2010

Weapons bay acoustic suppression using a novel rod in crossflow configuration

Shane Lackey

WEAPONS BAY ACOUSTIC SUPPRESSION USING A NOVEL ROD IN CROSSFLOW CONFIGURATION

by

SHANE LACKEY

A THESIS

Submitted in partial fulfillment of the requirements
for the degree of Master of Science in Engineering
in
The Department of Mechanical and Aerospace Engineering
to
The School of Graduate Studies
of
The University of Alabama in Huntsville

HUNTSVILLE, ALABAMA
2010

In presenting this thesis in partial fulfillment of the requirements for a master's degree from The University of Alabama in Huntsville, I agree that the Library of this University shall make it freely available for inspection. I further agree that permission for extensive copying for scholarly purposes may be granted by my advisor or, in his/her absence, by the Chair of the Department or the Dean of the School of Graduate Studies. It is also understood that due recognition shall be given to me and to The University of Alabama in Huntsville in any scholarly use which may be made of any material in this thesis.

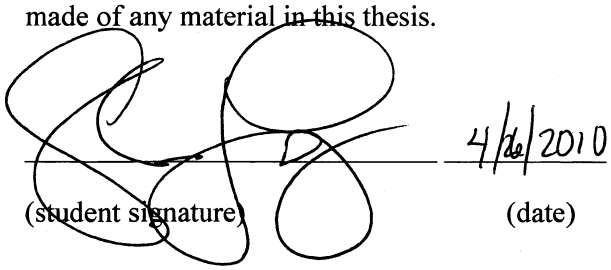

4/26/2010

(student signature) (date)

THESIS APPROVAL FORM

Submitted by Shane Lackey in partial fulfillment of the requirements for the degree of Master of Science in Engineering and accepted on behalf of the Faculty of the School of Graduate Studies by the thesis committee.

We, the undersigned members of the Graduate Faculty of The University of Alabama in Huntsville, certify that we have advised and/or supervised the candidate on the work described in this thesis. We further certify that we have reviewed the thesis manuscript and approve it in partial fulfillment of the requirements for the degree of Master of Science in Engineering.

4/26/10 D. Brian Landrum, Committee Chair

(Date)

4/27/10 Hugh W. Coleman

4/29/10 Kader Frendi

4/27/10 Kader Frendi, MAE Department Chair

Phillip Farrington, Dean of Engineering

Debra M. Moriarity, Dean of Graduate Studies

ABSTRACT

The School of Graduate Studies

The University of Alabama in Huntsville

Degree Master of Science in Engineering

College/Dept. Engineering/Mechanical and Aerospace

Name of Candidate Shane Lackey

Title Weapons Bay Acoustic Suppression Using a Novel Rod in Crossflow Configuration

A computational fluid dynamic study was performed to analyze the efficacy of a novel acoustic suppression device for high Mach number cavity flow. A clean cavity computational model was first qualitatively validated based upon recorded data and was shown to agree well with experimental results for overall sound pressure levels. The proposed configuration, consisting of a rod in crossflow over the leading edge of the cavity with a forty-five degree rod fence placed upstream of the cavity, was then inserted into the computational model to test for a quantitative reduction in sound pressure level. A reduction of approximately 8 decibels was observed with the proposed configuration. A parametric study of each component of the configuration was also evaluated in an attempt to isolate the reduction mechanism.

Abstract Approval: Committee Chair 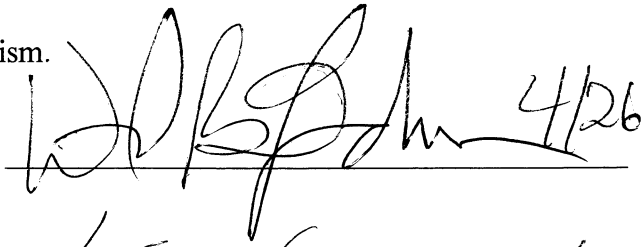 4/26/10

Department Chair 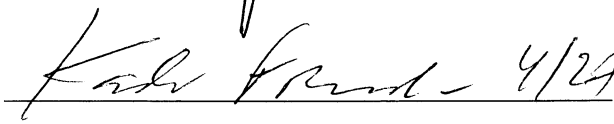 4/27/10

Graduate Dean  7/30/10

ACKNOWLEDGMENTS

The work described in this thesis would not have been possible without the assistance of Dr. Brian Landrum and the other members of my committee, Dr. Kader Frendi and Dr. Hugh Coleman.

The research for this thesis was supported in part by a grant of computer time from the DOD High Performance Computing Modernization Program at USASMDC Simulation Center.

I owe my deepest gratitude to Dr. Robert Tramel for taking me under his wing and mentoring me through the world of computational fluid dynamics and cavity flow acoustics. I would also like to thank Mr. Keith Jordan and Mr. Shawn Westmoreland for taking time to address my questions even when they had far too many things to do themselves.

Finally, I would like to thank my family for supporting me throughout my educational career, and Kaden and Millie for providing me with the motivation to see this degree through. I love you.

TABLE OF CONTENTS

LIST OF FIGURES

Figure **Page**

LIST OF TABLES

Table **Page**

LIST OF SYMBOLS

$OASPL$ – Overall Sound Pressure Level

d – Rod Diameter

D – Cavity Depth

f_m – Frequency of Rossiter Mode m

γ – Ratio of Specific Heats

K_v – Vortex Convection Ratio

L – Cavity Length

L/D – Cavity Length to Depth Ratio

L_{ref} – Reference Length of Computational Grid

m – Mode number

M – Mach Number

n – Phase shift

P_{ref} – Reference Pressure

P_{std} – Standard Deviation of Pressure

q – Dynamic Pressure

S_i – Strouhal Number

t – Time

τ – Time Step

V_{inf} – Freestream Velocity

V_v – Vortex Velocity

Chapter 1

INTRODUCTION

For many years, tactical aircraft used wing pylons and other external storage methods to mount and deliver munitions to the battlefield. However, with the ever increasing need to improve aircraft performance by reducing parasitic drag, as well as the need to minimize the radar signature of contemporary aircraft, designs are moving to internal storage of munitions in weapons bays. While storing the munitions internally generally increases aircraft survivability and performance, it does not come without pitfalls. Once the weapons bay is exposed to the external flow, extremely high overall sound pressure levels (OASPL) can be seen within the cavity. These high sound pressure levels can be detrimental to the electronics and guidance systems of the stored smart munitions and can also excite mechanical and structural modes of the aircraft, potentially leading to catastrophic failure. To make matters worse, for a fixed dynamic pressure, or q, the amplitude of the acoustic radiation increases with Mach number up to approximately Mach 1.2; making weapon release an even greater problem at higher speeds. In order to combat this problem, research is underway to develop methods to reduce the OASPL to a reasonable operational level within weapons bays at subsonic and supersonic speeds.

In recent years there has been a great deal of focus applied to three methods of controlling cavity acoustic oscillations: diversion or lofting of the shear layer, high-frequency shear layer forcing, and low-frequency shear layer forcing [1], [2], [3]. Based upon these control methods, various control systems have been proposed. But regardless

of the control method chosen, the general routine for testing these systems has been to fabricate a model and test the efficacy of the configuration using a combination of wind tunnel and flight tests. While experimental verification is a very important aspect of the qualification of any acoustic suppression device, it is also very expensive. Therefore, it would be beneficial to build a reliable computational model in which several different configurations could be tested before committing to the construction of a wind tunnel model and procuring a test facility.

The Reynolds Averaged based turbulence models and lower order numerics used in many computational fluid dynamic codes are overly dissipative when applied to unsteady flowfields which makes them unsuitable for the routine prediction of aero-acoustics. However, the recent addition of higher order numerical schemes and advanced turbulence modeling techniques has greatly expanded the ability of codes such as NASA's OVERFLOW2 code to accurately predict the coarse grained details of turbulent flows [4], [5], [6], [7], [8].

While many devices have shown excellent acoustic suppression at low speeds, few have reliably shown similar results at supersonic speeds. The proposed novel device consists of a bank of small rods at a forty-five degree crossflow angle, with a trailing larger rod. This configuration provides a two pronged attack by first lifting or diverting the shear layer and then by inducing high frequency shedding, or high frequency shear layer forcing, in its wake. This configuration was believed to be optimal based upon its passive nature and its simplistic design that may have the ability to be retracted into the aircraft when not in use.

The main objective of this thesis was to investigate the acoustic suppression ability of this novel rod in crossflow configuration in high Mach number flow using the OVERFLOW2 code. Five different configurations were studied. A clean cavity was first analyzed and compared to experimental data for qualitative validation. Next, the proposed configuration was analyzed, followed by a parametric study of each individual component (the forty-five degree fence and the large rod) to evaluate their efficacy as standalone devices. Finally, a modified version of the initial proposed configuration was also evaluated. Each of these configurations is examined in detail in later chapters.

Chapter 2

CAVITY FIELDS AND ACOUSTIC SUPPRESSION

2.1 Cavity Flow Overview

The phenomena of acoustic radiation due to pressure oscillations within cavities is prevalent in our everyday lives. Self-Sustained oscillations occur in such things as musical instruments, flow past an open window or sunroof of a car, and in the wells of landing gear and internal weapons bays. In musical instruments (flutes, organs, etc.) the acoustic radiation is advantageous, but in most engineering applications it is undesirable. In certain instances the intensity of the pressure oscillations associated with the acoustic radiation can be detrimental to performance or safety. The frequency and associated amplitude of these pressure oscillations can be potentially strong enough to excite mechanical modes and/or cause fatigue or material failure.

The phenomena of cavity flow acoustic radiation was investigated as far back as the late 1800's with experiments conducted by Strouhal, Rayleigh, and Kohlrausch. In his book, *The Theory of Sound*, Rayleigh postulated that the mechanism behind the acoustic radiation of flow over a cavity was undoubtedly, "connected with the instability of vortex sheets" [9]. He also showed that any disturbance caused the motion of the vortex sheet, "to increase rapidly." This is an important finding since the pressure oscillations in a cavity are generally attributed to vortex formation from shear layer instability. In 1937, Brown began studying self-sustained cavity oscillations by focusing on edge tones [10]. In his study of an orifice jet impinging on a sharp edge, Brown

discovered that edge tones were produced when small disturbances in the flow are scattered into acoustic waves by the sharp edge. These acoustic waves then excite more disturbances in the flow creating a self-sustained feedback loop [10]. In the 1950's Roshko and Krishnamurty began studying flow over surface cutouts. Roshko noted that in flow over a surface cutout or cavity, the separated boundary layer deflects into the recess and impinges on the trailing edge [11]. Furthermore, in his thesis, Krishnamurty concluded that the frequency of acoustic radiation from the cutout was directly proportional to the airspeed and inversely proportional to the depth. He also hypothesized that there was a connection between the acoustic radiation from the cutout and the edge tone phenomena studied by Brown [12].

In 1962, Plumblee et al. developed a theory for the prediction of resonant frequencies and pressure amplifications within cavities [13]. Building on this work while performing research for the Ministry of Aviation in 1964, J. E. Rossiter developed the first semi-empirical formula for predicting the frequencies of oscillations and for describing the phenomena of acoustic resonance governing cavity oscillations [14]. The resultant formula, known as the Rossiter Equation, has since been widely accepted as the basic equation used for predicting cavity modes. Rossiter's work is further detailed in the following section.

2.2 Physics of Cavity Flow

The physics pertaining to the flow over an open cavity can be quite complicated. Expanding on the work of Roshko, Plumblee, and Brown [11], [13], [10], Rossiter began experimenting with flow over open cavities. From his experiments, he was able to quantify several influential parameters which aide in the prediction of acoustic radiation.

He noted that the mean flow over a cavity depends greatly on the length to depth ratio (*L/D*) of the cavity itself. Also, depending on the speed of the incoming flow coupled with this ratio, the flow may or may not expand and attach to the cavity floor. Therefore *L/D* and Mach number were determined to be very influential parameters in the prediction of cavity flow pressure oscillations [14]. These observations also reinforced Krishnamurty's conclusions from his experiments that the frequency of acoustic radiation from cavities was directly proportional to the airspeed and inversely proportional to the depth of the cavity [12].

Through shadowgraphs and measurements, Rossiter concluded that vortices were shed from the leading edge and as the flow continued downstream, the flow impinged upon the rear wall of the cavity causing an acoustic radiation at a regular interval [14]. Heller and Bliss [15] did not observe the same vortex shedding in their experiments and postulated that the acoustic radiation could be attributed to the motion of waves between a shear layer and a boundary. They did however agree that the source of the acoustic radiation was shear layer interaction with the rear lip of the cavity. The resultant pressure wave then propagated back upstream in the lower region of the cavity and caused the shedding of yet another vortex from the oncoming flow. At this point the cavity was "locked" into an acoustic phase between the incoming flow and the acoustic radiation from the rear wall of the cavity, a schematic of which can be seen in Figure 2.1.

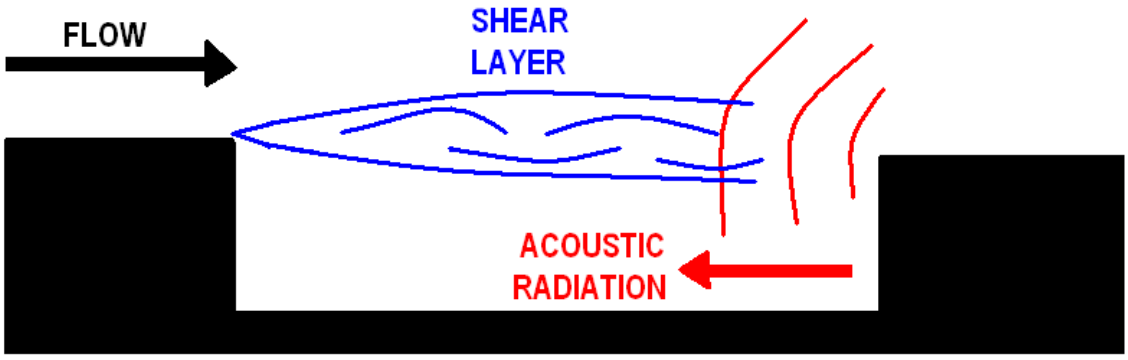

Figure 2.1 – Schematic of Cavity Flow Physics for a "Locked" Condition

Based upon his observations, Rossiter was able to determine that there was a correlation between the shedding of the upstream vortex and the acoustic radiation from the downstream trailing edge and developed what is known as Rossiter's equation [14]

$$f_m = \frac{V_\infty}{L}\frac{(m-n)}{(1/K_V + M)}, \tag{2.1}$$

where f_m is the frequency of acoustic mode m, V_∞ is the freestream velocity, K_V is the ratio of vortex velocity to freestream velocity, and n is the delay factor (or phase constant) between acoustic radiation at the trailing edge and vortex formation at the leading edge. For a cavity L/D equal to 4, Rossiter determined the values of n and K_V to be 0.25 and 0.57, respectively [14]. Heller et al. [15] and Smith and Shaw [16] later concurred with these values.

While Rossiter's equation proved to agree well with experimental data in the mid-subsonic range, in 1971 Heller, Holmes and Covert [17] improved upon Rossiter's equation by using the freestream total temperature as an estimate of the cavity speed of sound. This allowed for calculations at variable specific heat ratios as well as at higher Mach numbers. Furthermore, Dix and Bauer in 1994 used a curve fit to experimental

data to produce an empirical formula for calculating the phase constant, *n*, based upon the length to depth ratio of the cavity [1],

$$n = 0.062\left(\frac{L}{D}\right). \tag{2.2}$$

Based upon the modifications by Heller et al. and Dix and Bauer, a new equation, the Modified Rossiter Equation, was developed,

$$f_m = S_i \frac{V_\infty}{L} = \frac{V_\infty}{L} \frac{(m-n)}{\left[\dfrac{M}{\left(1+\dfrac{(\gamma-1)}{2}M^2\right)^{\frac{1}{2}}} + \dfrac{1}{K_v}\right]}, \tag{2.3}$$

where S_i is the non-dimensional frequency, or Strouhal number, and all other variables are the same as in the original Rossiter Equation. Equation 2.3 is widely accepted as the basis for prediction of cavity acoustic frequencies and was used as the basis for modal predictions in this thesis due to its good agreement with supersonic test data [18].

2.3 Acoustic Suppression Techniques

In recent years, there has been an ongoing research to mitigate the acoustic radiation from internal bays and cavities on commercial and tactical aircraft. For high-speed tactical aircraft, there are several inherent problems, including but not limited to space constraints and the ability to operate over a wide range of Mach numbers. As previously stated, the interaction of the shear layer with the rear cavity wall is the dominant source for the acoustic radiation. The shear layer, which develops at the leading edge of the cavity where the high-speed flow mixes with the low speed flow inside the cavity, becomes unstable and rolls up into large coherent vortices over the span of the cavity. The vortices then impinge upon the back wall of the cavity causing acoustic

radiation which propagates back upstream and causes yet another vortex to be shed, thus creating the aforementioned self-sustained feedback loop. Therefore, in order to accomplish the arduous task of acoustic suppression, especially at supersonic Mach numbers, two primary tactics have most prevalently been employed: *vertical shear layer displacement, and shear layer control and manipulation.*

Shear layer displacement is the most simplistic of the suppression approaches. As discussed earlier, the acoustic radiation occurs when the flow within the cavity gets locked into a self-sustained acoustic feedback loop (see Figure 2.1). This happens when the unstable shear layer from the front cavity lip impinges upon the rear cavity wall and emits pressure waves that propagate back upstream. These pressure waves then amplify flow instabilities in the shear layer and induce further vortex shedding. The idea behind vertical displacement is to divert the shear layer above the cavity thereby reducing the frequency at which it impinges upon the rear wall of the cavity, thus interrupting the phase in which the cavity has become locked.

Shear layer control and manipulation is a much more complicated technique, but the basic premise is the same: to break up the locked phase of the cavity in order to reduce the sound radiation. By perturbing the flow at certain frequencies and disrupting the phase of the cavity, one can partially mitigate the formation of the large vortical structures and therefore reduce the energy at which the shear layer impinges upon the rear cavity wall, reducing the amplitude of the radiation.

The method of shear layer control can be further broken down into high and low frequency forcing techniques. In both categories, the approach is still to break up the locked phase of the cavity. In low frequency shear layer forcing, the shear layer is

perturbed at a frequency near the dominant tones in the resonant cavity [2]. The technique of low frequency forcing has shown limited results especially in the realm of supersonic flow. Conversely, high frequency shear layer forcing has shown promising results. High frequency forcing is performed by perturbing the shear layer at frequencies much higher than the most unstable shear layer frequency as predicted by the Rossiter equation (Equation 2.3). By doing so, the large coherent vortical structures are broken down into much smaller structures, causing a diminished acoustic radiation at the rear cavity wall. This breaks up the feedback loop and reduces the overall sound pressure level of the cavity.

The shear layer displacement and shear layer control and manipulation methods can then be further decomposed into either passive or active devices. Heller and Bliss in 1975 [15], Sarohia and Massier in 1976 [19], as well as Gharib in 1987 [20] were some of the first to propose the idea of controlling cavity acoustic resonance. Heller and Bliss [15] proposed the use of a sloped rear wall to provide relief from the perpendicular impingement of the shear layer on the rear corner of the cavity thus reducing the amplitude of the acoustic radiation. Sarohia and Massier [19] conducted experiments using mass injection into the base of the cavity to stabilize the naturally oscillating shear layer, reducing its interaction with the aft wall of the cavity. They believed that the stability of the shear layer had been achieved, "by supplying the mass required for cavity shear layer entrainment externally." Gharib [20] used a sinusoidally heated strip upstream of the cavity to induce disturbances in the flow which were further amplified by the boundary layer and then introduced into the shear layer above the cavity. He determined that by forcing the shear layer at certain frequencies through these

disturbances, he could reduce the velocity fluctuations in the cavity by up to forty percent.

While these attempts provided insight into cavity acoustic suppression, in the 1990's and into the 21st Century, more and more research has been focused on trying to determine the best method, active or passive, of controlling cavity pressure oscillations. Due to the wide range of Mach numbers at which many military aircraft operate, an active control device must theoretically be able to adapt to the different flowfields. Devices such as oscillating fences [3] [21], oscillating flaps [22], and mass injection [18] [3] [23] have been tested. However, one pitfall of active flow control is that when control is used to reduce the amplitude at one frequency, typically, there is an increase in amplitude at another frequency [24]. Therefore passive flow treatments such as leading edge spoilers and high frequency tone generators have been investigated in recent years. While the benefits of a passive control device include the absence of a control system, many believe that the Mach range at which the device operates is limited. Regardless, these passive control techniques have shown good results, where the active control devices have proven less successful [18].

McGrath and Shaw [22] were the first to use a cylinder in crossflow as a suppression device. While no supersonic data was recorded due to time constraints, they were able to show significant reduction in sound pressure levels using the cylinder. Following the experiments of McGrath and Shaw, Stanek, et al. [25] were able to show marked reduction in sound pressure levels at both subsonic and supersonic speeds using a cylinder in crossflow. In subsonic flow, the cylinder in crossflow was able to achieve a 10 dB reduction in the Rossiter tones of a $L/D = 5$ cavity and a 16 dB reduction in

supersonic flow of the same cavity. Stanek also proposed a set of rules for mounting and designing the rod used for high frequency acoustic suppression. After comparing his rod in crossflow results to those obtained using mass injection, leading edge spoilers, and a rod mounted on top of a flat top spoiler, Stanek stated that his results, "provided the first irrefutable proof that high frequency acoustic suppression in high speed flows is real" [25]. This statement, along with computational research performed by Tramel et al. [26] is the basis for the approach discussed in this paper.

Chapter 3

COMPUTATIONAL MODEL DEVELOPMENT

3.1 WICS Experimental Model

In order to ensure the best analysis possible, it was necessary to qualitatively validate the computational model against a trustworthy dataset. For cavity flow, the experiments performed by Dix and Bauer at Arnold Engineering Development Center in Tullahoma, Tennessee, over the course of several years between 1986 and 1990 are widely regarded as a benchmark for the validation of cavity flow simulations [1]. The database constructed from the experiments, known as the Weapons Internal Carriage and Separation (WICS) database, contains a wide array of information pertaining to the acoustics of cavity flow as well as store separation. One of the experiments measured the fluctuating pressures, or acoustics, acting on a plate/cavity configuration.

Shown schematically in Figure 3.1, the model used in the Dix and Bauer experiments was a simple 18 inch long by 4 inch wide rectangular cavity constructed in a 47 inch long by 16.5 inch wide flat plate. The cavity was constructed so that the length to depth (*L/D*) ratio could be varied by installing the floor at several discrete locations between 0 and 4 inches. However, only three depths (1.25 in., 2 in., and 4 in.) were used in the experiments, corresponding to cavity *L/D* ratios of 14.4, 9.0, and 4.5, respectively [1]. In this thesis, comparisons were only made to the WICS cavity with a 4.5 length to depth ratio. This ratio was chosen due to it being sufficiently deep enough to provide similarity to the weapons bays of current generation tactical aircraft.

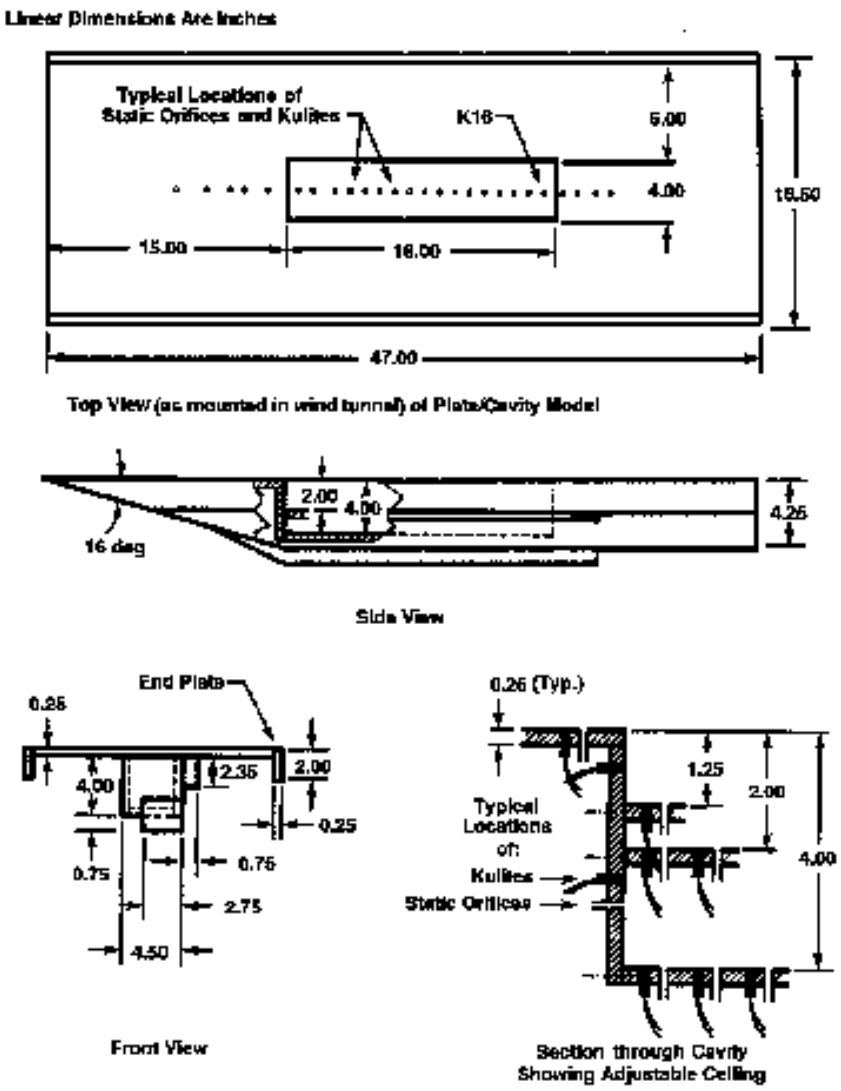

Figure 3.1 – WICS Experimental Model [1]

The experimental WICS model also used pressure transducers affixed to the floor of the cavity at discrete points for purposes of transient data recording. In order to qualify the computational model in this thesis, the sound pressure levels recorded by the transducers in the Dix and Bauer experiments were compared to the calculated sound pressure levels at comparable locations within the computational model. The locations of each of the transducers and computational grid locations are listed in Table 3.1 and shown in Figure 3.2.

Table 3.1 – Comparison of Pressure Sensor Locations of the WCIS Experimental Model and Data Recording Locations for the Computational Model

Sensor	WICS		Computational Model	
	X(in)	X/L	X(in)	X/L
K5	0.275	0.015	0.2636	0.015
K6	1.075	0.060	1.1	0.061
K7	1.975	0.110	2	0.111
K8	3.775	0.210	3.8	0.211
K9	4.675	0.260	4.7	0.261
K10	5.575	0.310	5.6	0.311
K11	8.275	0.460	8.3	0.461
K12	9.175	0.510	9.2	0.511
K13	10.075	0.560	10.1	0.561
K37	10.975	0.610	10.975	0.610
K38	11.875	0.660	11.875	0.660
K39	12.775	0.710	12.775	0.710
K40	13.675	0.760	13.675	0.760
K41	14.575	0.810	14.575	0.810
K42	15.475	0.860	15.475	0.860
K14	16.025	0.890	16	0.889
K15	16.925	0.940	16.9	0.939
K16	17.725	0.985	17.7275	0.985

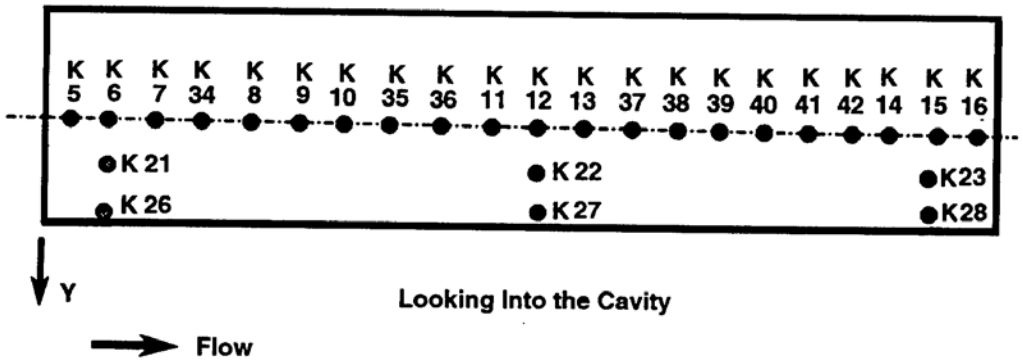

Figure 3.2 – WICS Pressure Sensor Locations [1]

3.2 Clean Computational Model

In order to obtain a robust computational model that can be accurately compared to the recorded WICS data, one must take care to ensure the model is as similar to the experiment as possible. Construction of the computational model was performed using several different software packages. A two-dimensional (18in L x 4in D), wind tunnel

scale model was constructed using ESI's CFD-GEOM, a commercially available structured and unstructured grid construction tool with limited CAD capabilities [27]. Using this geometry as a basis, six surface grids with a minimum five point overlap were also constructed using CFD-GEOM. Once the surface grids were completed, NASA's Chimera Grid Tools software package [28] was used to hyperbolically generate smooth grids using the HYPGEN function. In order to ensure an adequate number of grid points within the boundary layer, the initial off body grid spacing used for the computational model was chosen as 1×10^{-5} inches. This initial spacing, which translates into a y+ value of approximately 0.5, provided a dense enough mesh to enable the solver to compute the solution down to the viscous wall rather than depending upon wall functions for the calculation.

Once assembled, the six computational grids formed a two-dimensional representation of the WICS $L/D = 4.5$ model. From this two-dimensional center plane, NASA's GRIDGEN, also a part of Chimera Grid Tools [28], was used to construct a three-dimensional model by translating and concatenating 101 equally spaced, identical planes in the transverse direction a total of four inches, for a width to depth ratio of one. During preliminary analyses using simplified three-dimensional grid systems, this width was shown to provide adequate relief in the transverse direction, ensuring proper three-dimensional behavior of the flowfield. Viscous wall boundary conditions were applied to the flat plate upstream and downstream of the cavity as well as the cavity floor and fore and aft cavity walls. However, inviscid wall boundary conditions were applied to the side cavity walls in order to reduce computational time as well as in an attempt to ensure that the acoustic response of the cavity was a product of the length to depth ratio and not

a function of the width. A freestream inflow boundary condition of Mach 1.75 was applied approximately 3 cavity lengths in front of the leading cavity edge. A pure extrapolation outflow boundary condition was placed approximately 10 cavity lengths downstream of the rear cavity wall. A viscous wall boundary condition was also applied 15 inches upstream of the cavity leading edge in order to more accurately match the WICS experimental setup.

Each of the six computational grids were submitted into the Pegasus 5 pre-processor [29] which was used to cut holes, set up interpolations between grids, and combine the grids into one grid system for use in an overset flow solver. Once completed, the computational model of the clean cavity consisted of six computational grids with a total of approximately 7.7 million grid points. A preliminary refinement study was performed to show that these grid densities produced reliable results while simultaneously maintaining computational efficiency. The detailed grid numbers and dimensions are provided in Table 3.2 and the completed computational model is shown in Figures 3.3 and 3.4.

Table 3.2 – Dimensions of Computational Grids in Clean Cavity Study

Grid Dimensions				
Grid	**J**	**K**	**L**	**Total**
1	184	90	101	1,672,560
2	181	127	101	2,321,687
3	85	51	101	437,835
4	157	81	101	1,284,417
5	43	125	101	542,875
6	101	141	101	1,438,341
				7,697,715

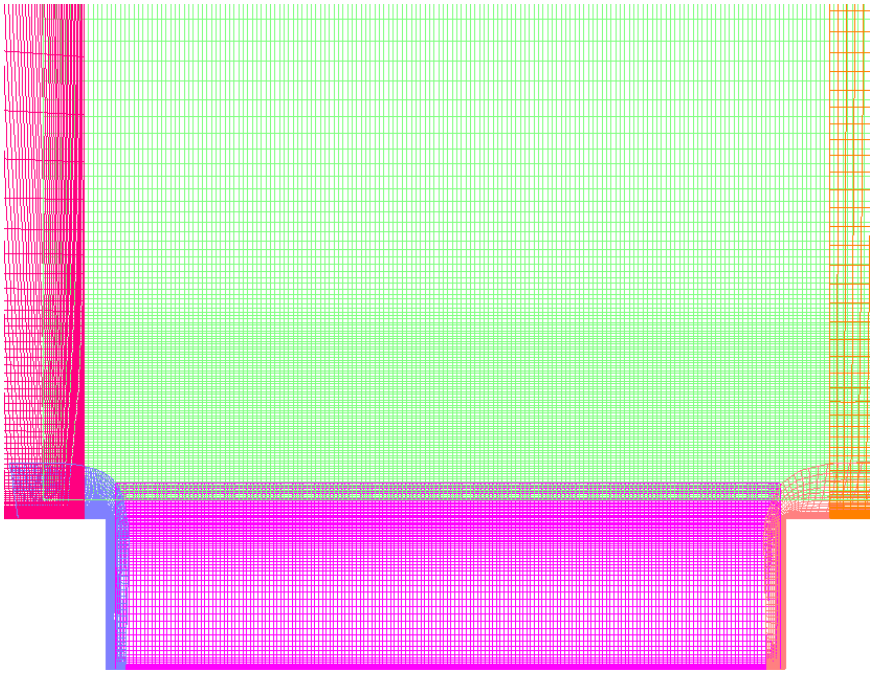

Figure 3.3 – Clean Computational Cavity, Side View

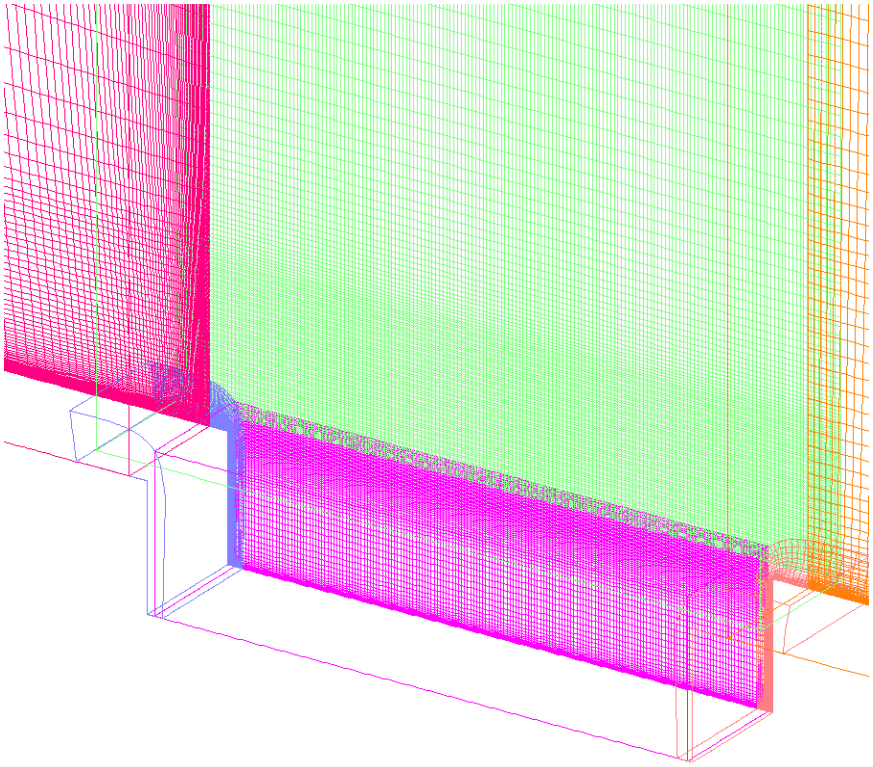

Figure 3.4 – Clean Computational Cavity, Isometric View

Once the computational model was constructed, NASA's OVERFLOW2 [30], an implicit overset Navier-Stokes flow solver, was chosen for the analysis. This particular flow solver was chosen due to the investigator's familiarity with the software, as well as OVERFLOW2's proven ability to accurately predict turbulent wake/shear layer flow. Much of OVERFLOW2's ability to accurately predict these phenomena can be attributed to the 5^{th} order WENO (Weighted Essentially Non-Oscillatory) schemes developed by Nichols, Tramel, and Buning [4], [5], [6], [7], [8]. The addition of these higher order numerical schemes and advanced turbulence modeling techniques has greatly expanded the ability of the code to accurately predict the coarse grained details of turbulent flows. By reducing the numerical dissipation/dispersion in the solver, the WENO schemes allow for much better prediction of vortex convection in the turbulent wake than other lower order schemes. These schemes, coupled with the shear-stress transport (SST) turbulence model, which has been shown to have good behavior in adverse pressure gradients and separating flow [4], and the detached eddy simulation (DES) approach, were used to compute the solution.

All flow inputs for the OVERFLOW2 simulations are provided in Appendix A. A Mach number of 1.75, a temperature of 344.8°R (191.4°K), a freestream velocity of 19106.7 in/s (485.31 m/s), and a Reynolds number of 191,667/in (7,546,945/m) were used. These conditions were used to match the dynamic pressure of 1200 lbf/ft² (57,456.4 Pa) and Mach number of 1.75 in AEDC's 4T tunnel used for the WICS experiments [1].

In order to determine the approximate number of time accurate steps needed to capture an adequate number of cavity oscillations, the "cycle time" of the cavity was calculated. This was done by first using the empirical phase constant calculation and the modified Rossiter equation, Equations 2.2 and 2.3, to calculate the analytical modal response of the cavity. Using these equations, the first six Rossiter modes of the computational cavity were calculated and are shown in Table 3.3. The calculated values were then used as a baseline estimate of the unstable shear layer frequencies of the given configuration as well as for calculating the necessary time step needed for the solver input.

Table 3.3 – Theoretical Prediction of Acoustic Cavity Modes for *L\D* = 4.5 WICS Experiment

Mode Frequency (Hz)		
1	**2**	**3**
244	583	922
4	**5**	**6**
1261	1600	1939

Previous experimental programs such as the WICS database have shown that most of the energy in cavity flow resonances is contained within the first three to four Rossiter modes [31]. Therefore, the 4th mode of approximately 1260 Hertz was used as the basis for the time stepping approximation.

NASA's OVERFLOW2 uses a non-dimensional time step, DTPHYS, for time accurate simulations. The value for DTPHYS was calculated by assuming the 4^{th} Rossiter mode as the highest frequency to be sampled. Therefore, the time for a vortex to transit the cavity was calculated by using the empirical relationship for convective vortex velocity derived by Rossiter [14],

$$K_V = \frac{V_V}{V_\infty}, \tag{3.1}$$

where V_V is the vortex velocity, V_∞ is the freestream velocity, and K_v is the empirically determined ratio of vortex velocity to freestream velocity, 0.57. Based upon this relationship, the vortex velocity was calculated to be 10890.95 in/sec (276.63 m/s). The cavity length was used to calculate an approximate time for each vortex to transit the length of the cavity by

$$\tau = \frac{L}{V_V} = \frac{18\ in}{10890.9508\ in/s} = 1.653 \times 10^{-3}\,\text{sec}. \tag{3.2}$$

Assuming the approximation that the vortex velocity is the same traveling both downstream, then back upstream, a "cycle" can be estimated as 2τ, or 0.0033 seconds. From this calculation for a cavity "cycle", the maximum value for DTPHYS was determined using,

$$DTPHYS = \frac{\Delta t V_\infty}{L_{ref}} = \frac{(0.0033s)(19106.7in/s)}{1in} \approx 63.052, \tag{3.3}$$

where Δt is the physical time, V_∞ is the freestream velocity, and L_{ref} is the reference length in grid units. This value for DTPHYS is the value that would bracket approximately one cycle of the 4th Rossiter tone as previously calculated. However, in order to ensure that the solution is highly sampled as well as to ensure solution stability, a more standard value of DTPHYS of 0.1 was chosen. The corresponding physical time step is thus calculated to be,

$$\Delta t = \frac{DTPHYS\, L_{ref}}{V_\infty} = \frac{(0.1)(1in)}{(19106.7\ in/s)} \approx 5.233\ x\ 10^{-6}\ \text{sec}. \tag{3.4}$$

With a "cycle" taking approximately 0.0033 seconds, this time step ensures that there is approximately one cycle every 660 steps.

Once the flow inputs were determined, the clean cavity case was initialized with a steady state startup of 5000 steps. This minimizes the initial startup transients and helps transition into the time accurate solution. After the initial steady state startup, the simulation was computed for 25,000 time accurate steps, or approximately 38 cycles, which was believed to be an adequate sampling for the spectral calculations.

3.3 Qualitative Comparison

During the course of the simulation, pressure data was taken at 18 microphone locations corresponding to the same locations of pressure sensors inside the experimental cavity. The most widely scrutinized microphone locations are shown in Figure 3.5.

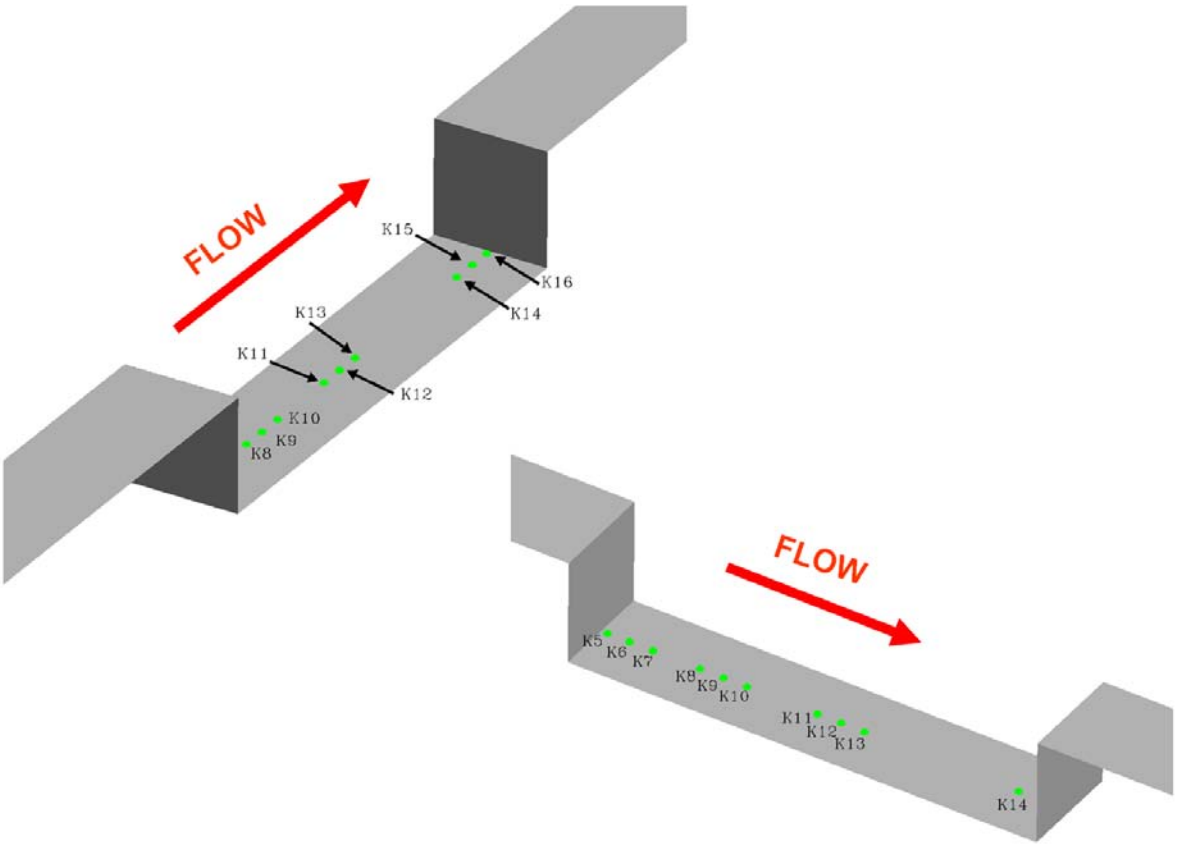

Figure 3.5 – Computational Model Microphone Locations

The overall sound pressure level at each microphone was computed by,

$$OASPL = 10 * \log_{10}\left(\frac{P_{std}}{P_{ref}}\right)^2 = 20 * \log_{10}\left(\frac{P_{std}}{P_{ref}}\right), \quad (3.5)$$

where P_{std} is the standard deviation of the pressures measured at each location and P_{ref} is the reference pressure, which is usually the threshold of human hearing, or 2.9×10^{-9} psi (2×10^{-5} Pa). The experimental and calculated sound pressure levels are compared in Table 3.4 and Figure 3.6. The calculated sound pressure levels were determined to be within approximately 5% of the experimental values at each of the 18 microphone locations. There was no record of uncertainty associated with the pressure sensors used by Dix and Bauer, so it was assumed that the 5% margin was adequate for this thesis. The largest discrepancy between the calculated values and the experimental values occurred at sensor K39. This inconsistency could be attributed to either recirculation of the flow from the rear wall, or simply a bad sensor. However, due to the accuracy of adjacent sensors K38 and K40, it is possible that the data recorded with sensor K39 was simply corrupted.

Table 3.4 – Comparison of Overall Sound Pressure Levels Between Computational and Experimental Models

Sensor	WICS		Clean		% Diff
	X/L	OASPL (dB)	X/L	SPL (dB)	
K5	0.015	158	0.015	155.6	1.50
K6	0.060	156	0.061	154.1	1.21
K7	0.110	151	0.111	152.8	-1.20
K8	0.210	154	0.211	153.2	0.54
K9	0.260	155	0.261	154.6	0.25
K10	0.310	156	0.311	154.7	0.81
K11	0.460	159	0.461	156.3	1.71
K12	0.510	160	0.511	159.1	0.59
K13	0.560	157	0.561	161.0	-2.56
K37	0.610	162	0.610	162.4	-0.23
K38	0.660	162	0.660	162.6	-0.39
K39	0.710	155	0.710	162.8	-5.04
K40	0.760	160	0.760	163.1	-1.94
K41	0.810	162	0.810	162.9	-0.53
K42	0.860	163	0.860	163.3	-0.18
K14	0.890	163	0.889	163.7	-0.46
K15	0.940	166	0.939	165.4	0.37
K16	0.985	169	0.985	168.7	0.19

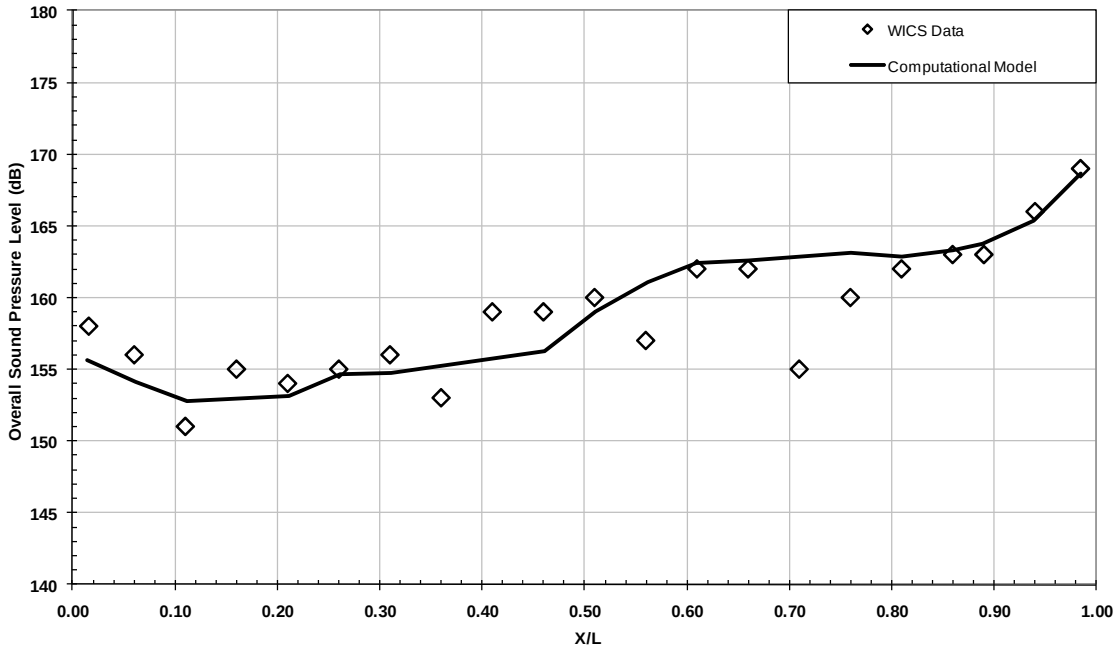

Figure 3.6 – Comparison of OVERFLOW2 Prediction to Clean WICS Cavity Data

Detailed predictions for sensors K5, K12, and K16 (located in the front, center, and aft wall portions of the cavity, respectively) are available for reference in Appendix B. Sensor K16, the sensor nearest the aft cavity wall, was chosen for

comparisons in this thesis due to its proximity to the acoustic source near the rear wall as well as its high amplitudes as noted by Dix and Bauer [1]. Additionally, the OASPL values predicted by the computational model were calculated to be within 0.2% of experiment at sensor K16 further reinforcing the decision to use this sensor as a basis for comparison for the analysis.

The calculated frequency content and amplitudes at sensor K16 are shown in Figure 3.7. The first six modal shapes can be seen at approximately 280 Hz, 630 Hz, 980 Hz, 1330 Hz, 1680 Hz, and 1960 Hz, with the third mode of approximately 980 Hz being the most dominant. Unfortunately, attempts to obtain WICS spectral data for this experimental setup were unsuccessful. Instead, comparisons were made to the theoretical frequency values. When compared to the first six theoretical values of cavity modes predicted by the Rossiter equation, the computational model does an excellent job of predicting the spectral content to within 15% at the first mode of 280 Hz and to within 1% at the sixth mode of 1960 Hertz. The time varying pressure at sensor K16 and the computed power spectral density are shown in Figures 3.8(a) and 3.8(b). Further evidence of the dominant tone is visible in Figure 3.8b where the highest energy peak is between 900 and 1000 Hertz.

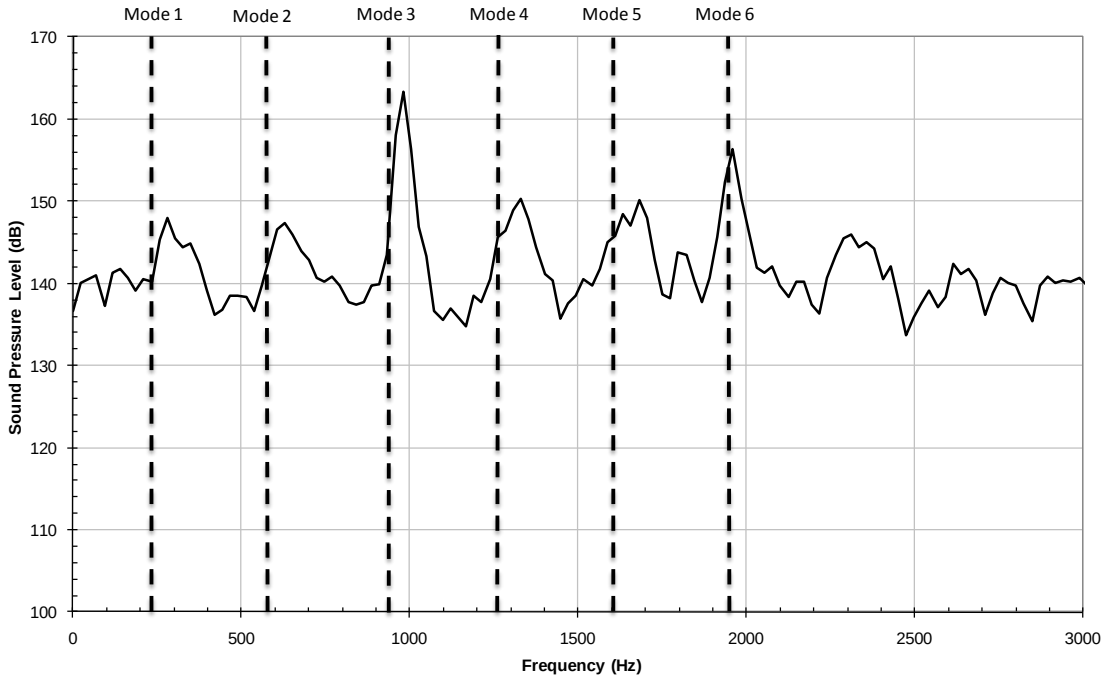

Figure 3.7 – Computed Sound Pressure Level vs. Frequency Plot for K16 Sensor in Cavity

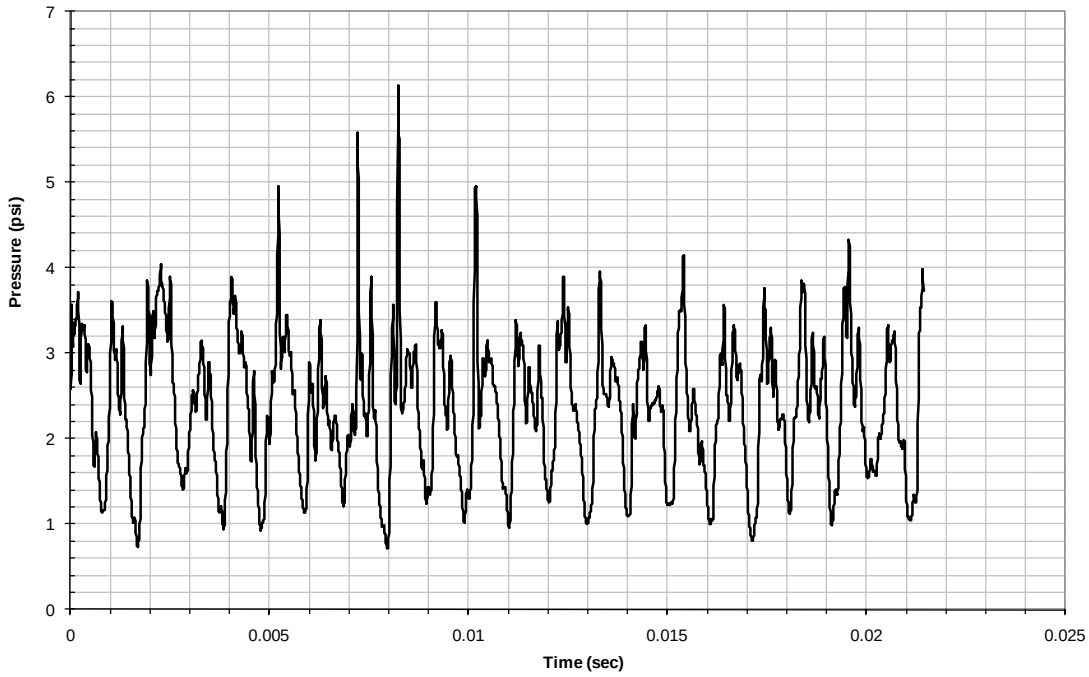

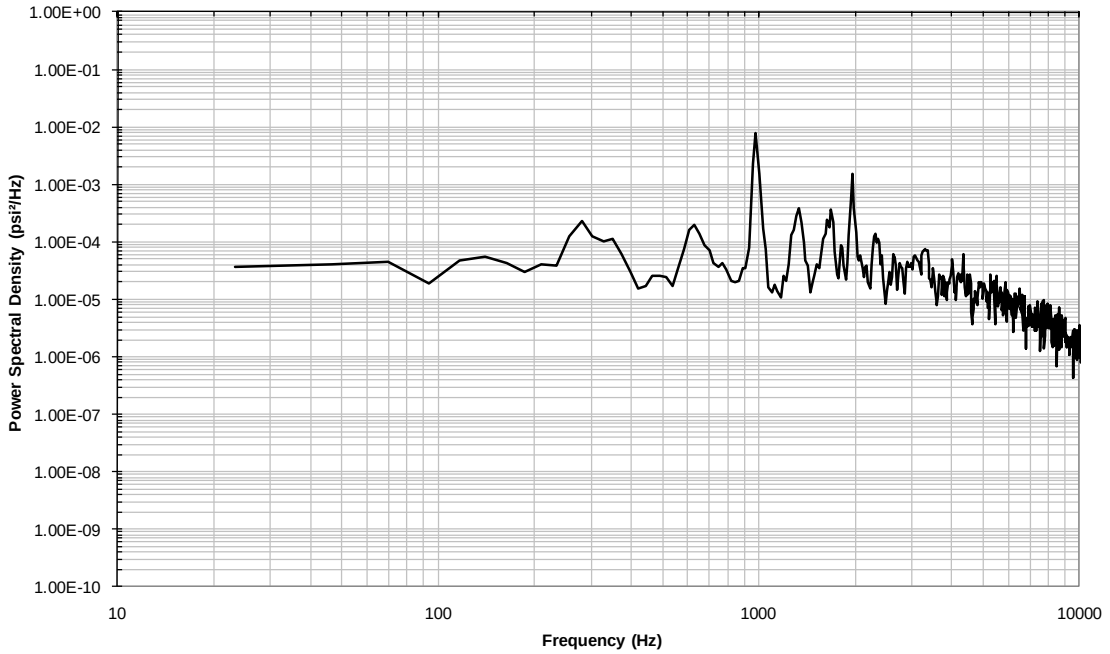

Figure 3.8 – (a) Computed Raw Pressure vs Time for K16 Sensor in Cavity
(b) Computed Power Spectral Density vs. Frequency Plot for K16 Sensor in Cavity

Flow visualizations were also developed in an attempt to understand the shear layer behavior for the clean cavity solution. Figure 3.9 shows an approximate cycle at quarter cycle increments of the dominant third Rossiter tone. It can be seen in the images that the vortex begins to roll up at the beginning of the cycle, impinges upon the rear wall at the quarter cycle emitting a pressure wave which radiates from the aft cavity wall. The pressure wave is reflected upstream (visible at the half cycle), and nears the leading edge of the cavity at the three-quarter cycle. Figure 3.10 shows the u-velocity contour of an approximate cycle of the dominant third Rossiter tone. The undulating shear layer is visible with apparent large vortical structures spanning the cavity and interacting with the aft cavity wall.

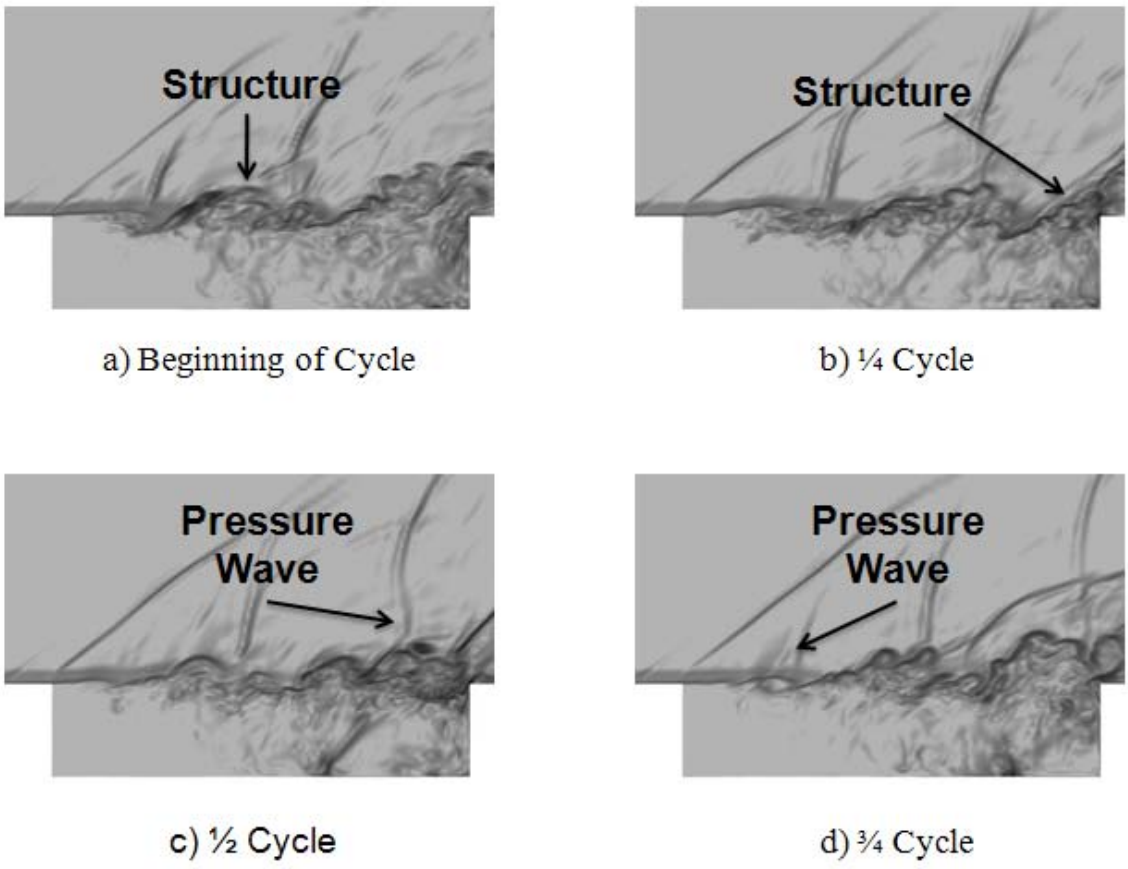

Figure 3.9 – Computed Pseudo-Schleiren Images of Dominant Third Rossiter Tone of Clean Cavity

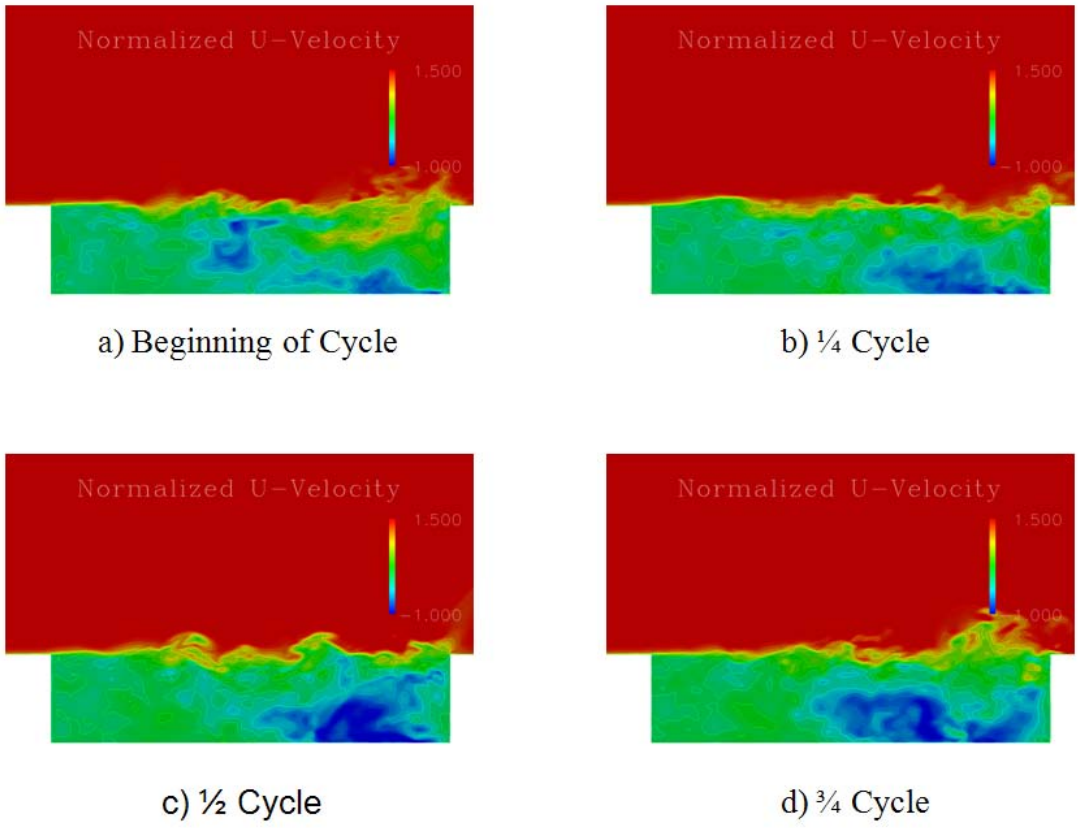

Figure 3.10 – Computed U-velocity Contours of Dominant Third Rossiter Tone of Clean Cavity

Based upon the results shown in this chapter, it was determined that the computational model could provide a qualitative comparison for the proposed configurations. The computational model was not only able to accurately predict the theoretical and experimental acoustic modes, but was also able to provide insight into which modes were contributing the most energy to the overall sound pressure level at the aft cavity wall.

Chapter 4

MULTIPLE ROD CONFIGURATION

4.1 Design Methodology

As previously mentioned, a novel approach to suppressing high speed cavity flow oscillations was proposed. The concept behind the configuration is to attack the problem using two proven approaches shown to have the propensity to work within a given aero-environment. In order to maximize acoustic suppression, and to potentially field a successful device, several factors were taken into consideration. In 1997, a survey by Dennis Bushnell [32] highlighted key parameters of successfully fielded flow control devices and the reasons why the devices were used. It was determined that in order to successfully field a device, it generally needed to be

1. Simple/inexpensive
2. Retrofittable
3. Passive/rigid
4. Reliable/"foolproof"
5. Able to be simulated in ground facilities at or near flight Reynolds numbers
6. Well understood/proven

Based upon Bushnell's findings, a simple, passive design was determined to be the best approach for success. By designing a simple, yet robust device, there would be less potential of accidental damage which could be detrimental to the efficacy of the device. By making a passive device, one could minimize the need for an expensive, complicated and potentially large control system.

As previously mentioned, there have been a large number of attempts at cavity flow control using passive or active systems, and also by using either shear layer forcing or diversion of the shear layer. Many of these systems are problematic due to their inability to operate over a wide range of Mach numbers. It was determined that for this investigation, a two pronged approach using both shear layer forcing as well as shear layer diversion would be used. This was accomplished by using two proven cavity flow treatments in tandem with one another: a forty-five degree rod fence for vertical displacement of the shear layer, followed by a larger rod which would then disrupt the formation of large coherent vortical structures by way of high-frequency shear layer forcing. The combined configuration is shown schematically in Figure 4.1.

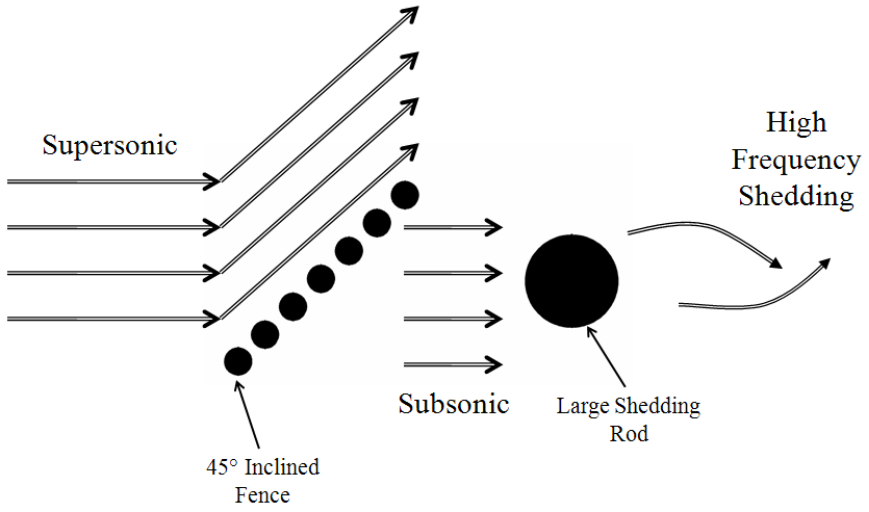

Figure 4.1 – Schematic of Proposed Combined Suppression Configuration

The combined system was designed with the notion that the rod fence would act as a spoiler to loft the supersonic flow while simultaneously decelerating the flow in its wake. At that point, the larger rod would induce high frequency vortex shedding,

breaking up the larger, more coherent vortical structures impinging on the rear cavity wall.

Earlier work by Stanek [25] led to a series of rules for using a rod in crossflow as an acoustic treatment for cavity flows. Stanek suggested that in order to get the best performance, the rod must be mounted directly over the leading edge of the cavity, have adequate height above the wall for shedding, and must be partially immersed in the boundary layer. He also developed a convenient equation for sizing and positioning of the rod based upon boundary layer height. However, due to the slotted rod fence upstream of the shedding rod, it was determined that prediction of the boundary layer height would be problematic, leaving rod sizing and positioning difficult to determine from Stanek's methodology. Further work by Illy, et al. [33] provided more suggestions for design and placement of a rod used as an acoustic suppression device for cavity flows. They agreed with Stanek in that the rod needed to be placed either directly above or at least in the vicinity of the leading edge of the cavity. However, rather than sizing and placing the rod based upon a sometimes unpredictable or changing boundary layer height, Illy believed the efficacy of the rod in crossflow as an acoustic suppressive device was based predominantly on a geometric parameter. As shown in Figure 4.2 this relative height parameter is based upon the ratio of the rod diameter, d, and the height of the rod above the cavity leading edge, z_d. Illy determined that the best results were obtained within the intervals of $0.5 < z_d/d < 0.7$ and $1.6 < z_d/d < 2.2$. Ironically, the supersonic suppression claimed by Stanek using a rod in crossflow fell within this same range of values, with a $z_d/d = 0.667$. Based upon such close agreement in independent

experimental studies, these parameters were used for the design of the proposed configuration.

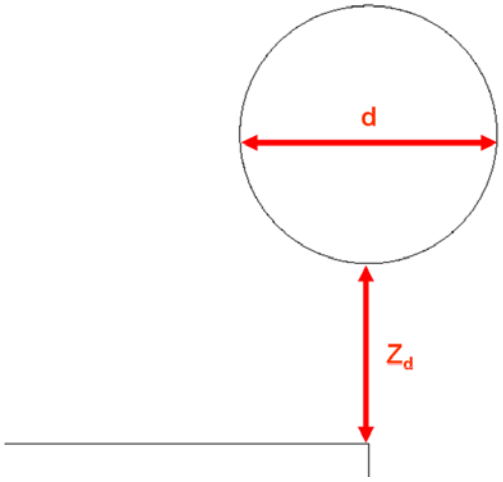

Figure 4.2 – Schematic of Illy, et al. [33] Geometric Sizing Dimensions

Since the size and number of rods comprising the fence could not accurately be assessed before the sizing of the large rod was complete, initial attention was placed upon the large rod and the fence was assumed to be absent. For high frequency shear layer forcing to be effective, the forcing, or shedding in this case, has to be significantly higher than the most unstable shear layer frequency of the cavity, estimated in the previous chapter to be the fourth Rossiter tone of approximately 1260 Hz. For this reason, a frequency of 12,000 Hz, a full order of magnitude higher, was chosen as the basis for the sizing of the large shedding rod. From his experiments, Stanek [25] calculated a modified Strouhal number of approximately 0.165. However, this calculation was based upon the rod being partially immersed in the shear layer. Due to the inability to predict the boundary layer behind the rod fence, White's [34] Strouhal number

$$S_i = \frac{fd}{V_\infty}, \tag{4.1}$$

where f is the desired frequency, V_∞ is the freestream velocity, and d is the rod diameter, was used for this thesis. Using White's Strouhal approximation of 0.2, a desired frequency of 12,000 Hz, and the freestream velocity, the diameter of the large cylinder was determined to be

$$d = \frac{S_i\, V_\infty}{f} = \frac{(0.2)(19{,}106.7\ ^{in}/_{sec})}{12{,}000\ Hz} \approx 0.3\ inches\,. \tag{4.2}$$

Once the size of the shedding rod was calculated, its placement was then determined. Based upon previously mentioned work by Stanek [25], Illy, et al. [33], and others, the best position is for the rod to be placed directly above or very near the leading edge. According to Stanek, the rod must have sufficient height to allow for shedding in its wake. Therefore, the upper limit of Illy's lower range was chosen in order to reduce the height above the leading edge while still providing enough clearance to ensure shedding. The relative height of the rod, z_d/d, was set to a preferred value of 0.7 as suggested by Illy, et al [33]. For a 0.3 inch rod diameter, this parameter yields a rod height of 0.21 inches. Once the size and position of the shedding rod was determined, a properly scaled and positioned model was added to the computational model of the clean cavity to assist in visually determining the size and number of small rods needed for the rod fence.

Attention was next directed to the smaller rods comprising the forty-five degree fence. The rods needed to be sufficiently high enough to shield the shedding rod from the incoming supersonic flow, while also providing enough volumetric flow rate to induce shedding on the aft rod. Therefore, given the large rod diameter of 0.3 inches, and

its height above the cavity leading edge of 0.21 inches, it was determined that the fence had to be a minimum of 0.51 inches high to ensure that the shedding rod was sufficiently protected from the incoming high speed flow. However, additional height was desired to ensure proper clearance. A total of seven rods with a nominal rod size of 0.09 inches were chosen based upon visualization of the system. The visualization was performed by systematically adding rods of different sizes and using engineering judgment. The rods were placed one rod diameter apart in the vertical and horizontal dimensions with the center of the bottom rod placed at one rod diameter above the cavity leading edge for a total height of 0.675 inches. This also assures that over one third of the fence (the first two rods) is immersed in the boundary layer based upon the calculated height of 0.24 inches from Dix and Bauer [1]. The horizontal placement of the rod fence was nominally chosen with the center of the most upstream rod at twelve small rod diameters (1.08 inches) upstream of the leading edge. This provided what appeared to be adequate spacing to allow any supersonic flow created by the rod fence to shock down to subsonic speeds before reaching the shedding rod at the cavity leading edge. The combined configuration is shown in Figure 5.3.

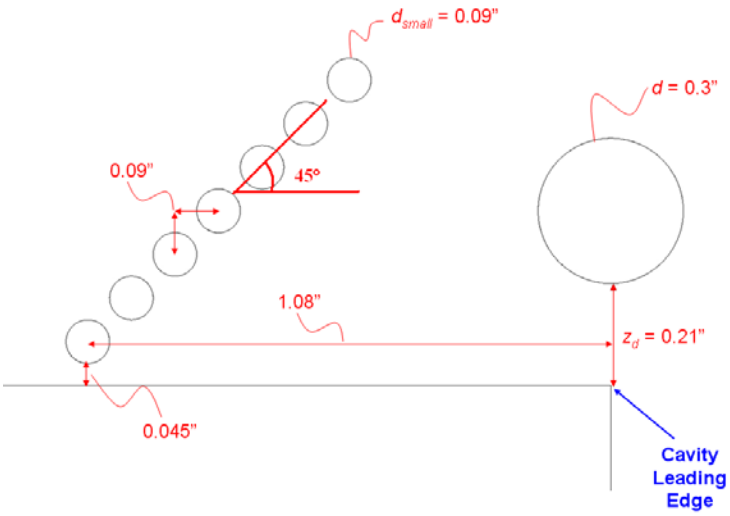

Figure 4.3 – Schematic of Proposed Configuration Composed of Angled Rod Fence and Large Shedding Rod

Once the geometric details of the configuration were determined, computational grids were built for the rods and appropriately placed within the clean cavity model. Each of the small rods was constructed with 181 points around the circumference and 52 points in the off body direction. The large rod was also constructed with 181 points around its circumference, but with 91 points in the off body direction. The same initial, off body spacing of 1×10^{-5} inches used in the construction of the clean cavity model grids was also used in the construction of the rod grids. Once the two-dimensional grids were constructed for each of the rods, OVERGRID [28] was again used to create, translate, and concatenate 101 equally spaced planes in the transverse direction. Due to the fact that OVERFLOW2 is an overset flow solver, the addition of the rods to the clean computational model was a trivial process. In order to accomplish this task, each grid was properly positioned and added to the clean computational model. Then the grid point interpolation and cutting of appropriate holes was determined by Pegasus 5 [29] and the

new computational model was obtained. The proposed forty-five degree fence with rod model is shown in Figure 4.4 below.

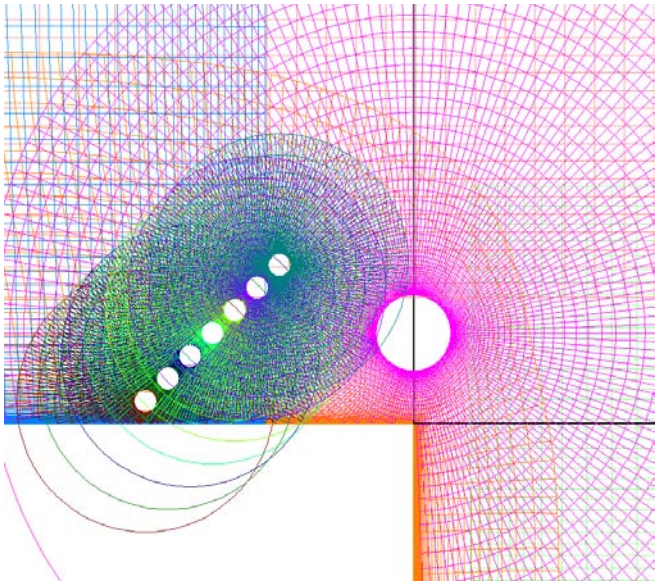

Figure 4.4 – Computational Model of Proposed Configuration

Viscous wall boundary conditions were applied to the new rod grids within the OVERFLOW2 input file, and an initial 5,000 step steady state solution was computed. This steady state startup was performed in order to facilitate stability. Once the initial steady state solution was complete, the simulation was carried out for an additional 25,000 time accurate steps. Time accurate data was recorded at each of the same microphone locations as the clean computational model for comparison purposes.

4.2 Acoustic Suppression Calculations

Overall sound pressure levels at each of the microphone locations were calculated for the multiple rod configuration and compared to the baseline clean configuration in Figure 4.5 and Table 4.1. Based upon the values at each point, an average reduction in the overall sound pressure level of approximately 7.6 decibels was calculated, which translates into a 59% reduction.

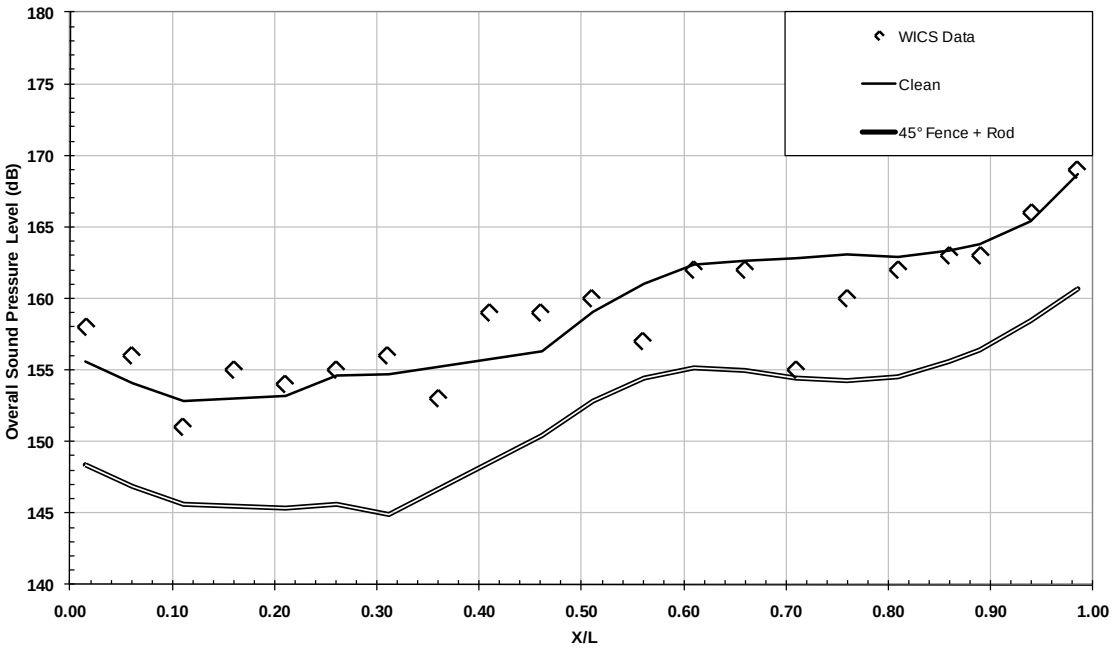

Figure 4.5 – OASPL Comparison of Clean Computational Model, Combined Configuration and WICS Experimental Model

Table 4.1 – Comparison of OASPL of Combined Configuration to Clean Computational Model

OASPL (dB)			
Sensor	**Clean**	**Fence +Rod**	**ΔdB**
K5	155.6	148.4	-7.2
K6	154.1	146.8	-7.3
K7	152.8	145.6	-7.2
K8	153.2	145.4	-7.8
K9	154.6	145.6	-9.0
K10	154.7	144.9	-9.9
K11	156.3	150.4	-5.9
K12	159.1	152.9	-6.2
K13	161.0	154.4	-6.6
K37	162.4	155.1	-7.3
K38	162.6	154.9	-7.7
K39	162.8	154.5	-8.3
K40	163.1	154.2	-8.9
K41	162.9	154.5	-8.3
K42	163.3	155.6	-7.7
K14	163.7	156.4	-7.4
K15	165.4	158.4	-6.9
K16	168.7	160.6	-8.1
Average			-7.6

The spectral results for the sensor with the highest OASPL (sensor K16 near the aft cavity wall) were also calculated and compared to the clean cavity results in Figure 4.5. There was a reduction in the peak 3rd Rossiter tone by approximately 8 dB at sensor K16 with the proposed configuration, as well as significant reductions in each of the other five previously noted Rossiter tones. Based upon a P_{ref} of 2 x 10^{-5} Pa (or 2.9 x 10^{-9} psi), the original sound pressure level of 168.7 dB equates to a sound pressure of approximately 5,445 Pa (or 0.73 psi). With the cavity treatment, the sound pressure level of 160.6 equates to a sound pressure of approximately 2,143 Pa (or 0.29 psi), a reduction of approximately 60 percent.

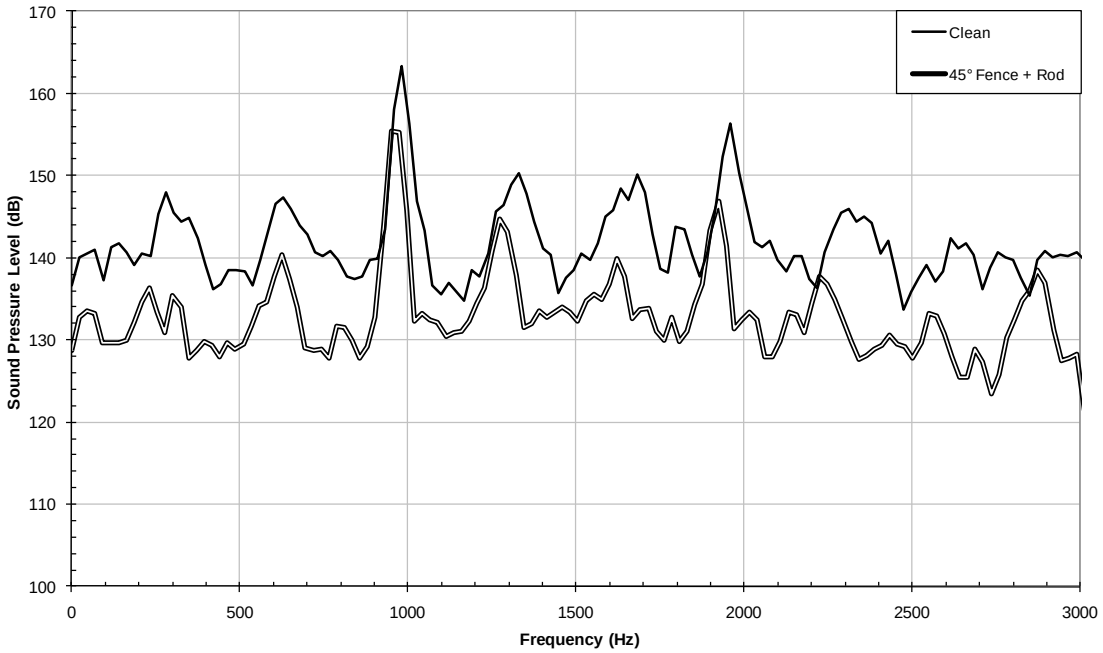

Figure 4.6 – Sound Pressure Level vs. Frequency Comparison of Clean Computational Model to Combined Configuration

Figures 4.7(a) and 4.7(b) are plots of the time varying pressure and computed power spectral density at sensor K16, respectively. The energy in each of the tones has

been significantly reduced by as much as approximately one order of magnitude for some modes.

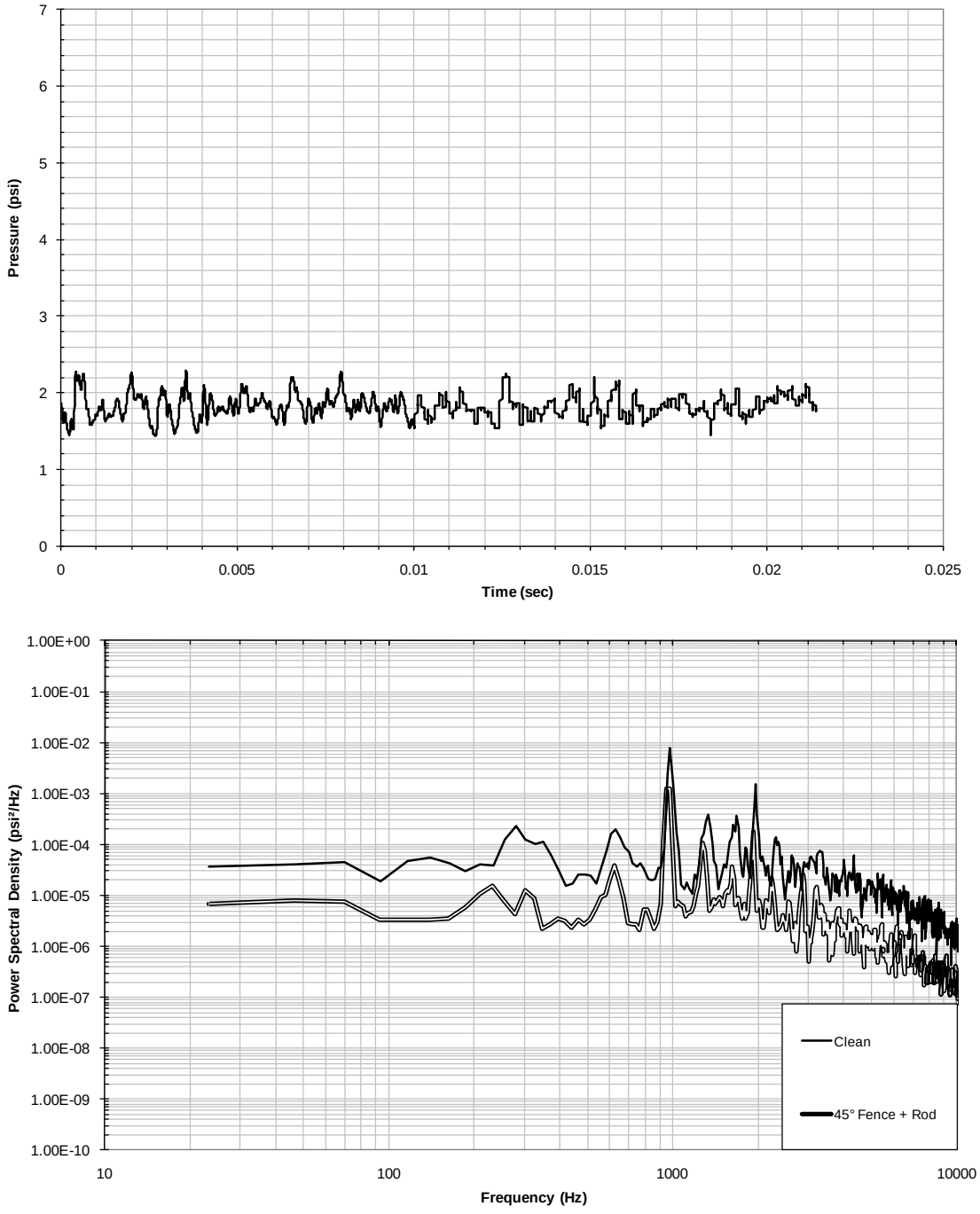

Figure 4.7 – (a) Computed Raw Pressure at Sensor K16 of Combined Configuration (b) Computed Power Spectral Density vs. Frequency Comparison of Clean Computational Model to Combined Configuration

Upon investigation of the flow visualizations, the proposed configuration appeared to be performing as hypothesized. In Figures 4.7 and 4.8 computed pseudo-Schleiren and u-velocity contours for an approximate cycle of the dominant third Rossiter tone are shown. Much like the clean computational cavity visualization, the cycle is broken into near quarter-cycle increments. In the pseudo-Schleiren image (Figure 4.7) a large bow shock is observed in front of the forty-five degree rod fence as well as a lambda shock, indicating separation upstream of the device. Figure 4.7 also shows that the large rod appears to be acting as hypothesized and is producing high-frequency vortex shedding. In the u-velocity contour plot (Figure 4.8) a recirculation at the aft cavity wall is indicated. This is believed to be due to the flow reversing after impinging upon the rear cavity wall. These results for the proposed configuration were encouraging, but a further investigation of the primary components was necessary to obtain a better understanding of the phenomena taking place.

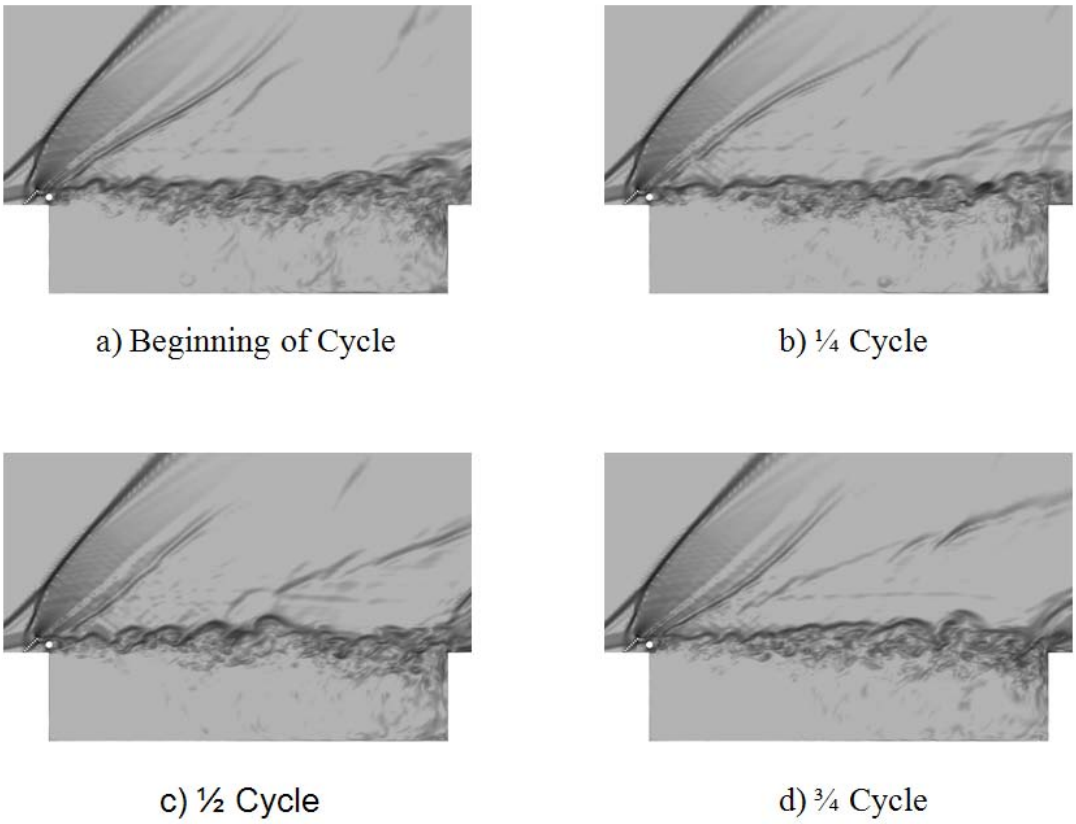

Figure 4.8 – Computed Pseudo-Schleiren Images of Dominant Third Rossiter Tone of Combined Configuration

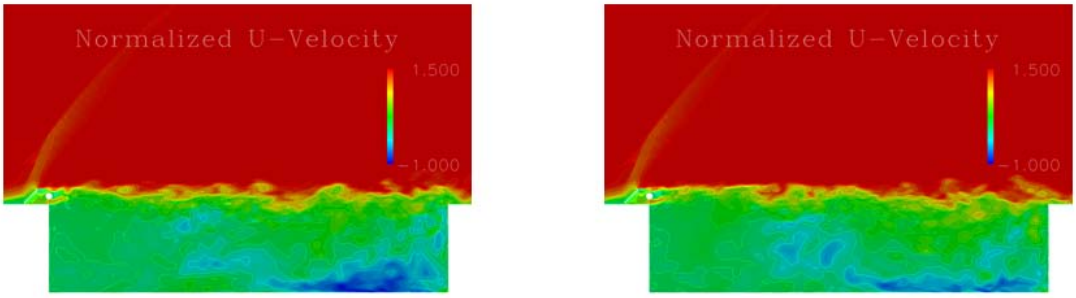

a) Beginning of Cycle

b) ¼ Cycle

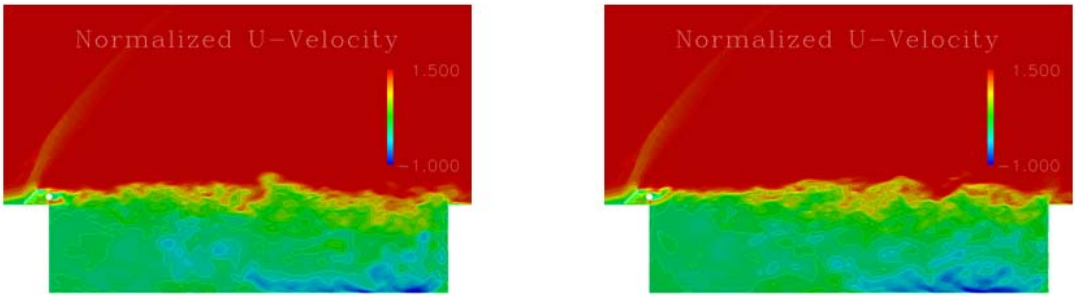

c) ½ Cycle

d) ¾ Cycle

Figure 4.9 – Computed U-velocity Contours of Dominant Third Rossiter Tone of Combined Configuration

Chapter 5

SINGLE ROD CONFIGURATION

5.1 Design

In order to assess the role of each component of the combined configuration in the reduction of sound pressure levels, it was proposed that the fence and shedding rod be examined on their own merits. The parametric study was performed in an attempt to isolate the driving mechanism in the acoustic suppression observed in the proposed configuration. This chapter focuses on the single, large, “shedding” rod.

Due to OVERFLOW2 being an overset flow solver, removing components of the chimera grid was a trivial task. The grids for each of the smaller rods comprising the fence were removed from the domain and the Pegasus 5 pre-processor was once again used to establish the new grid interpolations and to perform the necessary hole cutting for the computational domain. The new single rod grid system is shown in Figure 5.1. Once the new grid was obtained, a solution was computed using the same flow inputs as the previous two cases. Once again data was collected at each of the microphone locations from the baseline model.

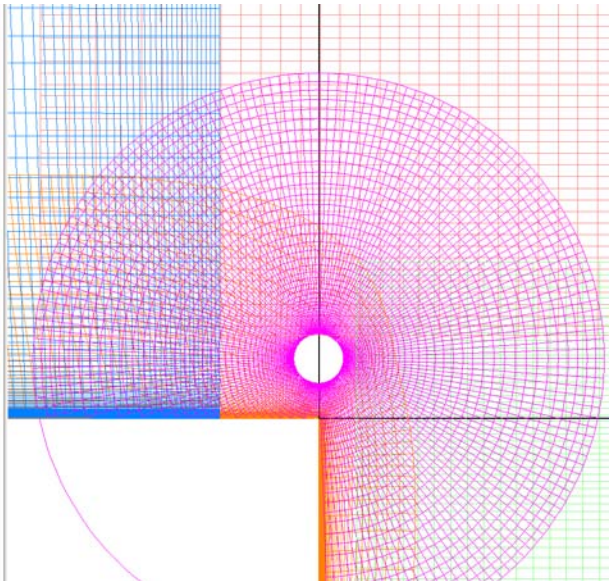

Figure 5.1 – Computational Model of Single Rod Configuration

5.2 Calculations and Comparison to Baseline

After completion of the simulation, the data was once again post processed using an FFT algorithm to compute the overall sound pressure level and the power spectral density at each of the microphone locations. The results of the comparison are shown in Table 5.1 and Figure 5.2. The average reduction in overall sound pressure level at each of the microphone locations was approximately 3.5 decibels which equated to less than half the 7.6 decibel average reduction observed with the combined configuration.

Table 5.1 – Comparison of OASPL of Single Rod Model to Clean Computational Model

OASPL (dB)			
Sensor	**Clean**	**Single Rod**	**ΔdB**
K5	155.6	152.4	-3.2
K6	154.1	150.9	-3.2
K7	152.8	149.4	-3.5
K8	153.2	149.6	-3.5
K9	154.6	150.8	-3.8
K10	154.7	151.0	-3.7
K11	156.3	153.3	-3.0
K12	159.1	155.7	-3.4
K13	161.0	157.6	-3.4
K37	162.4	158.8	-3.6
K38	162.6	159.3	-3.3
K39	162.8	159.2	-3.6
K40	163.1	158.9	-4.2
K41	162.9	158.5	-4.4
K42	163.3	159.6	-3.7
K14	163.7	160.4	-3.3
K15	165.4	162.5	-2.9
K16	168.7	165.6	-3.1
Average			-3.5

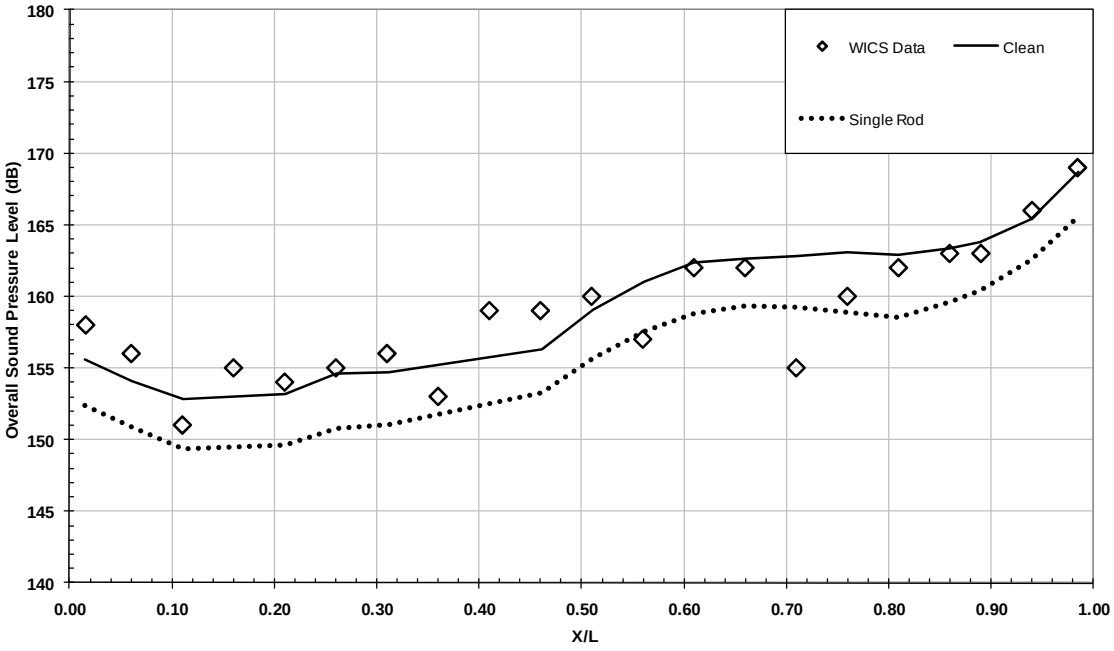

Figure 5.2 – OASPL Comparison of Clean Computational Model, Single Rod Configuration and WICS Experimental Model

Figure 5.3 shows that the single rod configuration all but eliminates the 1st Rossiter tone of approximately 240 Hz at the K16 sensor, but it also shows the appearance of increased amplitude in a low frequency mode at approximately 20 Hz that was not present in the clean cavity model. This could be an artifact of the windowing used in the post processing of the frequency data, but could potentially be the phenomenon of frequency shift referred to by Williams and Fabris [24].

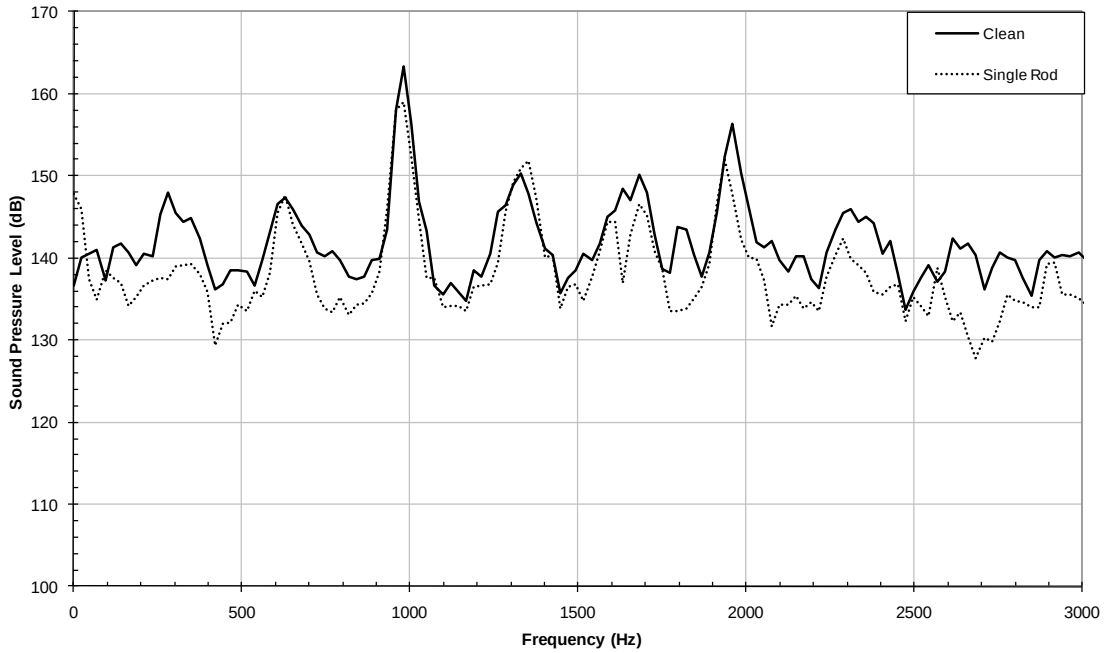

Figure 5.3 – Computed Sound Pressure Level vs. Frequency Comparison of Clean Computational Model to Single Rod Configuration

The time varying pressure as well as the computed power spectral density at sensor K16 are shown in Figure 5.4(a) and 5.4(b). The same 20 Hz tone observed in Figure 5.3 is also visible in the power spectral density plot at sensor K16 plotted in Figure 5.4(b). The energy in the 1st Rossiter tone is greatly reduced while the energy in the lower frequency mode is increased.

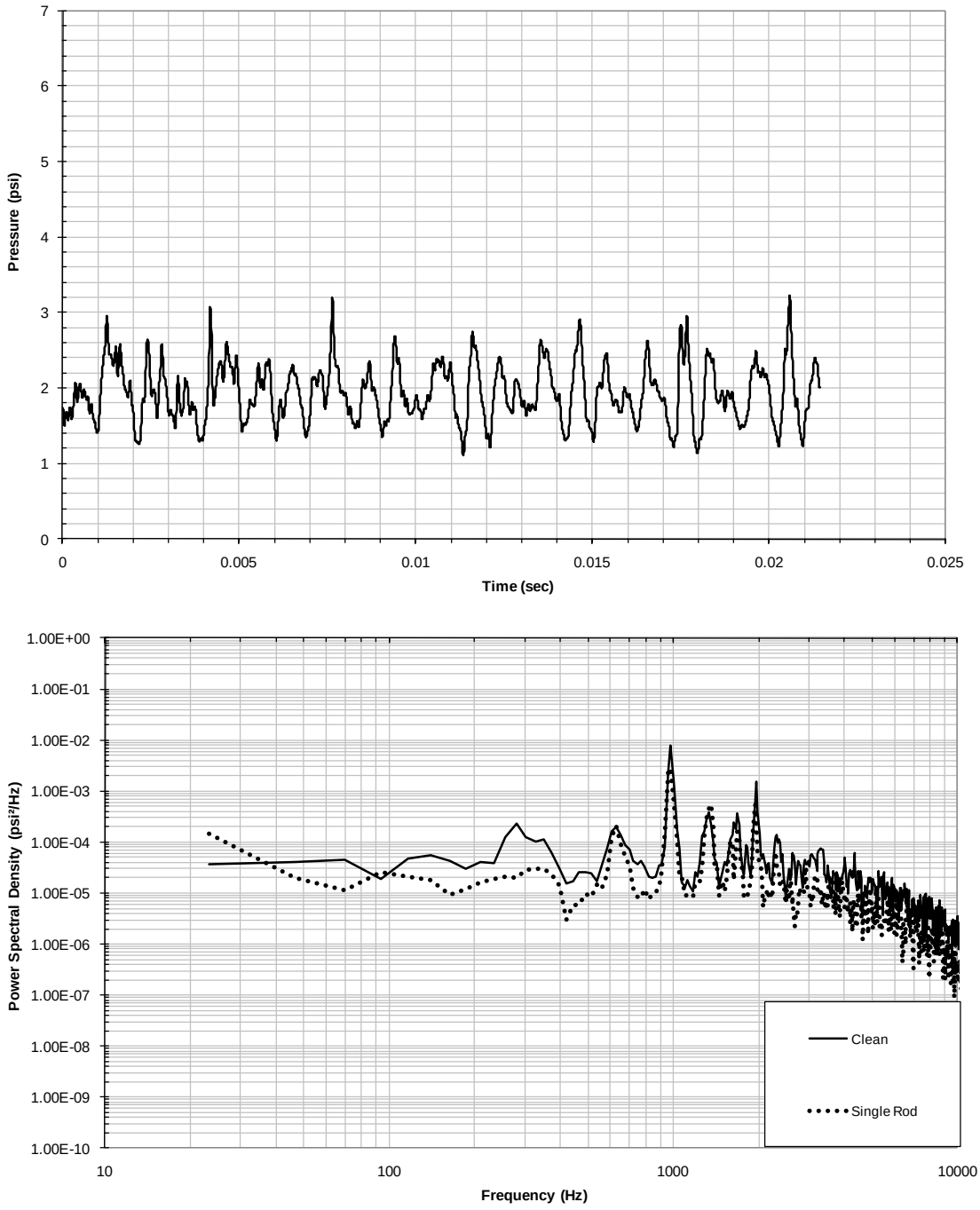

Figure 5.4 – (a) Computed Raw Pressure at Sensor K16 of Single Rod Configuration (b) Computed Power Spectral Density vs. Frequency Comparison of Clean Computational Model to Single Rod Configuration

The computational flow visualizations of the single rod case are shown in Figures 5.5 and 5.6. The pseudo-Schleiren images of Figure 5.5 appear to show shedding

from the single, large rod. However several large structures are also observed near the aft cavity wall at the quarter, half, and three-quarter cycle points. The same can be said for the u-velocity contours in Figure 5.6.

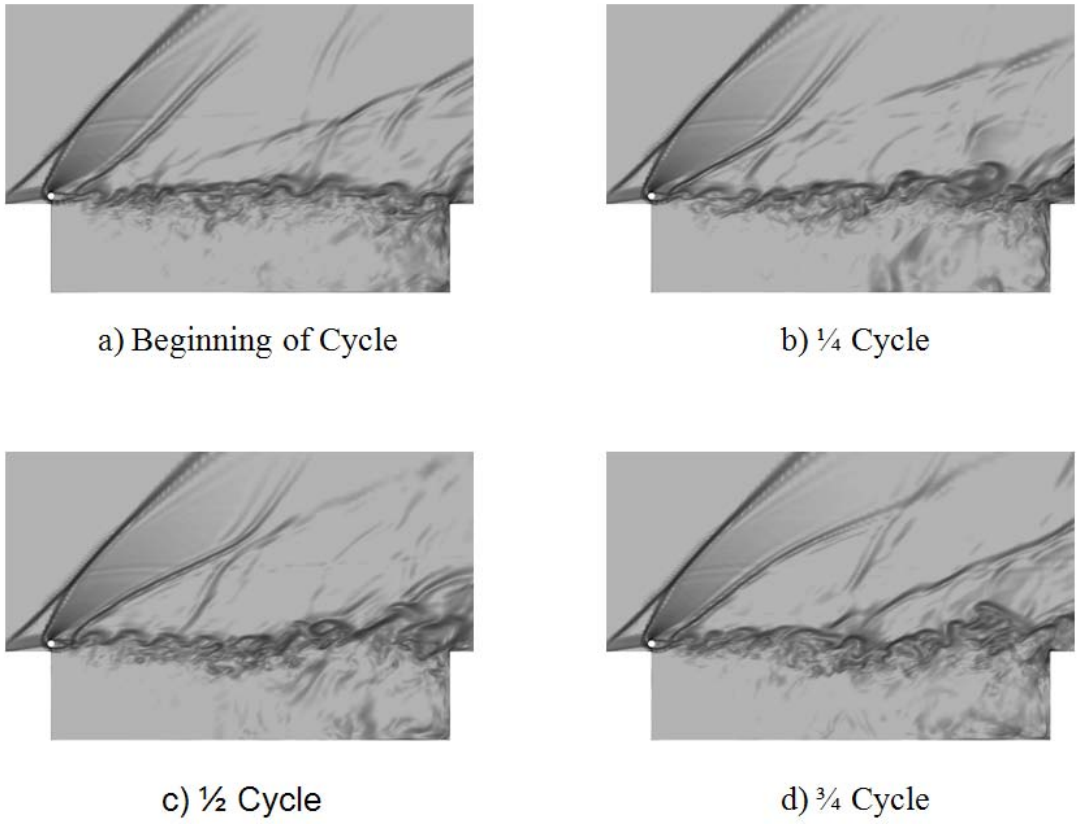

Figure 5.5 – Computed Pseudo-Schleiren Images of Dominant Third Rossiter Tone of Single Rod Configuration

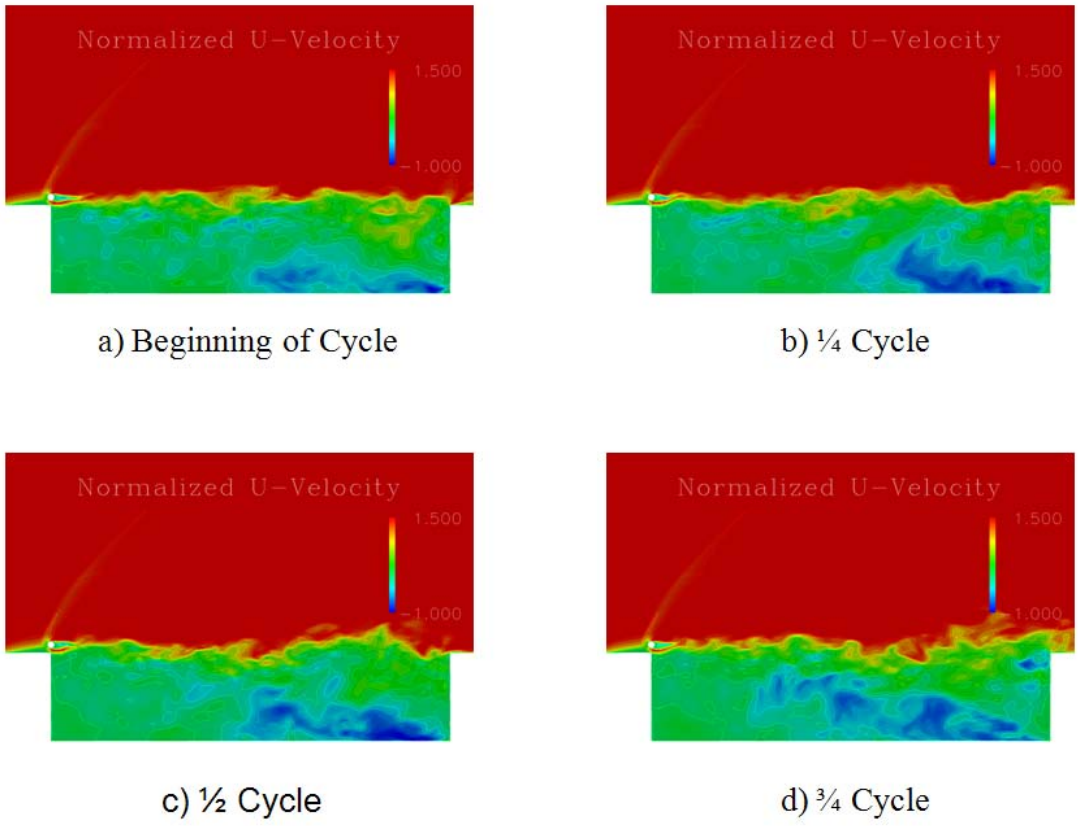

Figure 5.6 – Computed U-velocity Contour of Dominant Third Rossiter Tone of Single Rod Configuration

While there are geometric dissimilarities between the computational model and Stanek's experiment, shedding was observed with the single rod configuration. However, the level of acoustic suppression claimed by Stanek [25] in his experiments with the rod in crossflow was not reproduced in the computational model. These results could lend credence to the claim of Illy, et al. [33] that the suppression is purely geometric, and the high level of suppression observed by Stanek was not observed due to slight discrepancies in the computational and experimental models.

Chapter 6

INCLINED FENCE CONFIGURATION

6.1 Design

In order to complete the parametric study, the remaining component of the proposed configuration, the forty-five degree fence, was examined as a standalone device. As previously stated, this task was performed in an attempt to isolate the driving mechanism in the acoustic suppression observed in the complex configuration. A grid system comprised of only the fence was constructed. To construct the new grid system, the large "shedding" rod was simply removed from the previous combined grid system, and new interpolations and hole cutting were carried out with Pegasus 5. The new grid system is shown in Figure 6.1.

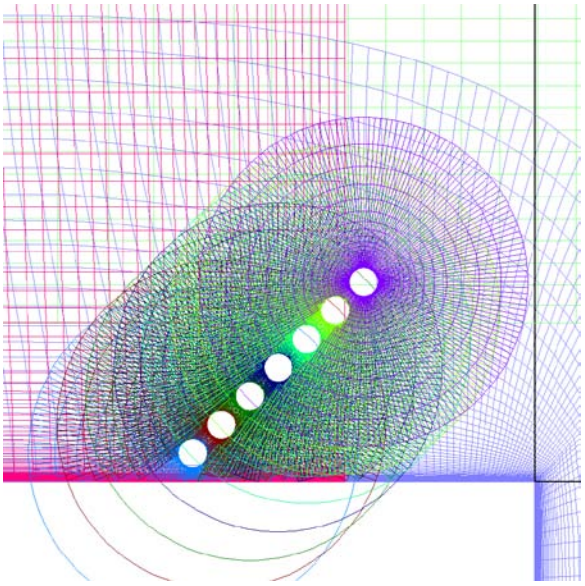

Figure 6.1 – Computational Model of Forty Five Degree Fence Configuration

After the new grid was constructed, a simulation was performed using the same flow inputs as the previous three cases. Data was once again collected at each of the microphone locations as the previous model and overall sound pressure levels and spectral results were calculated using the aforementioned scripts.

6.2 Calculations and Comparison To Baseline

The results of the forty five degree fence calculations are shown in Table 6.1 and Figure 6.2. When compared to the baseline clean configuration, the forty five degree fence was calculated to have an average sound pressure reduction of approximately 3.7 decibels. This calculated value was shown to be appreciably less than the 7.6 decibels average reduction observed with the combined configuration in which the single rod and fence work together in tandem.

Table 6.1 – Comparison of OASPL of Forty Five Degree Fence Model to Clean Computational Model

OASPL (dB)			
Sensor	**Clean**	**45° Fence**	**ΔdB**
K5	155.6	154.2	-1.4
K6	154.1	153.2	-0.9
K7	152.8	151.5	-1.4
K8	153.2	148.3	-4.9
K9	154.6	147.9	-6.7
K10	154.7	147.6	-7.1
K11	156.3	153.3	-3.0
K12	159.1	156.0	-3.1
K13	161.0	157.9	-3.2
K37	162.4	158.8	-3.6
K38	162.6	158.5	-4.1
K39	162.8	157.5	-5.3
K40	163.1	157.1	-6.0
K41	162.9	157.3	-5.5
K42	163.3	159.9	-3.4
K14	163.7	161.4	-2.4
K15	165.4	163.7	-1.6
K16	168.7	166.1	-2.5
Average			-3.7

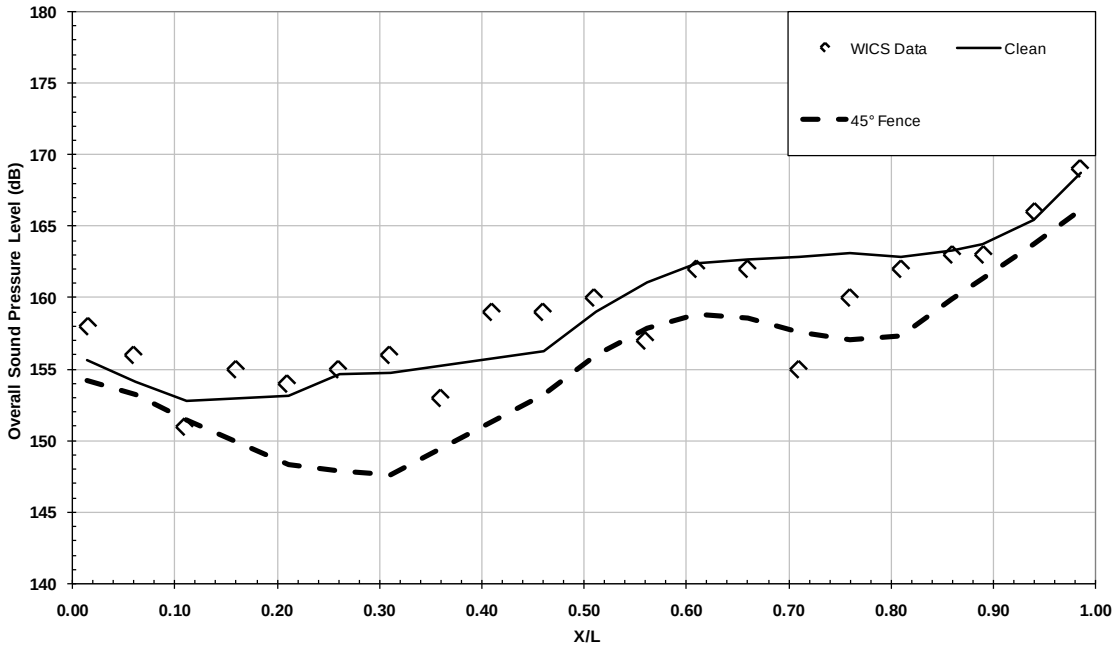

Figure 6.2 – OASPL Comparison of Clean Computational Model, Forty Five Degree Fence Configuration and WICS Experimental Model

Figure 6.3 shows a significant reduction in sensor K16 sound pressure around the 1st Rossiter tone of 240 Hz and a quantifiable reduction in the 4th and 5th tones of approximately 1260 Hz and 1600 Hz. But there was negligible reduction in the 2nd Rossiter tone and little or no reduction in the dominant 3rd tone. The time varying pressure and computed power spectral density are shown in Figures 6.3(a) and 6.3(b). The power spectral density plot of the forty-five degree fence configuration also shows the reduction in energy in each of the aforementioned tones.

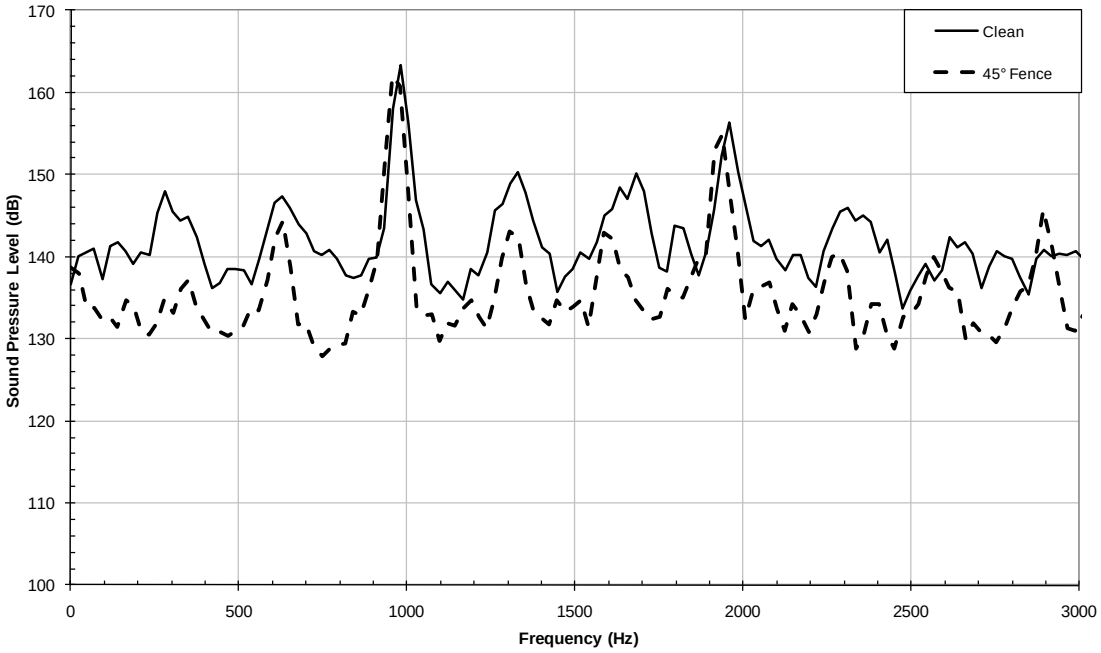

Figure 6.3 – Computed Sound Pressure Level vs. Frequency Comparison of Clean Computational Model to Forty Five Degree Fence Configuration

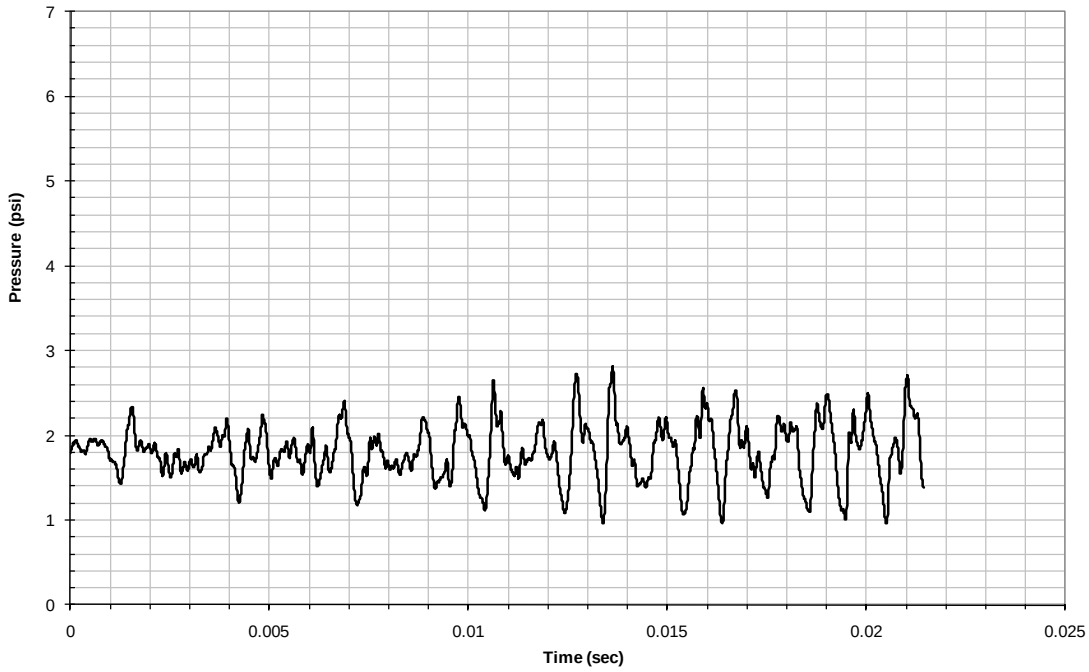

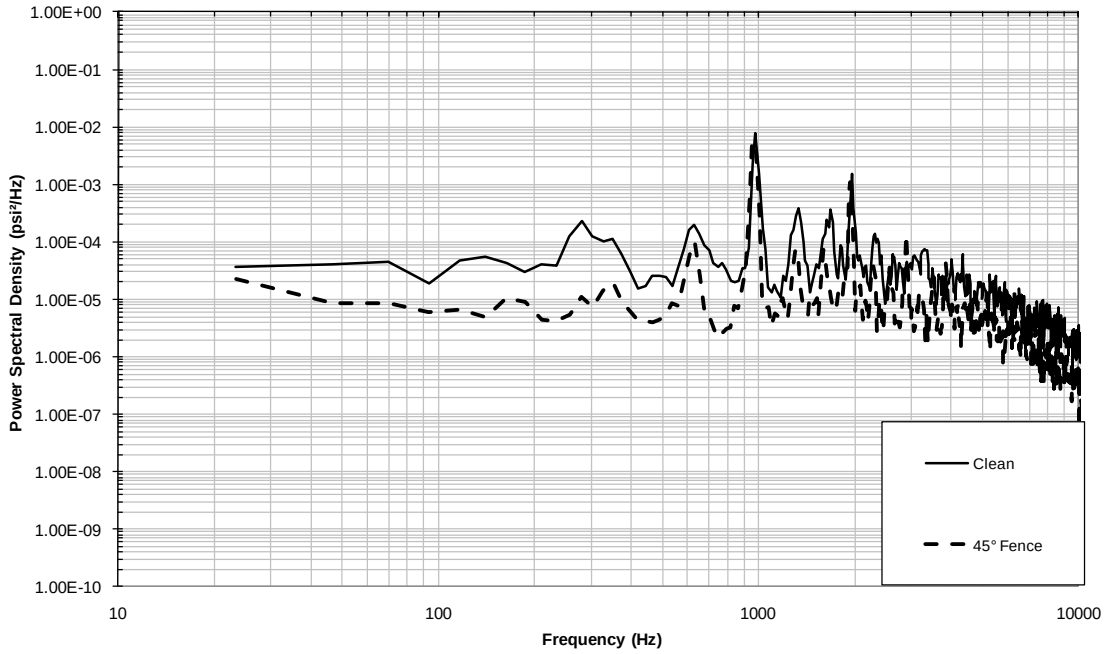

Figure 6.4 – (a) Computed Raw Pressure at Sensor K16 of Forty Five Degree Fence Configuration (b) Computed Power Spectral Density vs. Frequency Comparison of Clean Computational Model to Forty Five Degree Fence Configuration

In Figures 6.5 and 6.6 the computed pseudo-Schleiren and u-velocity contours of the forty-five degree fence are shown. In Figure 6.5 there appears to be a large structure interacting with the rear cavity wall at the quarter-cycle, and a pressure wave emitting from the corner at the half cycle and continuing to radiate outward at the three-quarter cycle. In Figure 6.6, the adverse velocity gradient observed in the rear of the cavity seems to dissipate while mixing with the shear layer, and appears to cause a large wave in the shear layer near the aft cavity wall at the three-quarter cycle. Based upon these results, it can be stated that while the forty-five degree fence does in fact reduce the sound pressure at several of the predicted Rossiter tones, it is not as effective as a standalone device.

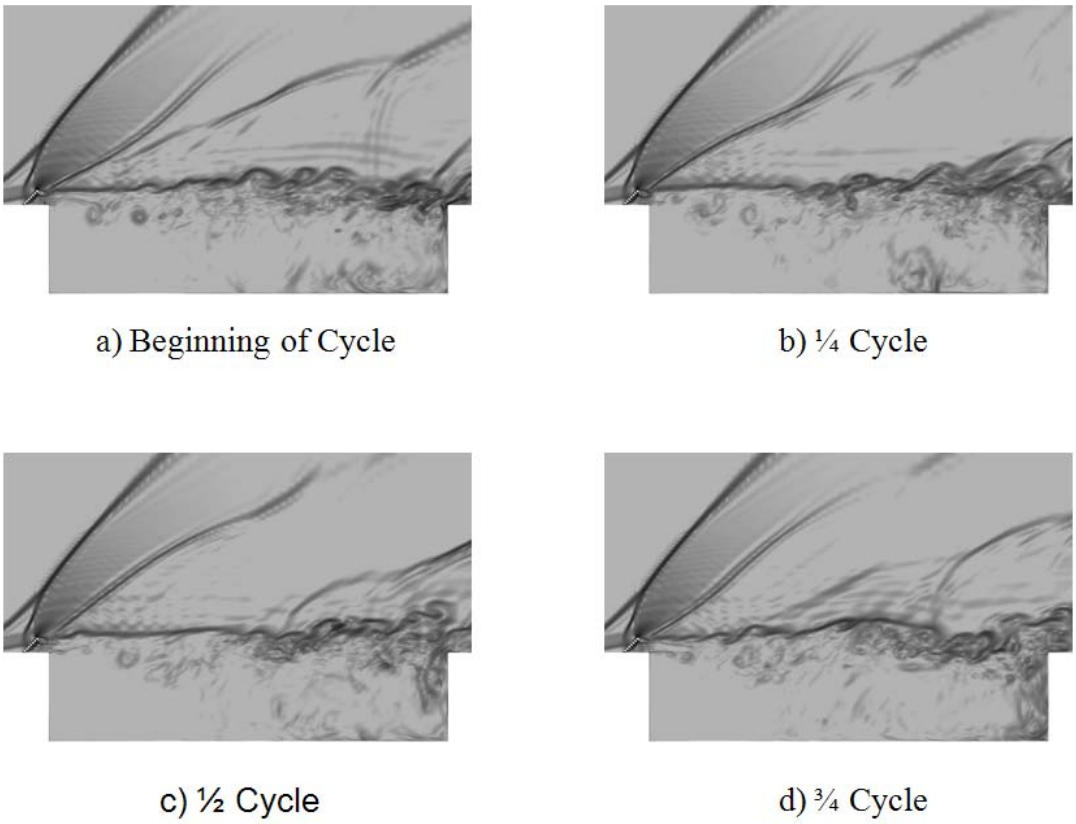

Figure 6.5 – Computed Pseudo-Schleiren Images of Dominant Third Rossiter Tone of Forty Five Degree Fence Configuration

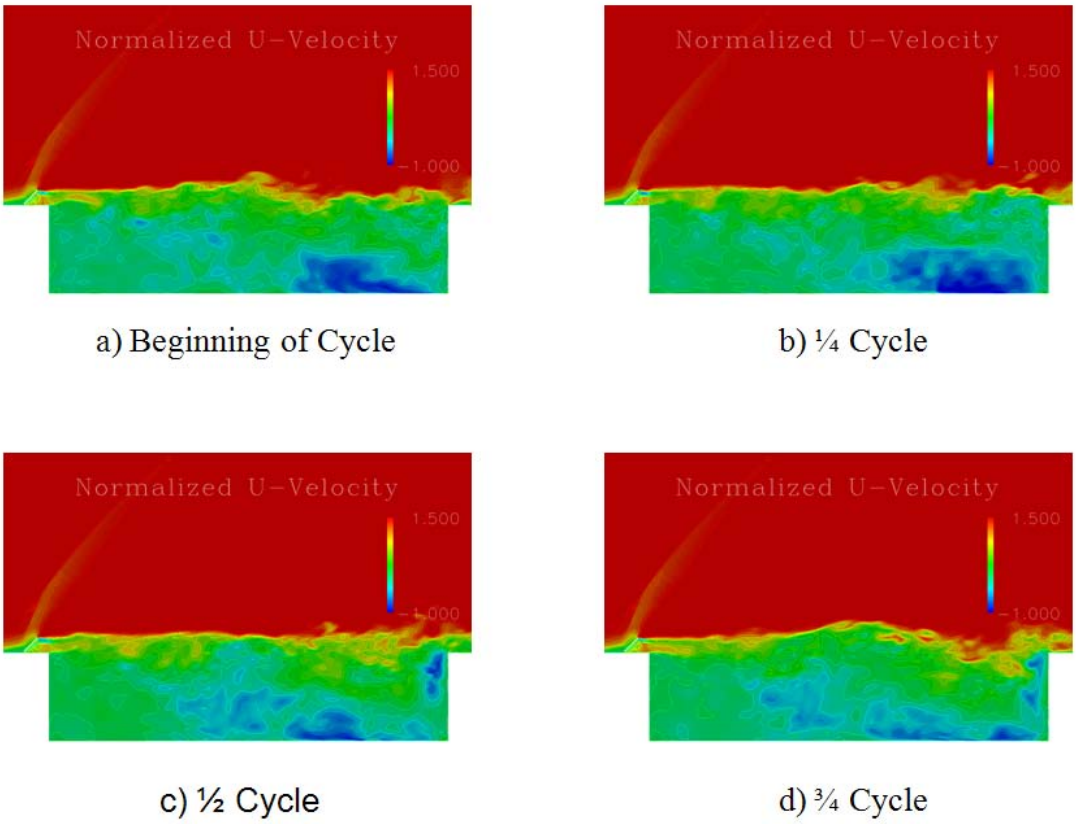

a) Beginning of Cycle

b) ¼ Cycle

c) ½ Cycle

d) ¾ Cycle

Figure 6.6 – Computed U-velocity Contours of Dominant Third Rossiter Tone of Forty Five Degree Fence Configuration

Chapter 7

MODIFIED COMBINED CONFIGURATION

7.1 Design

Based on the parametric study of the combined configuration and each of the components, a modification to the design was proposed based upon visual inspection of the flowfield velocity vectors. This chapter covers discusses the modified design and its resultant performance.

While analyzing the results from the forty-five degree fence and shedding rod configuration, a visual inspection of the time averaged flowfield velocity vectors, shown in Figure 7.1, was performed. It was proposed that by removing one or more of the small rods from the bottom of the fence configuration and adding one or more small rods to the top, additional upward advection of flow could be encouraged by entraining higher momentum flow to the underside of the large rod. Also, examination of the Mach contour image of Figure 7.2 suggested that adding rods to the top of the fence could possibly provide some relief of the expansion fan on the downstream side of the fence which appears to be forcing the flow into the rear of the cavity.

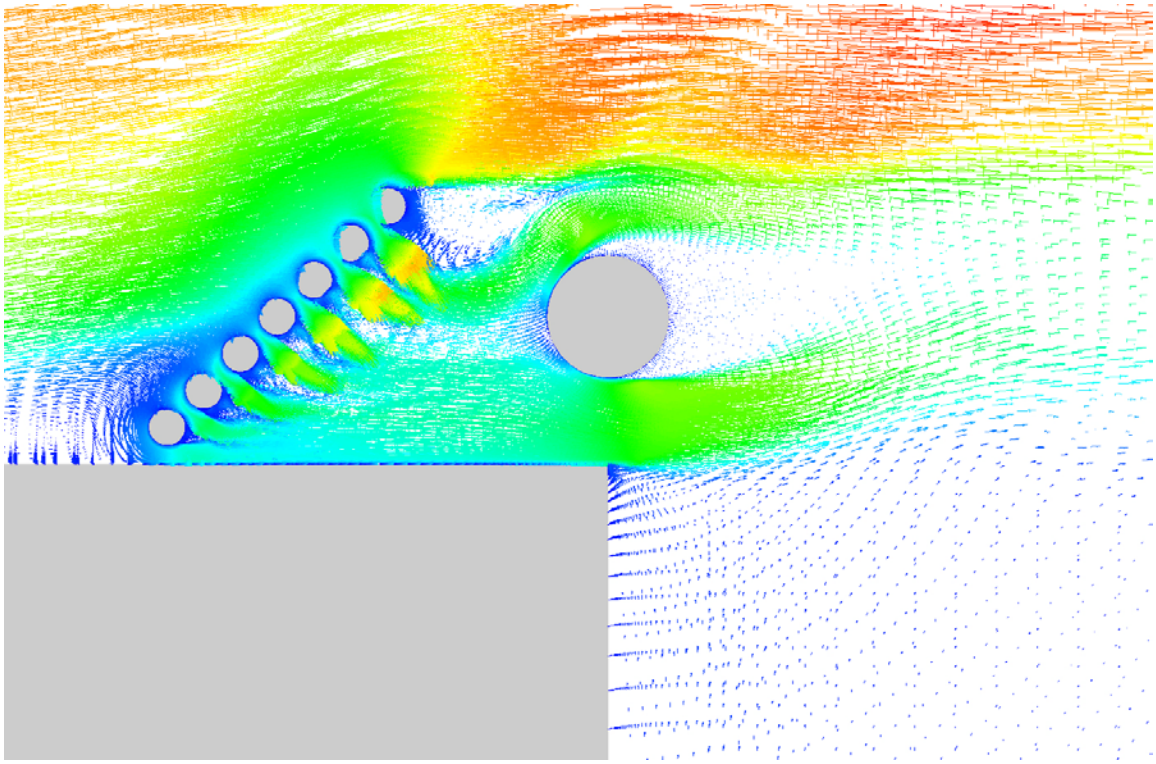

Figure 7.1 – Computed Vectors of Velocity Magnitude of Combined Configuration

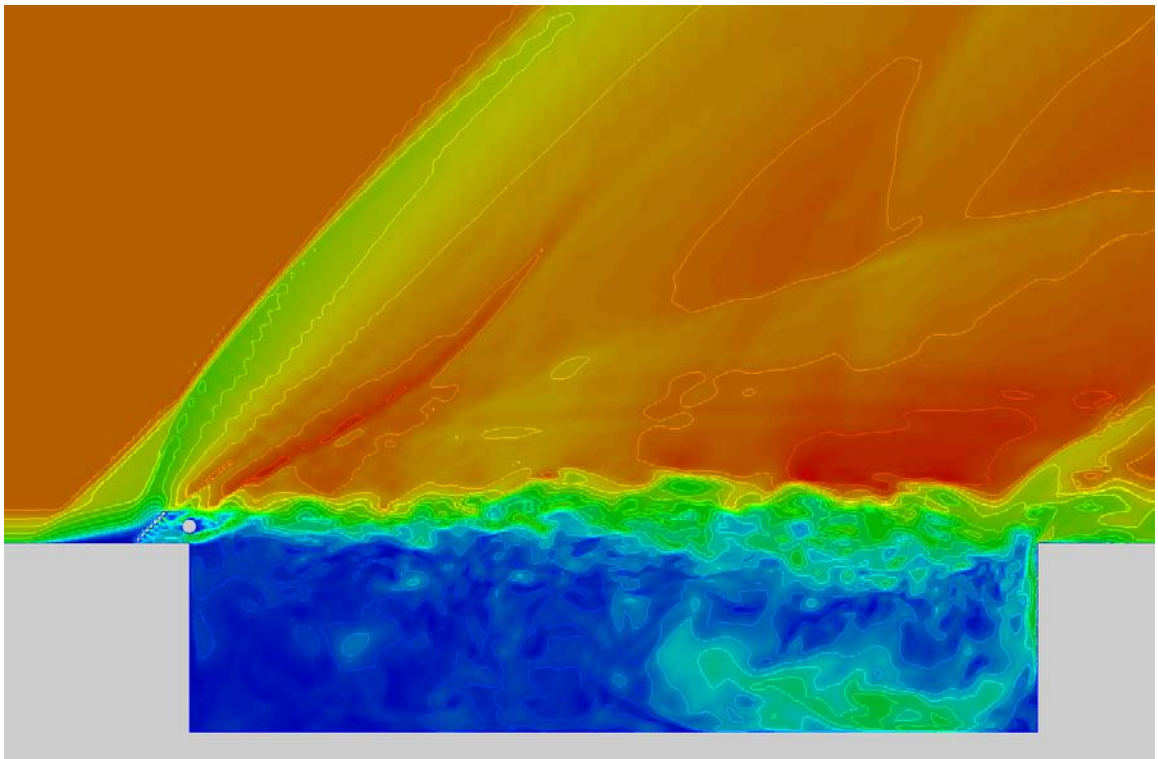

Figure 7.2 – Computed Mach Number Contours of Combined Configuration

In order to promote flow underneath the large rod while still providing adequate blockage of the high speed flow from interacting directly with the rod and diminishing any high frequency shedding, the decision was made to remove two of the small rods from the bottom of the fence and add one rod to the top of the fence. The addition of the rod to the top of the fence increased deflection of the flow and provided relief to the shear layer from the expansion on the downstream side of the rod fence all while maintaining a low profile. Any additional height would be undesirable. The new modified design is shown in Figure 7.3.

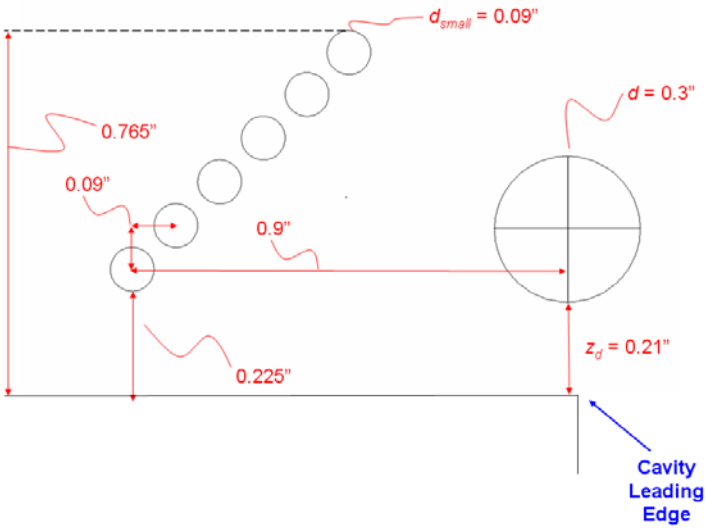

Figure 7.3 – Detailed Schematic of Modified Design

The new grid system was assembled and pre-processed using Pegasus 5. A close-up of the new design grid is shown in Figure 7.4. As with all the previous simulations, the same OVERFLOW2 inputs were used, and data was taken at each of the same points as the baseline configuration.

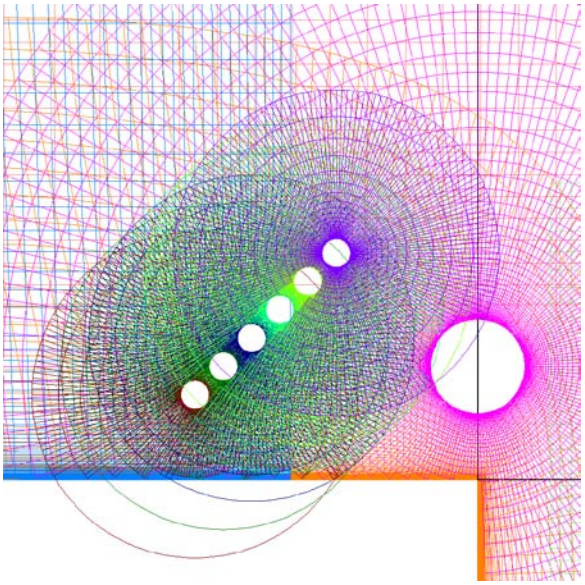

Figure 7.4 – Computational Model of Modified Design

7.2 Calculations and Comparison to Baseline

Post processing of the data was once again performed for each of the 18 microphone locations and the overall sound pressure level and power spectral density at each was calculated and compared to the baseline clean configuration. The results of these calculations can be seen in Table 7.1 and Figures 7.5 to 7.7. Figure 7.5 shows that the modified design reduces the average sound pressure level at each of the microphone locations by 7.3 dB. This is slightly less than the 7.6 dB reduction of the original combined configuration.

Table 7.1 – Comparison of OASPL of Design Iteration Model to Clean Computational Model

OASPL (dB)			
Sensor	**Clean**	**Fence 45 +Rod v2**	**ΔdB**
K5	155.6	149.0	-6.6
K6	154.1	147.6	-6.5
K7	152.8	146.5	-6.3
K8	153.2	146.0	-7.1
K9	154.6	146.4	-8.2
K10	154.7	146.2	-8.5
K11	156.3	150.4	-5.9
K12	159.1	152.5	-6.6
K13	161.0	154.0	-7.1
K37	162.4	154.7	-7.7
K38	162.6	154.8	-7.9
K39	162.8	154.6	-8.2
K40	163.1	154.6	-8.5
K41	162.9	154.9	-8.0
K42	163.3	155.9	-7.4
K14	163.7	156.7	-7.0
K15	165.4	158.8	-6.6
K16	168.7	161.5	-7.2
Average			-7.3

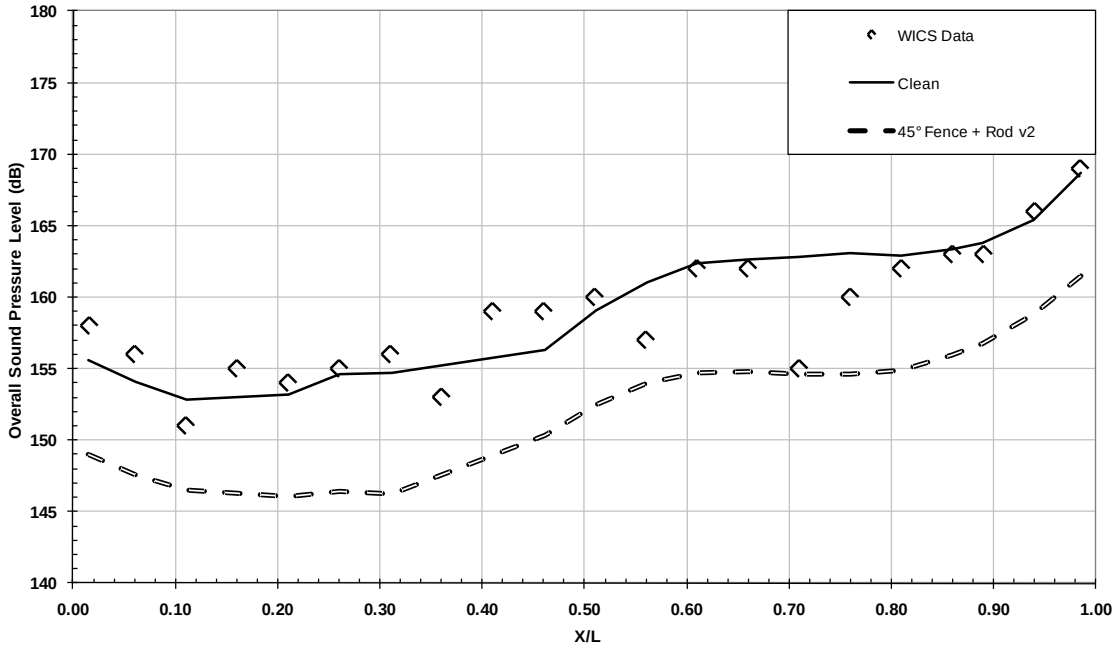

Figure 7.5 – OASPL Comparison of Clean Computational Model, Design Iteration Configuration and WICS Experimental Model

The power spectral density plot at sensor K16 (Figure 7.6) shows a reduction in each of the Rossiter tones at the K16 sensor, with the highest being a 10 decibel reduction in the 1st tone, and an approximate 7 decibel reduction in the dominant 3rd tone. The time carrying pressure and computed power spectral density are shown in Figures 7.7(a) and 7.7(b).

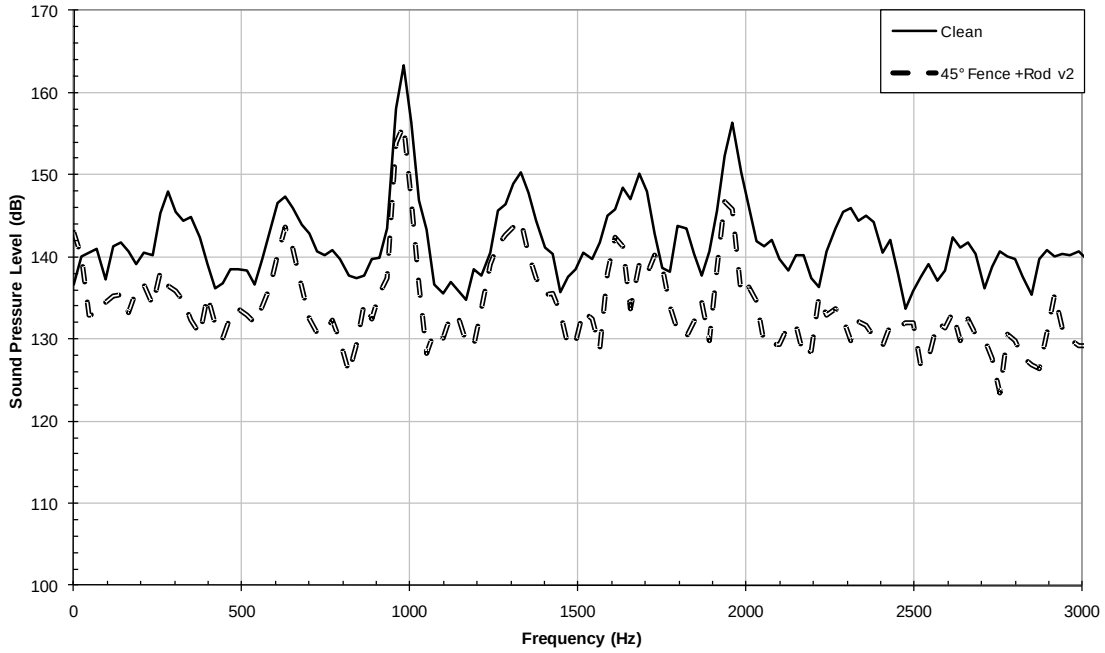

Figure 7.6 – Computed Sound Pressure Level vs. Frequency Comparison of Clean Computational Model to Design Iteration Configuration

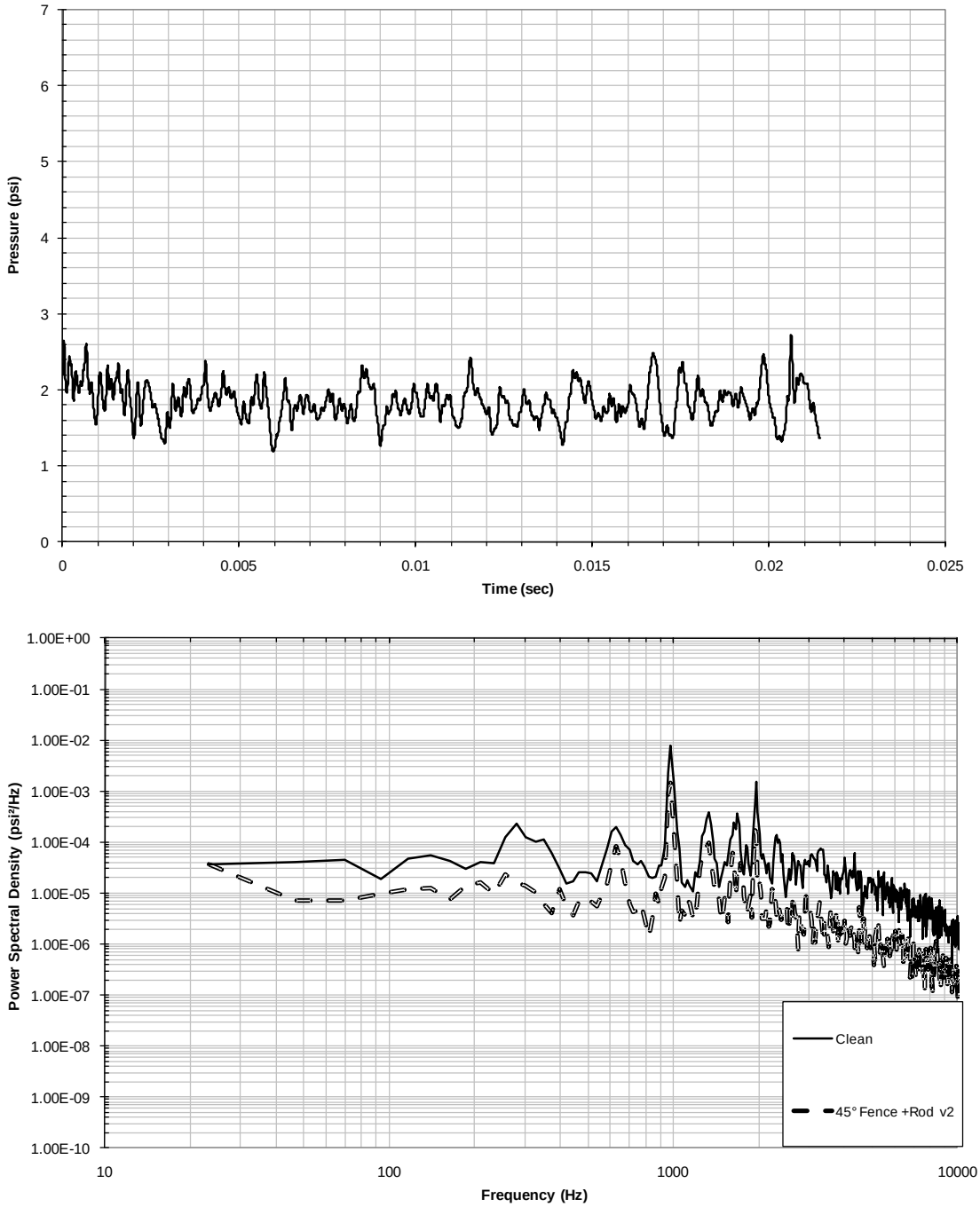

Figure 7.7 – (a) Computed Raw Pressure at Sensor K16 of Design Iteration Configuration (b) Computed Power Spectral Density vs. Frequency Comparison of Clean Computational Model to Design Iteration Configuration

Figures 7.8 and 7.9 show the computed pseudo-Schleiren and the u-velocity contours of an approximate cycle of the dominant third Rossiter tone of the modified configuration. Analysis of the pseudo-Schleiren revealed what appeared to be shedding

much like the shedding observed in the original combined configuration. The u-velocity contours also show the desired lofting from higher momentum flow channeled underneath the forty-five degree fence and rod. However, large structures were still observed in Figure 7.8 and large undulations were observed in Figure 7.9.

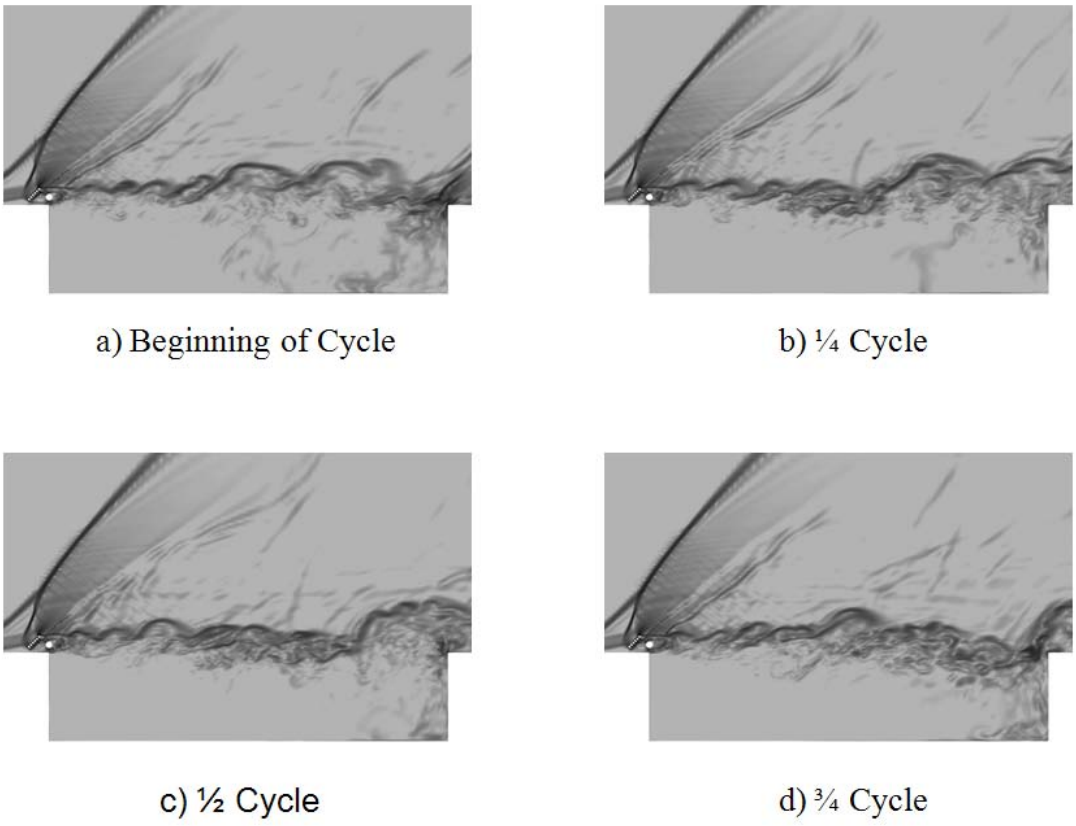

Figure 7.8 – Computed Pseudo-Schleiren Images of Dominant Third Rossiter Tone of Modified Design

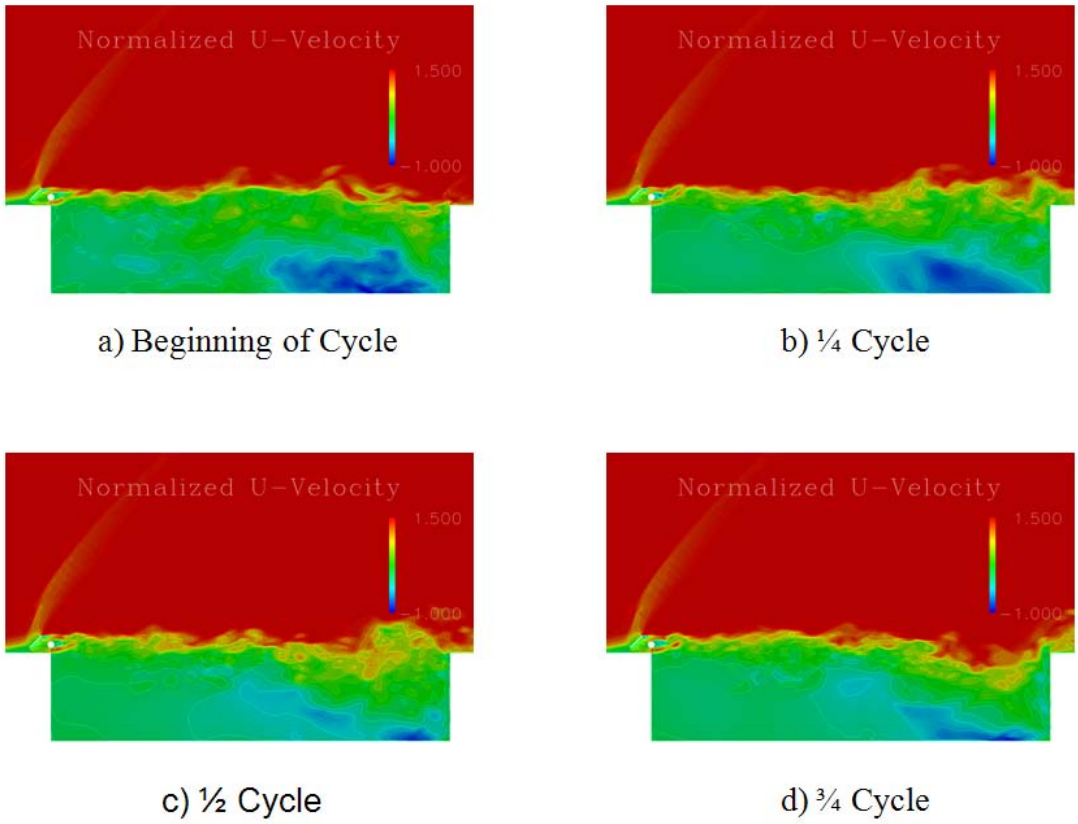

Figure 7.9 – Computed U-velocity Contour of Dominant Third Rossiter Tone of Modified Design

Based upon these results it seems that there is no added benefit with the modified design. When compared to the original proposed configuration, there is no real quantifiable reduction in OASPL at any of the eighteen sensors. Table 7.2 shows the OASPL comparison between the original combined configuration and the modified design which shows an average increase of approximately 0.4 decibels along the cavity floor. Figure 7.10 shows that the modified configuration may slightly reduce the OASPL below the original configuration only in the center of the cavity.

Table 7.2 – Comparison of OASPL of Design Iteration Model to Modified Design

OASPL (dB)			
Sensor	**Fence 45 +Rod**	**Fence 45 +Rod v2**	**ΔdB**
K5	148.4	149.0	0.6
K6	146.8	147.6	0.8
K7	145.6	146.5	0.9
K8	145.4	146.0	0.6
K9	145.6	146.4	0.8
K10	144.9	146.2	1.4
K11	150.4	150.4	0.0
K12	152.9	152.5	-0.4
K13	154.4	154.0	-0.4
K37	155.1	154.7	-0.4
K38	154.9	154.8	-0.2
K39	154.5	154.6	0.1
K40	154.2	154.6	0.4
K41	154.5	154.9	0.3
K42	155.6	155.9	0.3
K14	156.4	156.7	0.4
K15	158.4	158.8	0.3
K16	160.6	161.5	0.9
Average			0.4

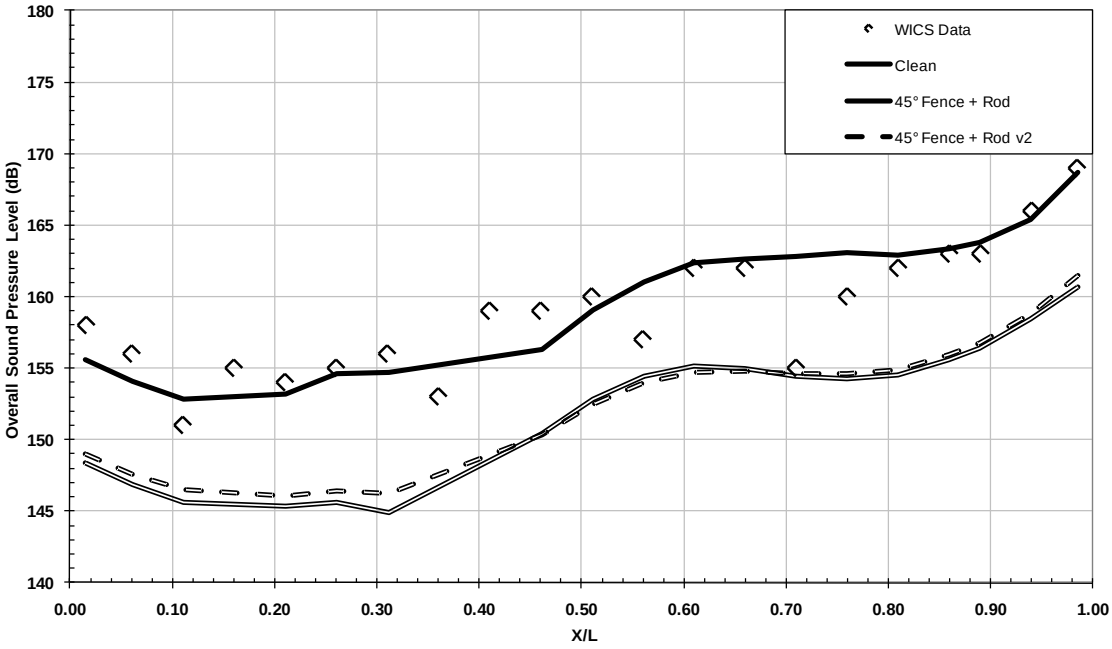

Figure 7.10 – OASPL Comparison of Clean Computational Model, Proposed Configuration, Design Iteration Configuration and WICS Experimental Model

The computed sound pressure levels and power spectral density at the aft cavity wall for the clean cavity, original fence-rod configuration, and the modified fence-rod configuration are compared in Figures 7.11 and 7.12. The modified configuration appears to reduce the peaks of the first and second Rossiter tones at the K16. However, there is little or no reduction in the dominant third tone or the 4th tone. Figure 7.12 shows that the energy spectrum is very similar between the original combined configuration and the modified design. The only observable difference is a slight increase in the energy of the second tone with the modified configuration. These results show that there is significant difference between the original and modified fence-rod configurations.

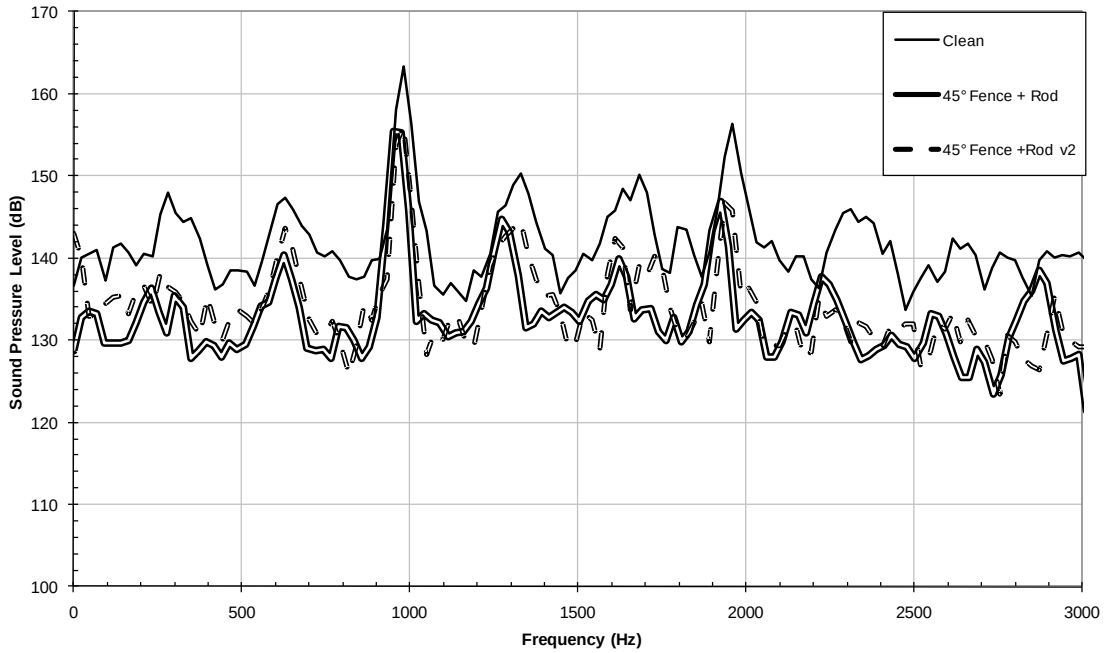

Figure 7.11 – Computed Sound Pressure Level vs. Frequency Comparison of Proposed Configuration, Modified Design Configuration and Clean Computational Model

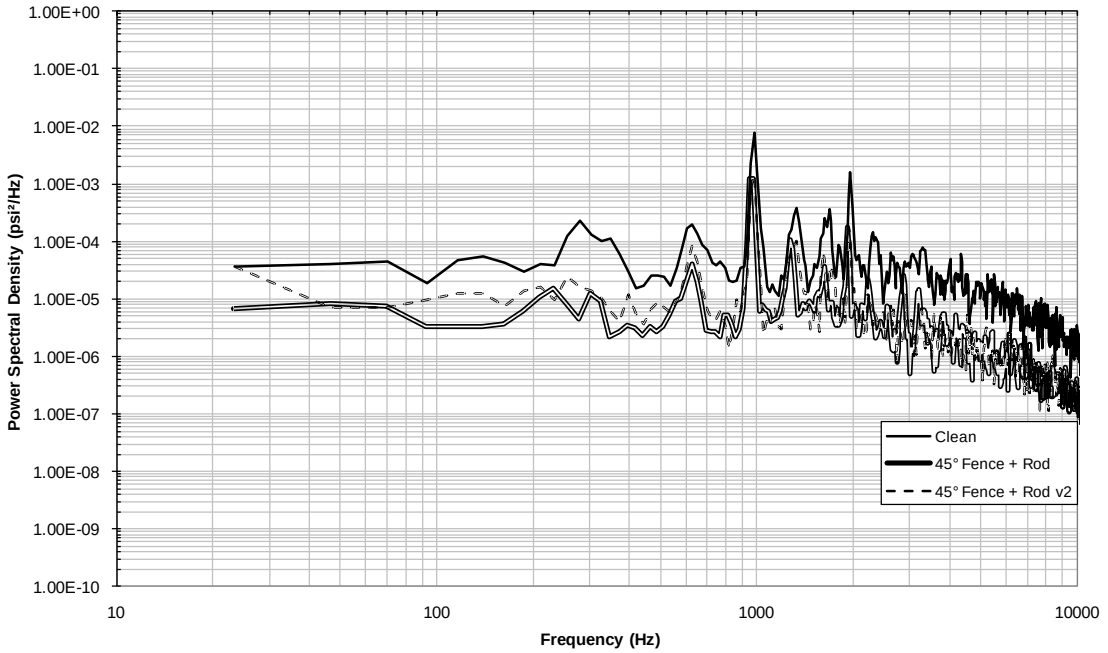

Figure 7.12 – Computed Power Spectral Density vs. Frequency Comparison of Proposed Configuration, Modified Design Configuration and Clean Computational Model

Chapter 8

SUMMARY AND CONCLUSIONS

In this thesis a novel approach to suppressing cavity flow oscillations in high-speed flow was investigated. It was proposed that a multi-faceted approach be taken, encompassing two of the most proven ways of controlling cavity flow oscillations: shear layer displacement and high frequency shear layer forcing. This was accomplished by placing a rod in crossflow over the leading edge of the cavity with a forty-five degree rod fence placed upstream of the cavity. With this configuration, it was believed that the forty-five degree rod fence would act as a spoiler, lofting the shear layer above the rear wall of the cavity, while the aft rod, immersed in the subsonic flow in the wake of the fence, would induce high-frequency shedding in its wake. This, it was believed, would further disrupt the formation of coherent vortical structures believed to be a primary cause of high energy cavity flow oscillations.

A baseline, clean cavity computational model was first created. The baseline computational model results were qualitatively compared to historical experimental data for cavity flow. The computational model accurately captures the theoretical cavity modes predicted by the modified Rossiter equation to within an average of 7% over the first six modes. Also, the overall sound pressure levels at 18 different locations along the cavity floor were predicted to within a 5% maximum deviation.

Once the baseline clean cavity model was qualitatively validated against experimental data, the proposed combined configuration was implemented into the computational model and sound pressure levels at the eighteen different microphone

locations were calculated. The combined configuration was computationally shown to reduce the peak sound pressure level by approximately 8 decibels at the loudest cavity position near the aft wall (sensor K16) and by an average of 7.6 decibels along the entire cavity floor. The combined configuration was also shown to reduce sound pressure levels at each of the predicted Rossiter modes at the rear of the cavity.

The results for the combined forty-five degree fence and shedding rod configuration were promising, and a parametric study was performed in an attempt to isolate the source of the reduction. The large shedding rod was first evaluated as a standalone device. Data was computed throughout the simulation at the same eighteen microphone locations as the proposed configuration. After post-processing the results, an average reduction of only approximately 4 decibels was observed along the length of the cavity floor.

The forty-five degree fence alone was next analyzed. While the fence showed an average reduction of approximately 3 decibels along the cavity floor, there was little reduction in the peak Rossiter modes and very little energy dissipated at the aft cavity wall. These results showed that the combined approach was needed to attain the full acoustic suppression.

A modification to the original configuration was proposed based upon inspection of the flowfield velocity vectors. It was hypothesized that by slightly changing the original configuration, an added reduction in sound pressure level could be achieved. The design modification consisted of adding one rod to the top of the forty-five degree rod fence, while removing two rods from the bottom. The intention was to inhibit the expansion fan on the downstream side of the fence from impinging on the shear layer and

forcing it into the rear of the cavity, while also promoting a lofting of the shear layer by entraining higher momentum flow to the underside of the large shedding rod. The new configuration was then analyzed in the same fashion as the other configurations. Pressures and sound pressure levels were computed at the same eighteen sensor locations and compared to the baseline clean cavity model. An average reduction of 7.3 decibels was observed along the entire length of the cavity, including a reduction of approximately 7 decibels in the dominant 3rd Rossiter mode at the aft cavity wall sensor K16. As in the original combined configuration, a substantial reduction in sound pressure level and energy content was observed at each of the predicted Rossiter modes. Based upon these results, it was determined that there was no added benefit to the modification of the original proposed configuration while there was an undesirable increase in the height of the configuration.

In conclusion, while the reduction of cavity acoustic radiation by use of a single rod in crossflow was demonstrated by Stanek in supersonic flow, the results proved to be irreproducible in further experimentation by others as well as in the computational results obtained during the course of this analysis. The research discussed in this thesis suggests that a two-phase approach to controlling cavity oscillations is viable. However, while the proposed configuration provided a significant reduction in the acoustic radiation of the cavity, further research should be performed in order to better understand the mechanism of suppression. Some of the future works should include performing a sound directivity study to indicate the direction in which energy is propagating from the source, sizing the shedding rod based upon the dominant 3rd Rossiter tone instead of the 4th, varying the z_d/d ratio provided by Illy, et al., and investigation of the suppressive capabilities at different

Mach numbers. Through this future work, the suppression mechanism may be better understood and may lead to refinement of the design and/or approach to acoustic suppression.

APPENDICES

APPENDIX A

OVERFLOW2 Inputs

A.1 – Steady State Startup Input

```
$GLOBAL
     CHIMRA = .T.,
     INCORE = .T.,
     NSTEPS = 5000,
     RESTRT = .F.,
     NSAVE = -2500,
     NFOMO = 1,
     ISTART_QAVG = 10000
     NQT = 205,
     NQC = 0,
     MULTIG = .F.,
     FMG = .F.,
     NGLVL = 3,
     FMGCYC = 150,150,
     DTPHYS = 0,
     $END

 $FLOINP
     ALPHA = 0.0,
     BETA = 0.0,
     FSMACH = 1.75,
     GAMINF = 1.4,
     REY = 191667.,
     PR = 0.7,
     PRT = 0.92,
     TINF = 344.8,
     $END

 $VARGAM
     $END


 $GRDNAM
     NAME = 'CAVITY_CORE',
     $END
 $NITERS
     $END
 $METPRM
     IRHS = 4, ILHS = 5,
     $END
 $TIMACU
     ITIME = 3, DT = 0.01,   CFLMIN = 1.0, CFLMAX = 2.0,
     $END
 $SMOACU
```

```
    DIS2 = 2.0, DIS4 = 0.1, SMOO = 0.0, FSO = 2.0,
    $END
$VISINP
    VISC  = .T.,  IDES = 1, IRC = 2,
    $END

$BCINP
   IBTYP =     5,    1,   1,
   IBDIR =     2,    3,  -3,
   JBCS  =     1,    1,   1,
   JBCE  =    -1,   -1,  -1,
   KBCS  =     1,    1,   1,
   KBCE  =     1,   -1,  -1,
   LBCS  =     1,    1,  -1,
   LBCE  =    -1,    1,  -1,
    $END
$SCEINP
    $END
$SIXINP
    $END

$GRDNAM
    NAME = 'CAVITY_FARFIELD',
    $END
$NITERS
    $END
$METPRM

    $END
$TIMACU

    $END
$SMOACU

    $END
$VISINP

    $END
$BCINP
   IBTYP =    47,    1,  1,
   IBDIR =    -2,    3, -3,
   JBCS  =     1,    1,  1,
   JBCE  =    -1,   -1, -1,
   KBCS  =    -1,    1,  1,
   KBCE  =    -1,   -1, -1,
   LBCS  =     1,    1, -1,
   LBCE  =    -1,    1, -1,
    $END
$SCEINP
    $END
$SIXINP
    $END

$GRDNAM
    NAME = 'COLLAR_AFT',
    $END
$NITERS
```

```
    $END
$METPRM

    $END
$TIMACU

    $END
$SMOACU

    $END
$VISINP

    $END
$BCINP
   IBTYP =     5,    5,    1,  1,
   IBDIR =    -2,   -1,    3, -3,
   JBCS  =     1,   -1,    1,  1,
   JBCE  =    -1,   -1,   -1, -1,
   KBCS  =    -1,    1,    1,  1,
   KBCE  =    -1,   -1,   -1, -1,
   LBCS  =     1,    1,    1, -1,
   LBCE  =    -1,   -1,    1, -1,
    $END
$SCEINP
    $END
$SIXINP
    $END

$GRDNAM
    NAME = 'COLLAR_FWD',
    $END
$NITERS
    $END
$METPRM

    $END
$TIMACU

    $END
$SMOACU

    $END
$VISINP

    $END
$BCINP
   IBTYP =     5,    5,    1,  1,
   IBDIR =    -2,    1,    3, -3,
   JBCS  =     1,    1,    1,  1,
   JBCE  =    -1,    1,   -1, -1,
   KBCS  =    -1,    1,    1,  1,
   KBCE  =    -1,   -1,   -1, -1,
   LBCS  =     1,    1,    1, -1,
   LBCE  =    -1,   -1,    1, -1,
    $END
$SCEINP
    $END
```

```
$SIXINP
    $END

$GRDNAM
    NAME = 'PLATE_AFT',
    $END
$NITERS
    $END
$METPRM

    $END
$TIMACU

    $END
$SMOACU

    $END
$VISINP

    $END
$BCINP
   IBTYP =     5,   30,    1,  1,  47,
   IBDIR =    -2,    1,    3, -3,   2,
   JBCS  =     1,    1,    1,  1,   1,
   JBCE  =    -1,    1,   -1, -1,  -1,
   KBCS  =    -1,    1,    1,  1,   1,
   KBCE  =    -1,   -1,   -1, -1,   1,
   LBCS  =     1,    1,    1, -1,   1,
   LBCE  =    -1,   -1,    1, -1,  -1,
    $END
$SCEINP
    $END
$SIXINP
    $END

$GRDNAM
    NAME = 'PLATE_FWD',
    $END
$NITERS
    $END
$METPRM

    $END
$TIMACU

    $END
$SMOACU

    $END
$VISINP

    $END
$BCINP
   IBTYP =     5,   47,    1,   47,  1,
   IBDIR =    -2,   -1,    3,    2, -3,
   JBCS  =     1,   -1,    1,    1,  1,
   JBCE  =    -1,   -1,   -1,   -1, -1,
```

```
   KBCS  =    -1,    1,    1,    1,  1,
   KBCE  =    -1,   -1,   -1,    1, -1,
   LBCS  =     1,    1,    1,    1, -1,
   LBCE  =    -1,   -1,    1,   -1, -1,
    $END
 $SCEINP
    $END
 $SIXINP
    $END
```

A.2 – Time Accurate Input

```
$GLOBAL
     CHIMRA = .T.,
     INCORE = .T.,
     NSTEPS = 25000,
     RESTRT = .T.,
     NSAVE = -1000,
     NFOMO = 1,
     ISTART_QAVG = 10000
     NQT = 205,
     NQC = 0,
     MULTIG = .F.,
     FMG = .F.,
     NGLVL = 3,
     FMGCYC = 150,150,
     NITNWT = 5,
     DTPHYS = 0.10,
     $END

 $FLOINP
     ALPHA = 0.0,
     BETA = 0.0,
     FSMACH = 1.75,
     GAMINF = 1.4,
     REY = 191667.,
     PR = 0.7,
     PRT = 0.92,
     TINF = 344.8,
     $END

 $VARGAM
     $END

 $GRDNAM
     NAME = 'CAVITY_CORE',
     $END
 $NITERS
     $END
 $METPRM
     ILHS = 5, IRHS = 4, ILIMIT = 4,
     $END
 $TIMACU
     ITIME = 3, DT = 1.0, CFLMIN = 10.0, CFLMAX = 10.0,
     $END
```

```
$SMOACU
    DELTA=1.2, FSO = 5.0,
    $END
$VISINP
    VISC = .TRUE., IDES = 3, IRC = 2,
    $END
$BCINP
   IBTYP =     5,    1,   1, 201,
   IBDIR =     2,    3,  -3,   2,
   JBCS  =     1,    1,   1,   1,
   JBCE  =    -1,   -1,  -1,  -1,
   KBCS  =     1,    1,   1,   1,
   KBCE  =     1,   -1,  -1,   1,
   LBCS  =     1,    1,  -1,  51,
   LBCE  =    -1,    1,  -1,  51,
   BCFILE(4)='cavity_floor_clean'
    $END
$SCEINP
    $END
$SIXINP
    $END

$GRDNAM
    NAME = 'CAVITY_FARFIELD',
    $END
$NITERS
    $END
$METPRM

    $END
$TIMACU

    $END
$SMOACU

    $END
$VISINP

    $END
$BCINP
   IBTYP =    47,    1,  1,
   IBDIR =    -2,    3, -3,
   JBCS  =     1,    1,  1,
   JBCE  =    -1,   -1, -1,
   KBCS  =    -1,    1,  1,
   KBCE  =    -1,   -1, -1,
   LBCS  =     1,    1, -1,
   LBCE  =    -1,    1, -1,
    $END
$SCEINP
    $END
$SIXINP
    $END

$GRDNAM
    NAME = 'COLLAR_AFT',
    $END
```

```
$NITERS
    $END
$METPRM

    $END
$TIMACU

    $END
$SMOACU

    $END
$VISINP

    $END
$BCINP
   IBTYP =     5,    5,    1,  1, 201,
   IBDIR =    -2,   -1,    3, -3,  -2,
   JBCS  =     1,   -1,    1,  1,  19,
   JBCE  =    -1,   -1,   -1, -1,  -1,
   KBCS  =    -1,    1,    1,  1,  -1,
   KBCE  =    -1,   -1,   -1, -1,  -1,
   LBCS  =     1,    1,    1, -1,  51,
   LBCE  =    -1,   -1,    1, -1,  51,
   BCFILE(5)='back_wall_clean'
  $END
$SCEINP
    $END
$SIXINP
    $END

$GRDNAM
    NAME = 'COLLAR_FWD',
    $END
$NITERS
    $END
$METPRM

    $END
$TIMACU

    $END
$SMOACU

    $END
$VISINP

    $END
$BCINP
   IBTYP =     5,    5,    1,  1, 201,
   IBDIR =    -2,    1,    3, -3,  -2,
   JBCS  =     1,    1,    1,  1,   1,
   JBCE  =    -1,    1,   -1, -1,  91,
   KBCS  =    -1,    1,    1,  1,  -1,
   KBCE  =    -1,   -1,   -1, -1,  -1,
   LBCS  =     1,    1,    1, -1,  51,
   LBCE  =    -1,   -1,    1, -1,  51,
   BCFILE(5)='front_wall_clean'
```

```
   $END
$SCEINP
    $END
$SIXINP
    $END

$GRDNAM
    NAME = 'PLATE_AFT',
    $END
$NITERS
    $END
$METPRM

    $END
$TIMACU

    $END
$SMOACU

    $END
$VISINP

    $END
$BCINP
   IBTYP =     5,   30,    1,  1,  47,
   IBDIR =    -2,    1,    3, -3,   2,
   JBCS  =     1,    1,    1,  1,   1,
   JBCE  =    -1,    1,   -1, -1,  -1,
   KBCS  =    -1,    1,    1,  1,   1,
   KBCE  =    -1,   -1,   -1, -1,   1,
   LBCS  =     1,    1,    1, -1,   1,
   LBCE  =    -1,   -1,    1, -1,  -1,
    $END
$SCEINP
    $END
$SIXINP
    $END

$GRDNAM
    NAME = 'PLATE_FWD',
    $END
$NITERS
    $END
$METPRM

    $END
$TIMACU

    $END
$SMOACU

    $END
$VISINP

    $END
$BCINP
   IBTYP =     5,   47,    1,   47,  1,
```

```
   IBDIR =    -2,   -1,    3,    2, -3,
   JBCS  =     1,   -1,    1,    1,  1,
   JBCE  =    -1,   -1,   -1,   -1, -1,
   KBCS  =    -1,    1,    1,    1,  1,
   KBCE  =    -1,   -1,   -1,    1, -1,
   LBCS  =     1,    1,    1,    1, -1,
   LBCE  =    -1,   -1,    1,   -1, -1,
    $END
$SCEINP
    $END
$SIXINP
    $END
```

APPENDIX B

SPL and PSD Plots at Sensors K5, K12, and K16

B.1.a – Clean Cavity SPL Plots

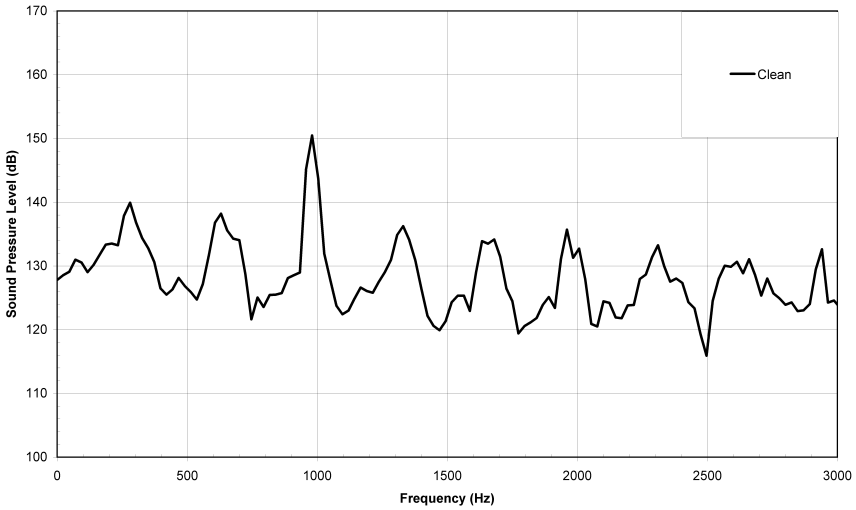

Figure B.1 – Sound Pressure Level vs Frequency of Clean Cavity K5 Sensor

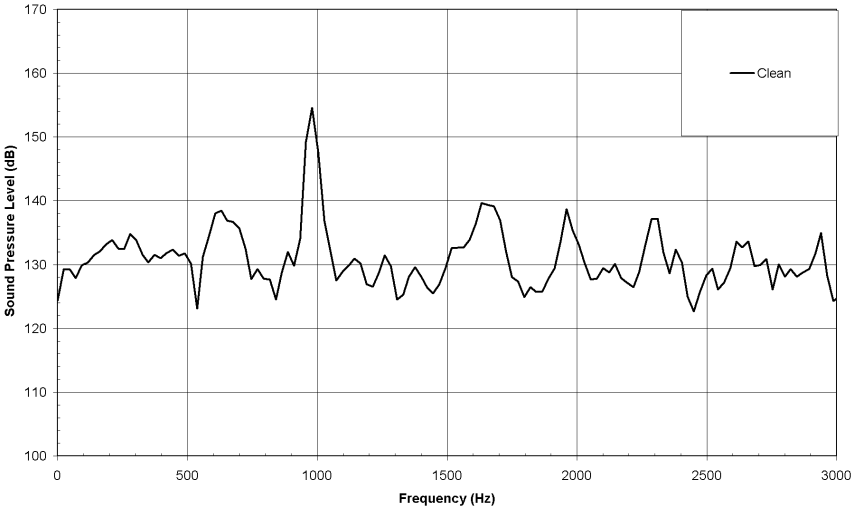

Figure B.2 – Sound Pressure Level vs Frequency of Clean Cavity K12 Sensor

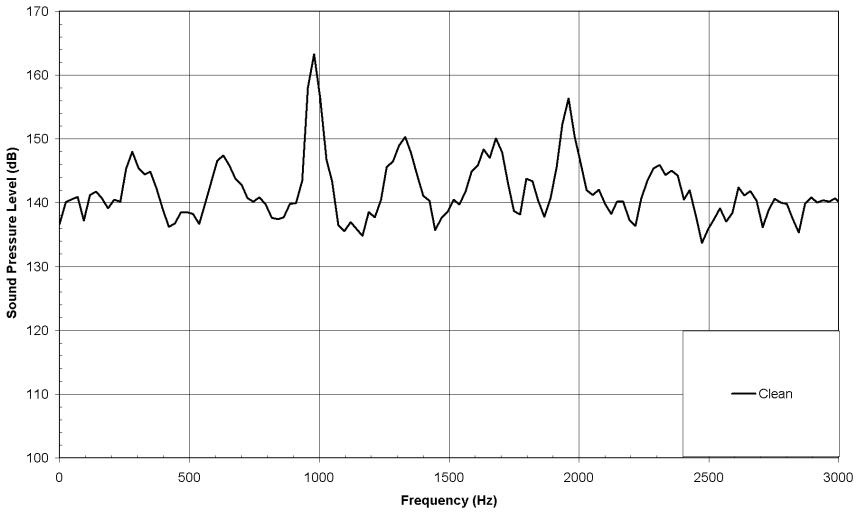

Figure B.3 – Sound Pressure Level vs Frequency of Clean Cavity K16 Sensor

B.1.b – Clean Cavity PSD Plots

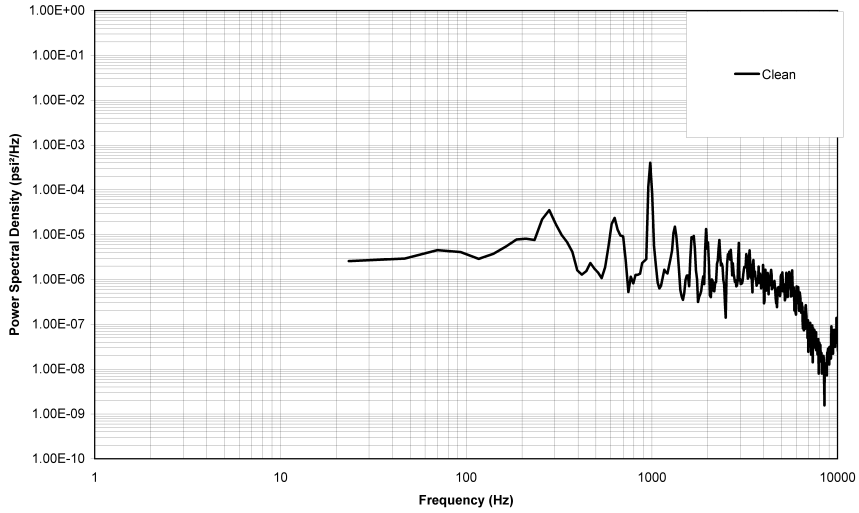

Figure B.4 – Power Spectral Density vs Frequency of Clean Cavity K5 Sensor

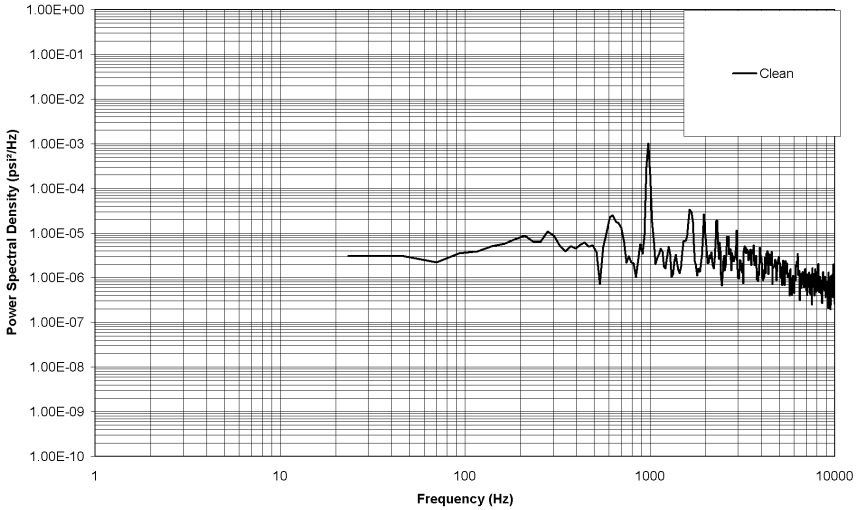

Figure B.5 – Power Spectral Density vs Frequency of Clean Cavity K12 Sensor

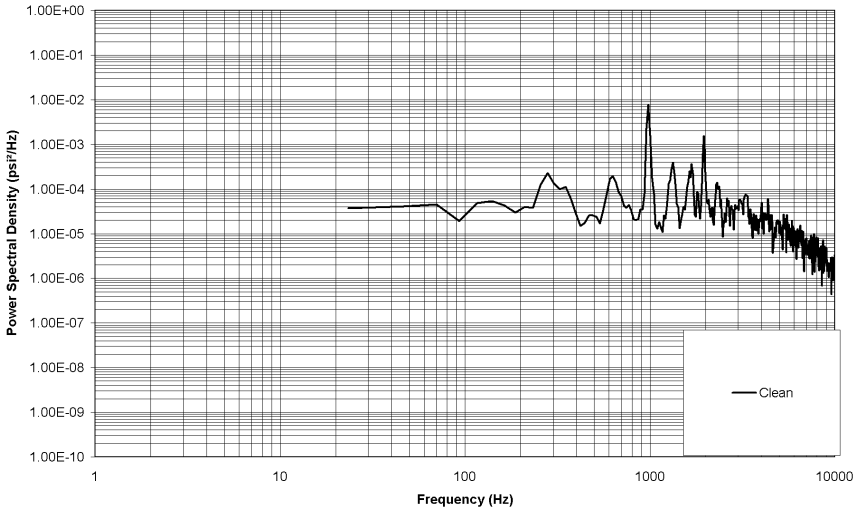

Figure B.6 – Power Spectral Density vs Frequency of Clean Cavity K16 Sensor

B.2.a – Combined Configuration SPL Plots

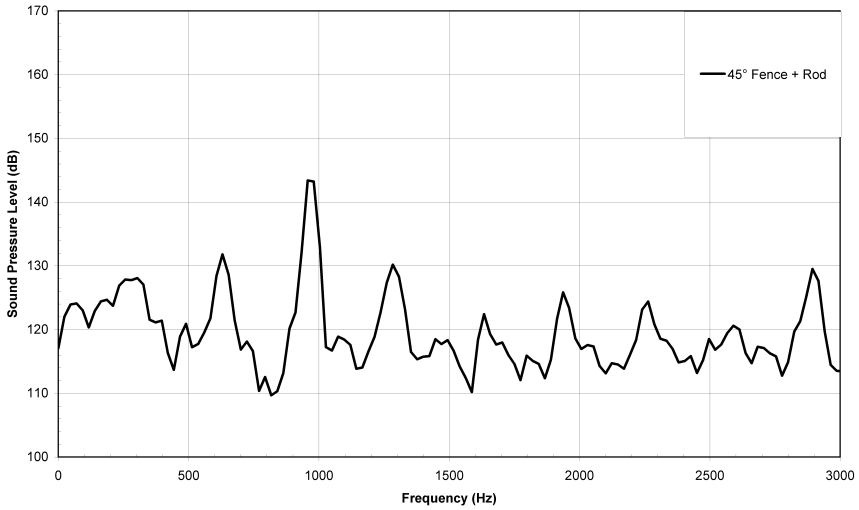

Figure B.7 – Sound Pressure Level vs Frequency of Combined K5 Sensor

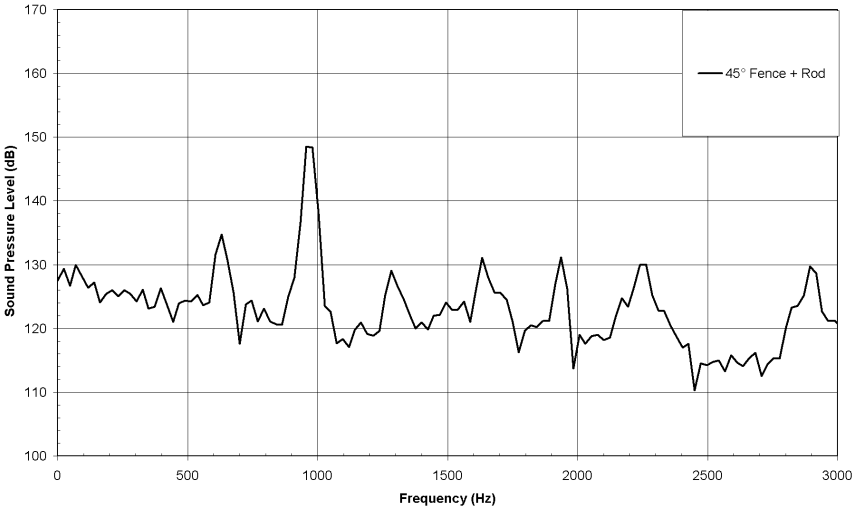

Figure B.8 – Sound Pressure Level vs Frequency of Combined K12 Sensor

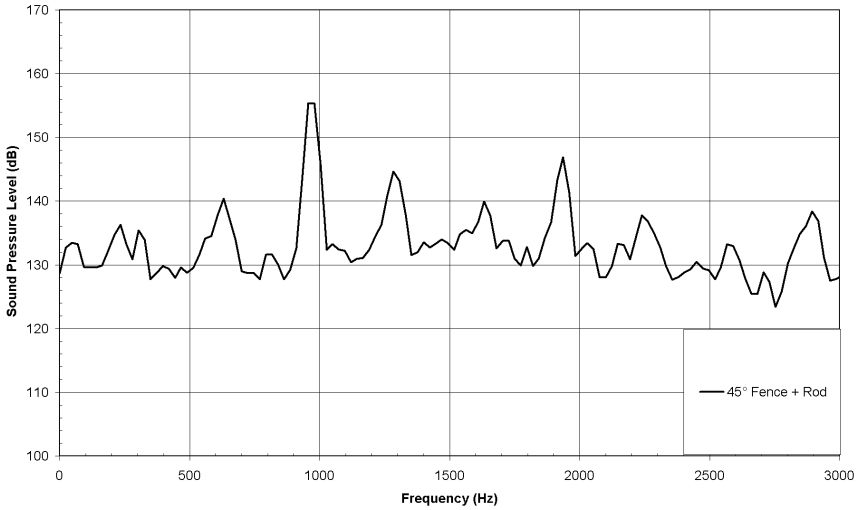

Figure B.9 – Sound Pressure Level vs Frequency of Combined K16 Sensor

B.2.b – Combined Configuration PSD Plots

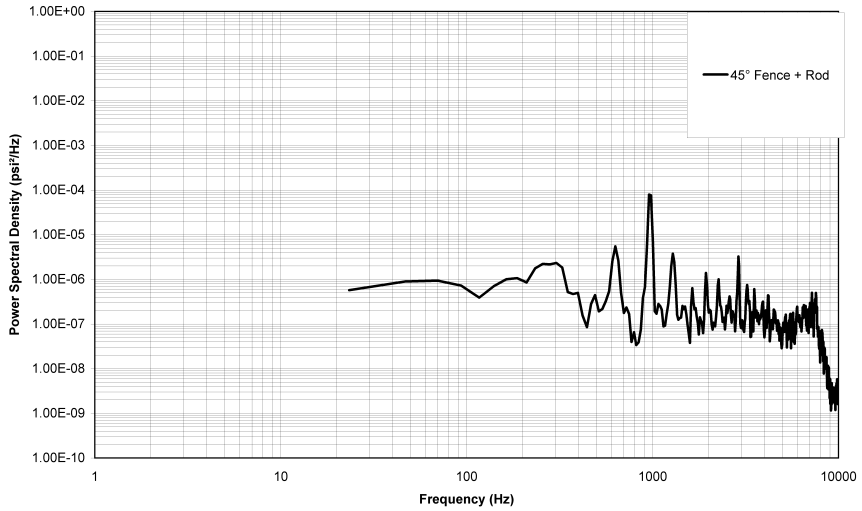

Figure B.10 – Power Spectral Density vs Frequency of Combined K5 Sensor

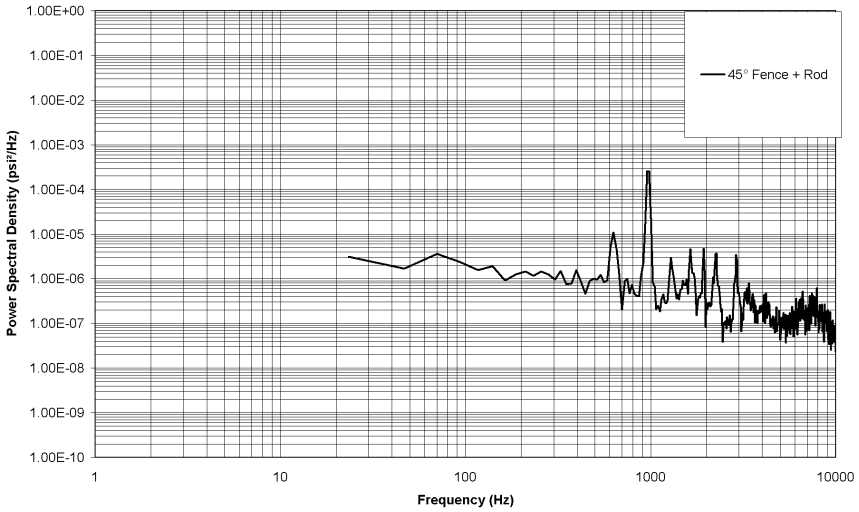

Figure B.11 – Power Spectral Density vs Frequency of Combined K12 Sensor

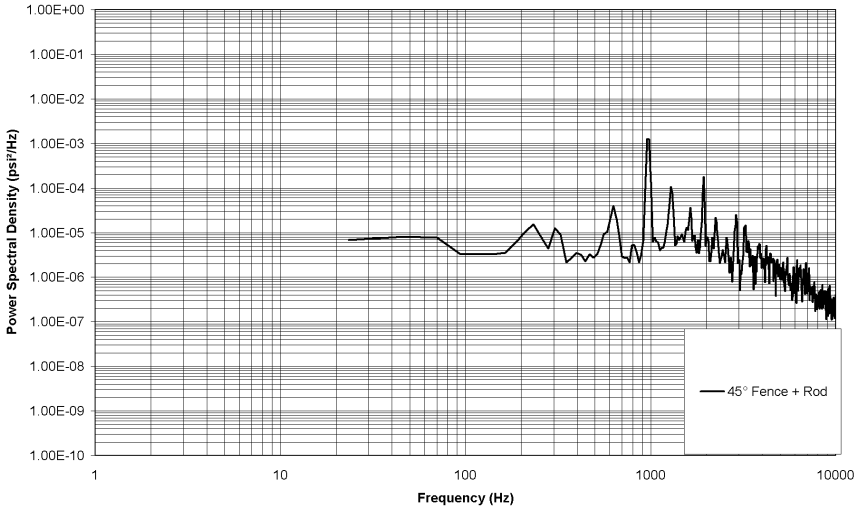

Figure B.12 – Power Spectral Density vs Frequency of Combined K16 Sensor

B.3.a – Single Rod in Crossflow SPL Plots

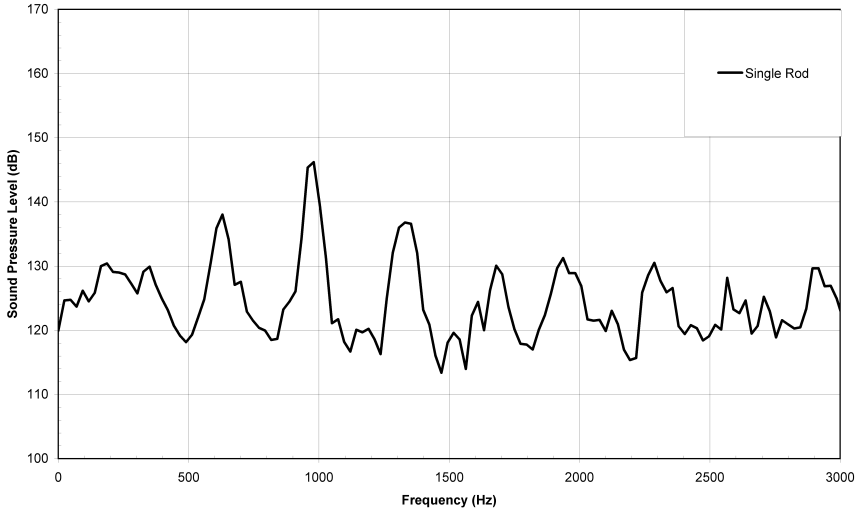

Figure B.13 – Sound Pressure Level vs Frequency of Single Rod K5 Sensor

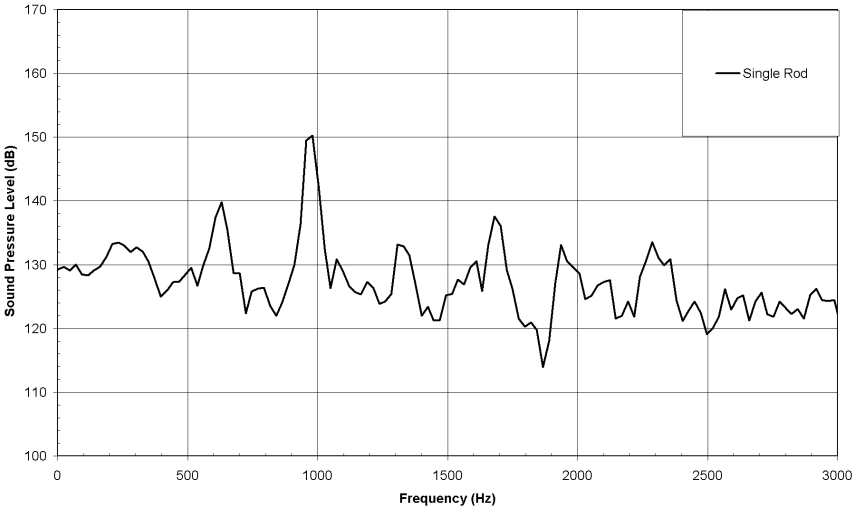

Figure B.14 – Sound Pressure Level vs Frequency of Single Rod K12 Sensor

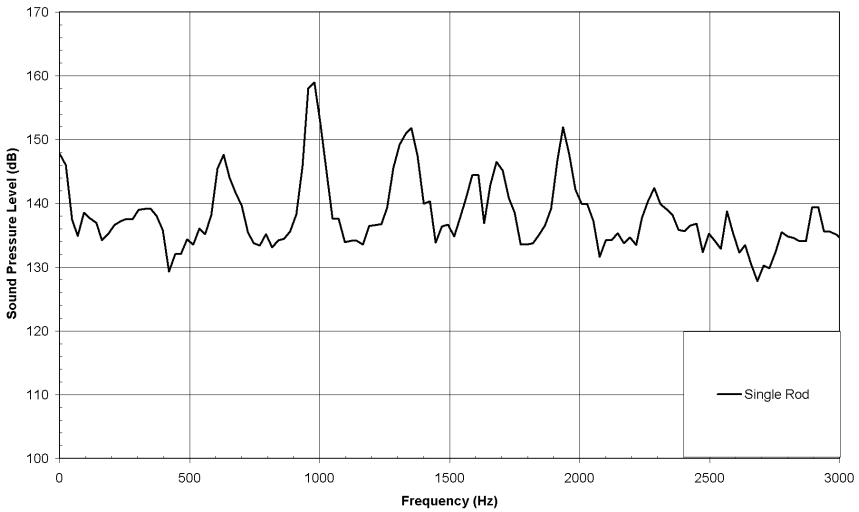

Figure B.15 – Sound Pressure Level vs Frequency of Single Rod K16 Sensor

B.3.b – Single Rod in Crossflow PSD Plots

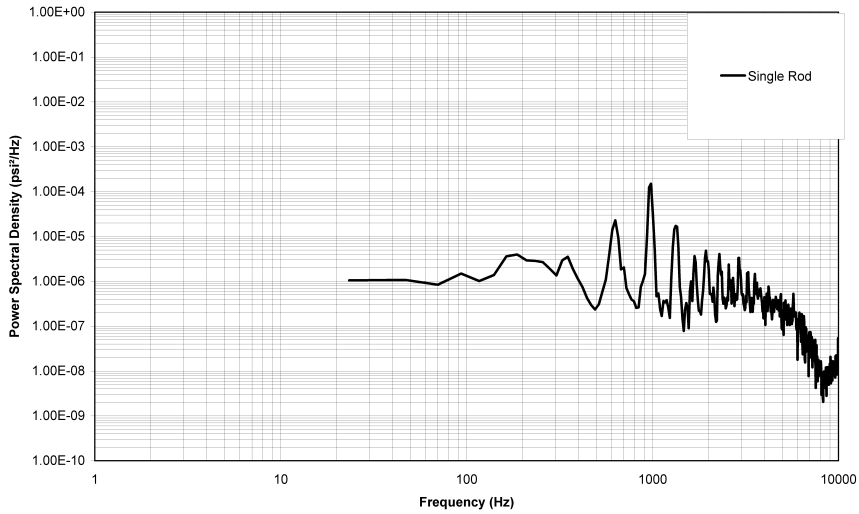

Figure B.16 – Power Spectral Density vs Frequency of Single Rod K5 Sensor

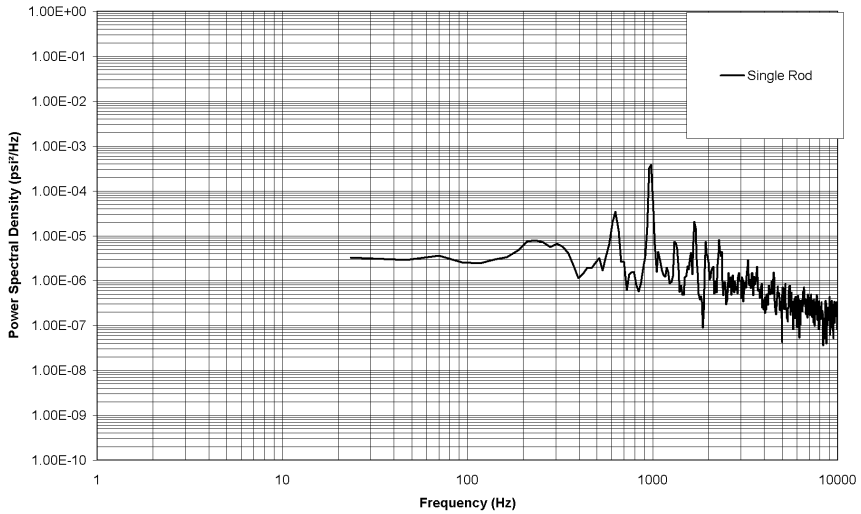

Figure B.17 – Power Spectral Density vs Frequency of Single Rod K12 Sensor

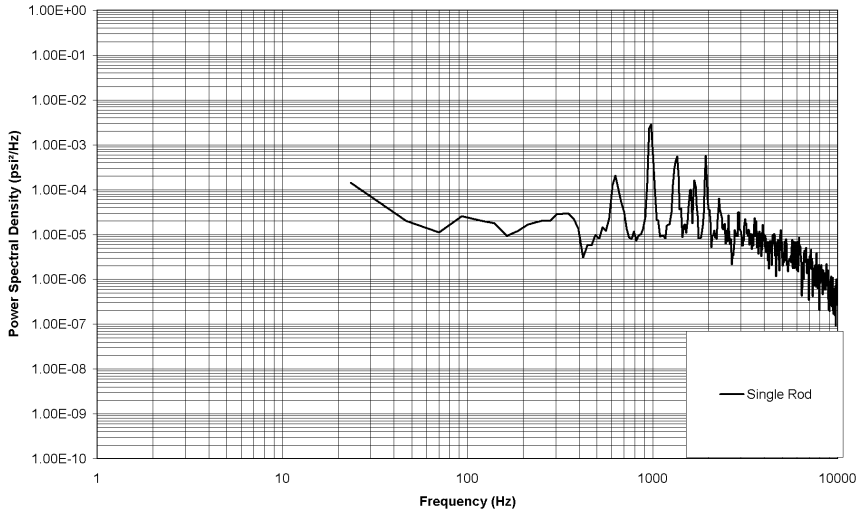

Figure B.18 – Power Spectral Density vs Frequency of Single Rod K16 Sensor

B.4.a – Forty-five Degree Fence SPL Plots

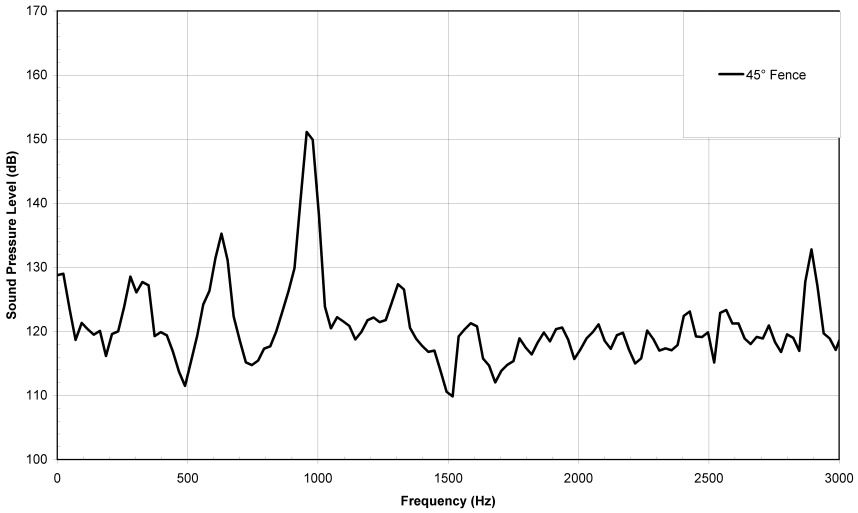

Figure B.19 – Sound Pressure Level vs Frequency of Forty Five Degree Fence K5 Sensor

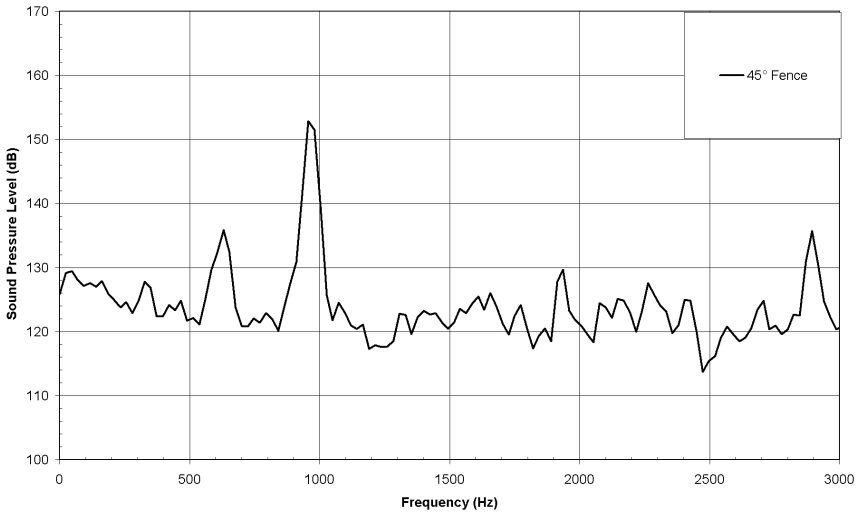

Figure B.20 – Sound Pressure Level vs Frequency of Forty Five Degree Fence K12 Sensor

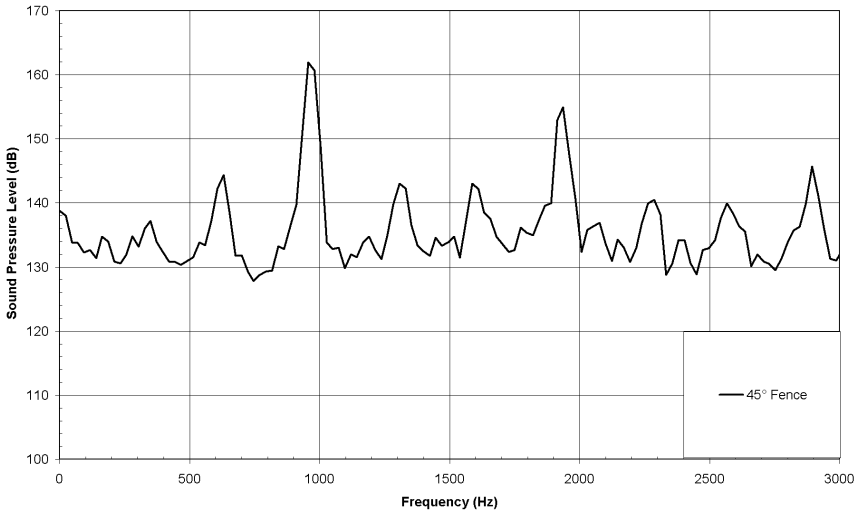

Figure B.21 – Sound Pressure Level vs Frequency of Forty Five Degree Fence K16 Sensor

B.4.b – Forty-five Degree Fence PSD Plots

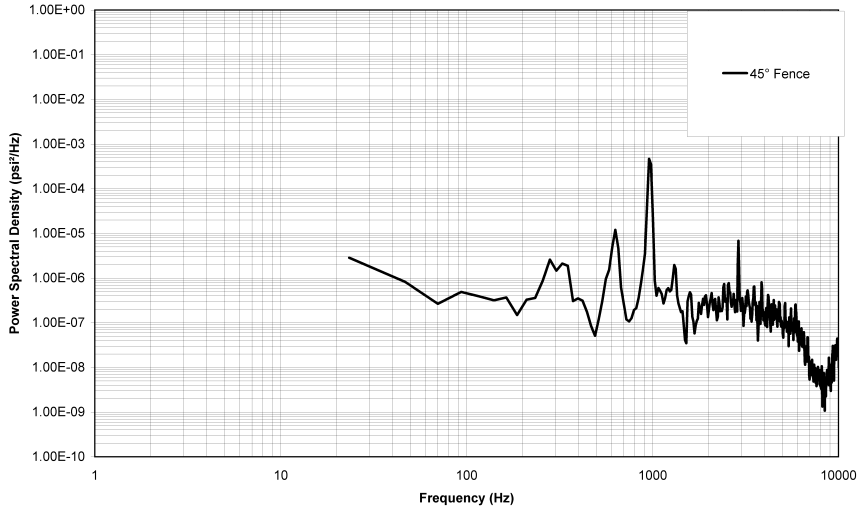

Figure B.22 – Power Spectral Density vs Frequency of Forty Five Degree Fence K5 Sensor

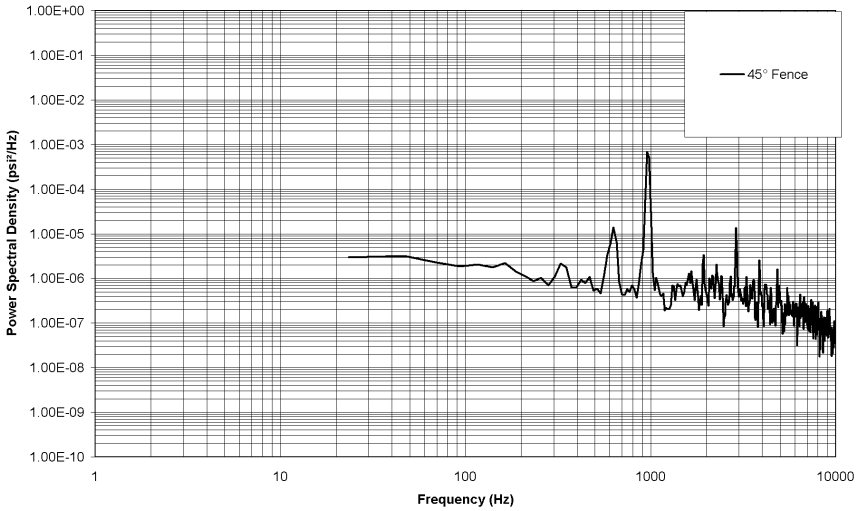

Figure B.23 – Power Spectral Density vs Frequency of Forty Five Degree Fence K12 Sensor

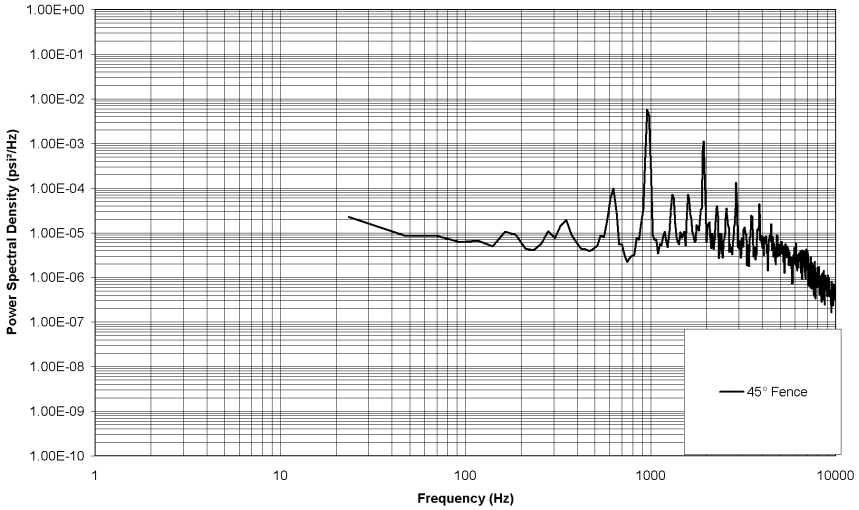

Figure B.24 – Power Spectral Density vs Frequency of Forty Five Degree Fence K16 Sensor

B.5.a – Modified Design SPL Plots

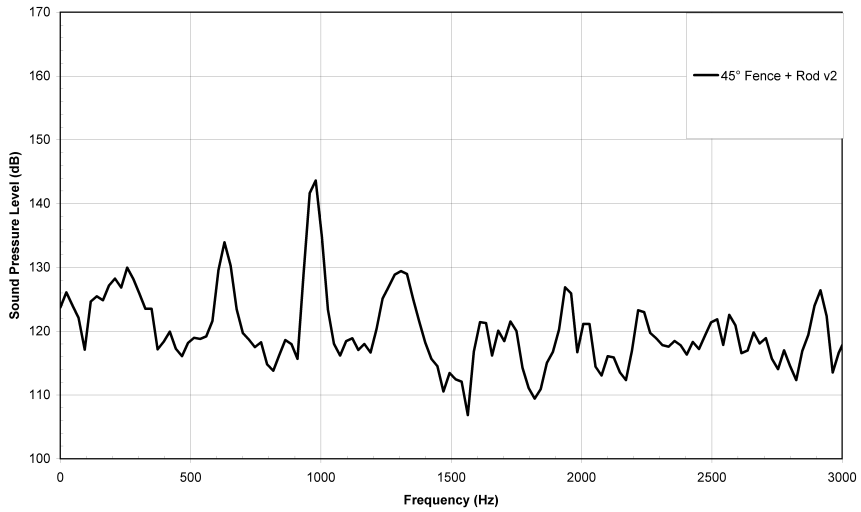

Figure B.25 – Sound Pressure Level vs Frequency of Modified Design K5 Sensor

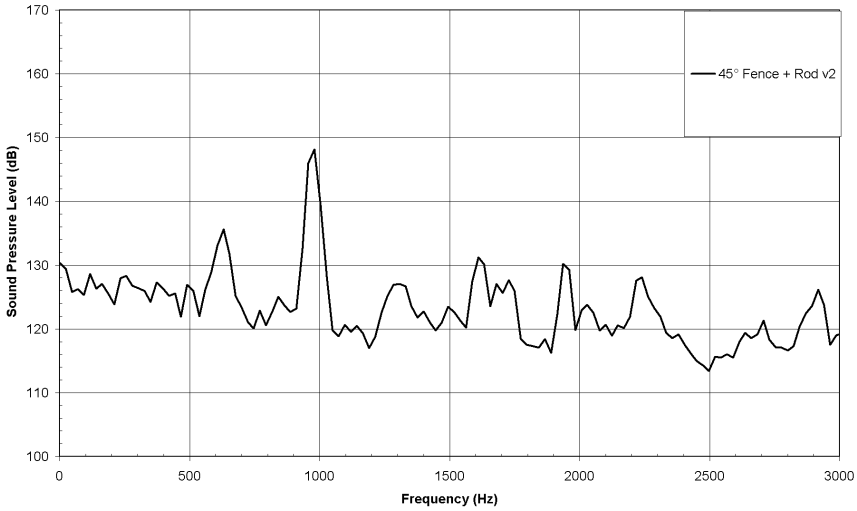

Figure B.26 – Sound Pressure Level vs Frequency of Modified Design K12 Sensor

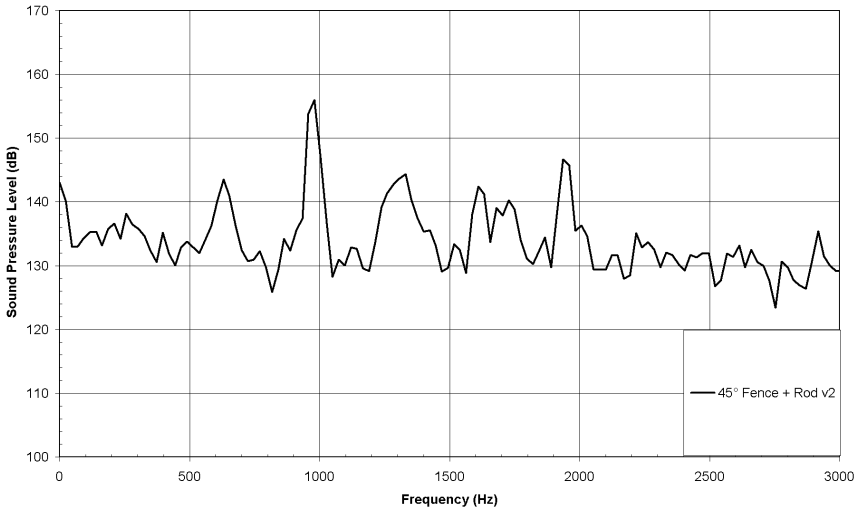

Figure B.27 – Sound Pressure Level vs Frequency of Modified Design K16 Sensor

B.5.b – Modified Design PSD Plots

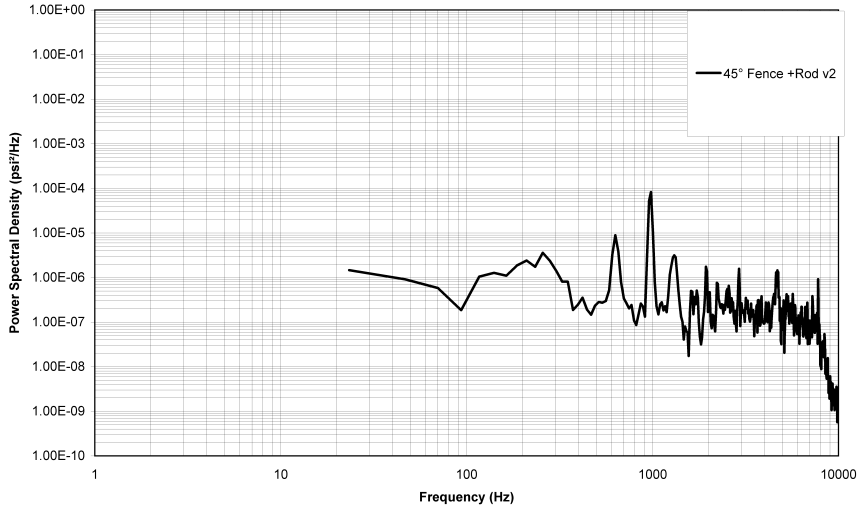

Figure B.28 – Power Spectral Density vs Frequency of Modified Design K5 Sensor

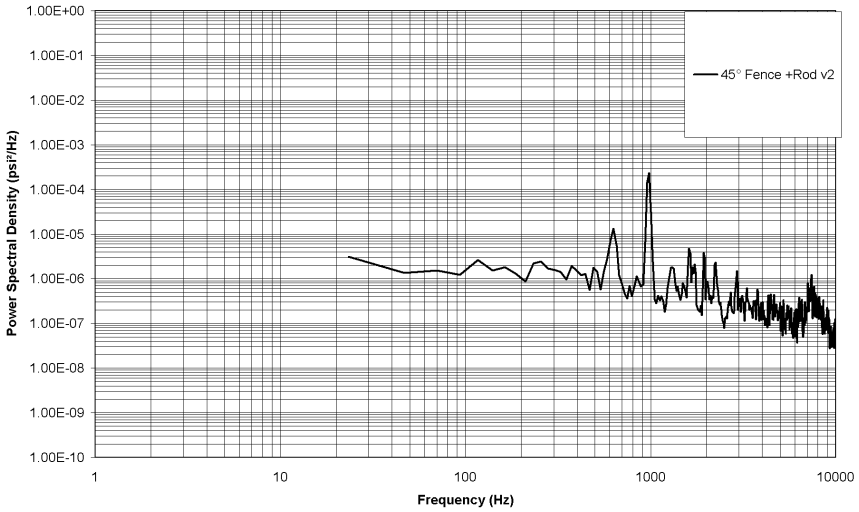

Figure B.29 – Power Spectral Density vs Frequency of Modified Design K12 Sensor

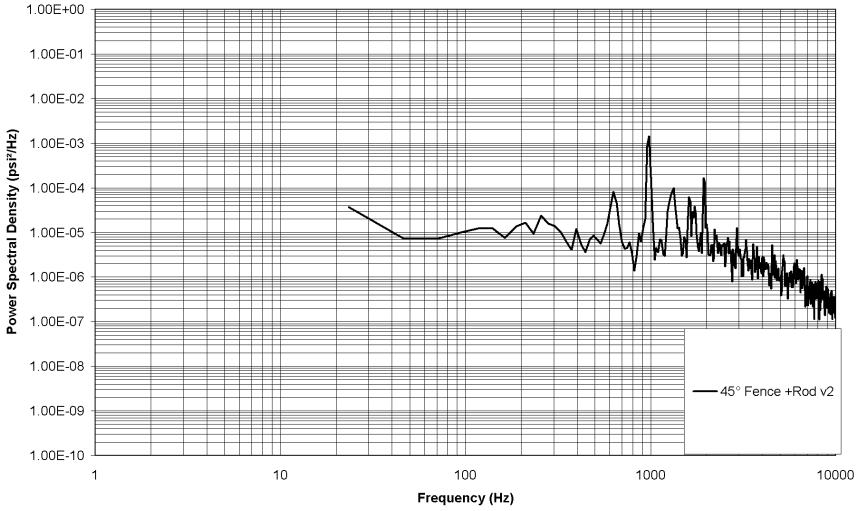

Figure B.30 – Power Spectral Density vs Frequency of Modified Design K16 Sensor

REFERENCES

[1] Dix, R. E., and Bauer, R. C., "Experimental and Theoretical Study of Cavity Acoustics," Arnold Engineering Development Center Technical Report, AEDC-TR-99-4.

[2] Stanek, M. J., Raman, G., and Kibens, V., "Control of Cavity Resonance Through Very High Frequency Forcing," AIAA-2000-1905, June 2000.

[3] Sarno, R. L., and Franke, M. E., "Suppression of Flow-Induced Pressure Oscillations in Cavities," *Journal of Aircraft*, Vol. 31, No. 1, Jan.-Feb. 1994.

[4] Nichols, R. H., "Algorithm and Turbulence Model Requirements for Simulating Vortical Flows," AIAA-2008-337, Jan. 2008.

[5] Nichols, R. H., Tramel, R. W., and Buning, P. G., "Solver and Turbulence Model Upgrades to OVERFLOW2 for Unsteady and High-Speed Applications," AIAA-2006-2824, June 2006.

[6] Nichols, R. H., Tramel, R. W., and Buning, P. G., "Evaluation of Two High Order WENO Schemes," AIAA-2007-3920, June 2007.

[7] Nichols, R. H., "Comparison of Hybrid RANS/LES Turbulence Models on a Circular Cylinder at High Reynolds Number," AIAA-2005-498, Jan. 2005.

[8] Nichols, R. H., "A Comparison of Hybrid RANS/LES Turbulence Models for a Generic Weapons Bay With and Without a Spoiler," AIAA-2008-6229, Aug. 2008.

[9] Covert, E. E., "An Approximate Calculation of the Onset Velocity of Cavity Oscillations," *AIAA Journal*, Vol. 8, No. 12, Dec. 1970.

[10] Brown, G. B., "The Vortex Motion Causing Edge Tones," *Proceedings of the Physical Society* Vol. 49, 493-507, 1937.

[11] Roshko, A., "On the Wake and Drag of Bluff Bodies," *Journal of the Aeronautical Sciences*, Vol. 22, Feb. 1955, pp. 124–132.

[12] Krishnamurty, K., "Sound Radiation From Surface Cutouts in High Speed Flow," Thesis, California Institute of Technology, 1956.

[13] Plumblee, H. E., Gibson, J. S., and Lassiter, L. W., "A Theoretical and Experimental Investigation of the Acoustic Response of Cavities in an Aerodynamic Flow," Wright-Patterson Air Force Base Technical Report, WADD-61-75.

[14] Rossiter, J. E., "Wind Tunnel Experiment on the Flow Over Rectangular Cavities at Subsonic and Transonic Speeds," Ministry of Aviation, Aeronautical Research Council, Reports and Memoranda No. 3438, Oct. 1964.

[15] Heller, H. H., and Bliss, D. B., "The Physical Mechanism of Flow-Induced Pressure Fluctuations in Cavities and Concepts for their Suppression," AIAA-1975-491-839., March 1975.

[16] Smith, D. L., and Shaw, L. L., "Prediction of the Pressure Oscillations in Cavities Exposed to Aerodynamic Flow," Air Force Flight Dynamics Lab Technical Report, AFFDL-TR-75-34.

[17] Heller, H. H., Holmes, G., and Covert, E. E., "Flow-Induced Pressure Oscillations in Shallow Cavities," Air Force Flight Dynamics Lab Technical Report, AFFDL-TR-70-104.

[18] Vakili, A. D., Gauthier, C., "Control of Cavity Flow by Upstream Mass Injection," AIAA-91-1645, June 1991.

[19] Sarohia, V., and Massier, P. F., "Control of Cavity Noise," AIAA-1976-528-600, July 1976.

[20] Gharib, M., "Response of Cavity Shear Layer Oscillations to External Forcing," *AIAA Journal*, Vol. 25, No. 1, Jan. 1987.

[21] Cattafesta, L. N., Garg, S., Choudhari, M., and Li, F., "Active Control of Flow-Induced Cavity Resonance," AIAA-97-1804, June 1997.

[22] McGrath, S. F., and Shaw Jr., L. L., "Active Control of Shallow Cavity Acoustic Resonance," AIAA-96-1949, June 1996.

[23] Seiner, J. M., Jansen, B. J., and Murray, N. E., "Weapons Bay Acoustic Suppression at Mach 2," AIAA-2008-60, Jan. 2008.

[24] Williams, D. R., and Fabris, D., "Closed-Loop Control in Cavities with Unsteady Bleed Forcing," AIAA-2000-0470, Jan. 2000.

[25] Stanek, M. J., Ross, J. A., Odedra, J., and Peto, J. W., "High Frequency Acoustic Suppression – The Mystery of the Rod-in-Crossflow Revealed," AIAA-2003-0007, Jan. 2003.

[26] Tramel, R., Rock, S., Ellis, J., and Sharpes, D., "Comparison of Large Cavity Aeroacoustic Computations with Flight Test Results," AIAA-2005-2800, May 2005.

[27] ESI Group. (2008). CFD-GEOM (Version 2008) Huntsville, AL.

[28] NASA. (2004). NASA Grid Tools (Version 2.0). NASA Ames Research Center.

[29] Rogers, S. E. (2003). Pegasus 5 (Version 5.1k). NASA Ames Research Center.

[30] Buning, P. (2008). OVERFLOW2 (Version 2.1s). NASA Langley Research Center.

[31] Dix, R. E., and Bauer, R. C., "Engineering Model Predictions of Aeroacoustic Amplitudes in a Weapons Cavity," AIAA-93-0858, Jan. 1993.

[32] Bushnell, D. M., "Application Frontiers of 'Designer Fluid Mechanics' – Visions Versus Reality or Attempt to Answer the Perennial Question 'Why Isn't It Used?'," AIAA-97-2110, June 1997.

[33] Illy, H., Jacquin, L., and Geffroy, P., "Observations on the Passive Control of Flow Oscillations over a Cavity in a Transonic Regime by Means of a Spanwise Cylinder," AIAA-2008-3774, June 2008.

[34] White, F. M., *Viscous Fluid Flow*, McGraw-Hill, Second Edition, 1991.